Development of Quantitative Phase Imaging for Temporal and Spectral Analysis of

Dynamic Microscopic Samples

by

Matthew Thomas Daniel Rinehart

Department of Biomedical Engineering
Duke University

Date:_____

Approved:

_____
Adam Wax, Supervisor

_____
David Brady

_____
Joseph Izatt

_____
David Katz

_____
Lisa Rohan

_____
George Truskey

Dissertation submitted in partial fulfillment of
the requirements for the degree of Doctor
of Philosophy in the Department of
Biomedical Engineering in the Graduate School
of Duke University

2014

ABSTRACT

Development of Quantitative Phase Imaging for Temporal and Spectral Analysis of Dynamic Microscopic Samples

by

Matthew Thomas Daniel Rinehart

Department of Biomedical Engineering
Duke University

Date:_____

Approved:

_____
Adam Wax, Supervisor

_____
David Brady

_____
Joseph Izatt

_____
David Katz

_____
Lisa Rohan

_____
George Truskey

An abstract of a dissertation submitted in partial fulfillment of the requirements for the degree of Doctor of Philosophy in the Department of Biomedical Engineering in the Graduate School of Duke University

2014

Abstract

Microscopic objects such as biological cells produce only minor modulation in the intensity of transmitted light, leading many researchers to add exogenous contrast agents for image enhancement. However, cells and other semitransparent objects that have not been chemically modified impart phase delays to the transmitted electromagnetic fields, which can be measured using interferometric microscopy methods. In this dissertation, instrumentation and methods are developed to investigate the spatiotemporal dynamics and spectral signatures of individual cells and semitransparent polymer film samples.

An off-axis quantitative phase microscope is applied to (1) quantitatively image the two-dimensional refractive index distributions of microbicide films undergoing hydration and compare effects of thickness and composition on dissolution dynamics, and (2) investigate the morphological and volumetric changes of individual RBCs undergoing mechanical flow stresses in *in vitro* models of capillaries. The quantitative phase microscope is further modified to capture high-resolution hyperspectral holographic phase and amplitude images. This novel hyperspectral imaging system is applied to compare the sensitivity of phase-based and amplitude-based spectral quantification of optically-absorbing molecules, and then used to measure spectroscopic changes in RBCs that take place during infection by *P. falciparum* parasites.

Measurements of an object's optical volume, which is defined as a novel metric for characterizing objects whose refractive index and thickness profiles are not known *a priori*. The composition and thickness of microbicide films are both found to impact spatiotemporal dissolution kinetics. A comparison of fluorophore concentration determination by amplitude and phase spectra indicates that both methods of quantification have comparable sensitivity, and that the two may be combined to improve the precision of quantity determination. Both optical volume and hemoglobin mass measurements are seen to decrease in cells infected by *P. falciparum*, although the two metrics are only loosely correlated. Finally, RBCs flowing through *in vitro* capillary models exhibit large changes in optical volume when deforming in response to mechanical stresses, which is attributed to a combination of cytosolic volume changes as well as conformational changes in the intracellular protein configuration.

These results demonstrate the applicability of QPM as a tool for evaluating (1) microbicide film performance, (2) spectroscopic changes in infected individual RBCs, and (3) novel biophysical changes observed in RBCs under mechanical stresses.

For Mom, Dad, and Anita. Your love and support have kept me moving forward through the ebb and flow of my time here at Duke.

Joy in looking and comprehending is nature's most beautiful gift.

Albert Einstein

Tiger got to hunt,
bird got to fly;
Man got to sit and wonder, 'Why, why, why?'
Tiger got to sleep,
bird got to land;
Man got to tell himself he understand.

Kurt Vonnegut

Contents

List of Tables

List of Figures

Acknowledgments

This dissertation represents the culmination of both my doctoral degree education and my tenure as a student at Duke University. Over the years, I have grown immensely as a researcher. Adam Wax has been an incredible advisor and advocate for me during this period, providing me with wisdom, opportunities, and support to explore a wide range of interests. The research summarized here would not have been possible without his guidance and support.

I also owe thanks to my committee members: Dr. Joseph Izatt and Dr. David Brady have taught me both in-class and out-of-class much of my knowledge on imaging and optical coherence. Dr. David Katz has been both a mentor and collaborator, as well as a fellow "gear-head" bike enthusiast. Dr. George Truskey and his former graduate student Kevin Zhao have developed an exciting new microfluidic platform for studying RBCs, and I have very much enjoyed working with them in the process to determine how quantitative phase measurements can complement their platform. All of my committee members have provided valuable input during my research, for which I am extremely grateful.

There are numerous other researchers in the Duke community whom I have learned from and worked with on projects: Drs. Jen-Tsan Ashley Chi, Greg Lamonte, Ian Wellsby, Brett Kirby, Becky Woodruff, Mardee Delahunty, Marilyn Telen, and graduate student Katelyn Walzer have all graciously provided blood samples and

indulged my many questions about their research. The staff of the shared materials instrumentation facility (SMIF) have further assisted me in planning and fabricating microscopic samples: Mark Walters, Jay Dalton, and Kirk Bryson in particular have steered me in the right direction on multiple occasions. Beyond Duke, Dr. Nicole Stacy has educated me about reptile and amphibian blood cell morphology, and Dr. Lisa Rohan and her graduate student Sheila Grab have taught me about the world of microbicides designed to prevent HIV transmission.

I also must thank the post-docs of Dr. Wax's lab who have spent many hours working on optical systems and experiments with me: Drs. Kevin Chalut, Natan Shaked, Yizheng Zhu, Bill Brown, and Tom Matthews. Additionally, the other graduate students in my lab and on my hall have been great research partners, lunch buddies, and fellow beer enthusiasts: Francisco Robles, Tyler Drake, Kenny Tao, Matt Crow, Stacy Millon, Neil Terry, Mike Giacomelli, Volker Jaedicke, Sanghoon Kim, and Hansang Park – thanks for keeping me sane and motivated over the years.

I'm grateful for the administrators here at Duke: August Burns, Kathy Barbour, Susan Story-Hill, and Kristen Rivers have supported my graduate studies immensely.

The Duke Cycling Team has alo kept me healthy and sane and provided some of the best memories I have since starting graduate school. While there are far too many people to name here whose time I have enjoyed, Rusty Miller, Chris Martin, Rob Ferris,

Kaleb Naegeli, ThomDom, and Mike Forbes have been phenomental friends, mentors, and coaches to me. Thank you for your friendship and wisdom.

Finally, this dissertation is for my parents, Tom and Jeannie Rinehart, and my girlfriend, Anita Kari, for the love and support they have given to me. More than I can express in words, I love you and am grateful to you.

1 Introduction

1.1 Motivation

Holographic imaging was first presented in 1948 by Denis Gabor as a method for improving electron microscopy images.[1] The amplitude and phase of the electromagnetic waves were lenslessly recorded in a photosensitive material, which could then be illuminated to reproduce an image of the original object. For this pioneering work in holography, Gabor was awarded the 1971 Nobel prize in physics. The advent of the laser in the late 1950s made powerful coherent light sources available, and the development of charge-coupled devices (CCDs) in the 1960s and 1970s enabled digital imaging (two more Nobel prize-winning inventions). The parallel development of these two technologies has made possible their merger in the field of digital holography.

Over the last two decades, the pairing of digital holographic imaging with microscopy has led not only to an array of techniques for holographic image formation, but to a strong interest in quantitative measurements of the optical phase delays imparted by semitransparent samples. Unlike fluorescence microscopy that relies on exogenous fluorophores or the expression of fluorescent proteins after gene transfection, phase microscopy can be performed on samples that have not been modified or labeled. Other methodologies such as differential-interference-contrast (DIC) and phase-contrast microscopy translate phase delays through a sample into intensity differences, however

these techniques primarily produce image contrast and quantitative phase delays are not readily calculable. On the other hand, digital holographic microscopy methods have been developed to yield milliradian phase sensitivity in images, corresponding to nanometer-scale axial measurements.

Quantitative phase microscopy (QPM) is a promising tool for quantitative biological research as measured phase delays are straightforwardly related to the refractive index and thicknesses of individual cells. QPM has been widely used to study the mechanical properties of red blood cells and has also been used for measuring dry mass and growth dynamics of other *in vitro* cells. It can also be applied to other thin semitransparent samples with suitable geometry, e.g., microfluidic devices and semitransparent films. Recent improvements in imaging sensor speed, pixel density, and light sensitivity have made it possible to study sample dynamics with both high speed (> kHz) and diffraction-limited spatial resolution over larger fields of view. The speed improvements of two-dimensional imaging sensors also allow for a large number of measurements to be rapidly performed, opening up the possibility of capturing time resolved spectral information.

1.2 Project Overview

The overall goals of the research presented in this document are (1) to advance the instrumentation and processing methods used for holographic microscopy, (2) to extend quantitative phase microscopy into a spectroscopic imaging modality, and (3) to

apply quantitative phase microscopy and spectroscopy to investigate temporal and molecular changes in semitransparent objects. This is accomplished through the development and refinement of two related but distinctly different systems, a single-wavelength time resolved off-axis Quantitative Phase Microscope (QPM) and a broadband high speed Quantitative Phase Spectrometer (QPS).

Through the course of instrument development and application, optical volume has been defined and shown to be a valuable metric for quantifying individual cells whose refractive index and thickness profiles are not precisely known and vary across populations. Accurate optical volume measurement will also be shown to require careful image focus, leading to the application of digital refocusing to correct for both axial cell motions relative to a static plane of focus as well as variations in manual focusing when acquiring images.

The laser-illuminated off-axis QPM instrument was designed to capture high-resolution holograms that can be processed to produce low-noise quantitative phase images from single interferograms. This system enables studies of dynamically-changing samples with time-resolution limited only by the frame-rate of the camera. The off-axis processing method prevents degradation of phase information that can arise from sample motion when using phase-shifting interferometry. This system is first applied using low magnification (2.5x) and relatively low frame rates (4 frames per second) to measure and compare the dissolution dynamics of polymeric microbicidal

films. Off-axis QPM is next applied at high speeds (1 kHz frame rate) to measure the deformations and morphological changes exhibited by red blood cells flowing through microchannels that are designed to mimic *in vivo* capillaries. The measured optical volume changes in individual RBCs motivate further modeling and studies to better understand their dynamic responses to mechanical stresses.

After constructing an initial QPS instrument that employed an acousto-optic tunable filter to capture hyperspectral hologram datasets spanning the visible range, an improved spectral filter was designed with narrower spectral line width and a method of acquiring and averaging multiple spectral sweeps of the same sample was implemented to reduce the spatiotemporal noise of the resulting phase and amplitude images. This improved imaging system has a narrower spectral line width to reduce washout of observed spectral features, and has a lower noise floor than the original QPS instrument to enable single-cell quantification of absorbing molecules.

Molecular absorbers exhibit corresponding nonlinear spectral phase features, which are mathematically linked by the Kramers-Kronig relations. Hologram amplitude and phase measurements are mathematically distinct, and each may be used to quantify a molecule's signature independently. Therefore, the QPS instrument is first applied to compare the sensitivity of amplitude-based spectroscopy to phase-based spectroscopy using the same holographic data set. Each method of quantification is found to produce similar results with equivalent spatial precision of measurement, leading to improved

sensitivity when combining both amplitude and phase information. QPS is next applied to investigate the spectroscopic changes induced by *P. falciparum* infection in individual cells.

1.3 Document Organization

The dissertation document is organized as follows. Chapter 2 reviews literature that gives context to the interferometer designs, holographic processing methods, and biological systems studied in subsequent chapters. The off-axis quantitative phase microscopy (QPM) and quantitative phase spectroscopy (QPS) instruments as well as the associated phase image conditioning methodology and a detailed noise characterization are discussed in Chapter 3. Chapter 4 introduces optical volume (OV) as a novel measure of samples whose refractive index (RI) and height spatial distributions are not easily separated and discusses the importance of digital refocusing for accurate OV measurements. This chapter further presents both a framework for reducing holographic image noise by spectral averaging and also a head-to-head comparison of sensitivity achieved when estimating molecular quantities from phase spectra and amplitude spectra.

After outlining the instrumentation and image processing methods developed and applied in this work, Chapters 5 - 7 present three studies of microscopic semitransparent samples by QPM and QPS. The spatiotemporal dissolution kinetics of polymeric microbicide films are measured by QPM and analyzed using spatial Fourier

analysis to compare hydration across samples with varying thicknesses and compositions in Chapter 5. QPS is then applied in Chapter 6 to quantify spectral changes in infected red blood cells (RBCs) that are associated with the consumption of hemoglobin by *P. falciparum*. Finally, Chapter 7 presents a study of RBCs traveling through an *in vitro* model of a capillary microchannel by high-speed single-wavelength QPM. Individual RBCs are observed to undergo extreme morphological deformations and are measured to have corresponding optical volume changes that suggest a combination of reversible water volume and material property changes. The research presented in Chapters 3 – 7 is summarized in Chapter 8, and future research studies are briefly discussed.

2 Background

This chapter gives context to the topics discussed within this dissertation. Section 2.1 reviews various methods of quantitative phase microscopy using digital holography and discusses their advantages and disadvantages. Section 2.2 examines techniques that have been developed to make use of spectral features within the framework of holographic microscopy. After reviewing the literature pertaining to digital holographic microscopy and spectroscopy, section 2.3 gives a brief overview of three model systems that are investigated later in this document: microbicidal films for topical delivery of anti-HIV drugs, the mechanical and compositional properties of RBCs during hydrodynamic flow, and the spectral changes that occur during infection of individual RBCs by *P. falciparum* parasites. Several investigations of the biophysics of individual RBCs by holographic microscopy have been conducted, and so the current progress of characterizing the latter two systems by QPM and QPS are also highlighted in this section.

2.1 Quantitative Phase Microscopy by Digital Holographic Microscopy

Digital holographic microscopy (DHM) setups use light sources, interferometers, and digital detectors designed to capture holograms of microscopic objects. Digitization allows rapid imaging from the typical ~30fps video rate imaging up to kHz rate high speed acquisition. Digital holography, as applied to microscopic investigation of

biological dynamic samples, became the focus of several research groups in the late 1990s, and since then much effort has been invested in improving imaging speed, lateral resolution, spatiotemporal noise characteristics, and the accuracy of phase and amplitude measurements. The recent development of DHM-based phase imaging techniques has improved quantitative analysis over traditional phase microscopy of *in vitro* cell cultures and other semitransparent dynamic systems, and has also defined new useful parameters.

Holographic microscopy systems are broadly split into two categories: (1) phase-shifting interferometry, which captures multiple frames in time with shifted interference patterns and combines the interferograms to recover phase information; (2) off-axis interferometry, which uses an angular tilt between the interferometer beams to create a "spatial carrier frequency" that allows spatial Fourier filtering to recover complex phase and amplitude information. The following subsections review techniques and instrument configurations that use each of these two processing methods and have become widely used for quantitative phase microscopy by DHM.

2.1.1 Phase-shifting Holographic Microscopy

Yamaguchi and Zhang first demonstrated phase shifting digital holography for imaging microscopic samples in 1998.[2] In their work, a Mach-Zehnder interferometer is used to split a CW laser beam (λ=514nm) into a sample and a reference beam, and a mirror mounted to a PZT shifts the reference arm path length in four steps of $\pi/2$. The

resulting phase-shifted interferograms are used to calculate the object's phase distribution, and the complex amplitude is then propagated by Fresnel transform[3] to various focal planes. This method requires a second interferometer and fringe analyzer to carefully control the phase shifts, and results in an image magnification that varied with propagation distance because of the non-infinity-corrected imaging geometry. Furthermore, only the refocused amplitude images were presented without phase information.

Popescu, *et al.*, further developed phase-shifting holographic microscopy into a technique dubbed Fourier Phase Microscopy (FPM).[4,5] FPM uses the video port of a commercial microscope, thus capturing microscopic images that are assumed to be well-focused and require no digital propagation. A set of lenses images the Fourier plane of the microscopic object onto a two-dimensional programmable phase modulator (PPM), which can be digitally controlled to shift the phase of the zero-frequency Fourier component relative to the higher spatial frequencies that correspond to the object's spatial features. The back-reflected light from the PPM is Fourier transformed by a lens and forms an image on a CCD. Because the interference between the phase-shifted zero-frequency component and the image's nonzero spatial frequencies follow a common-path geometry and the phase shifts are accurate to ~24mrad, the calculated phase images are temporally stable to σ=0.15nm in the absence of sample objects. FPM also has low speckle noise, as the illumination is a low coherence superluminescent diode (SLD) with

a 20-nm bandwidth (λ_0=809 nm). However, this technique still requires four phase-shifted interferograms and is limited to an imaging rate of 4 frames/minute by the PPM, making it accurate only when measuring changes on long (minutes-to-hours) timescales.

Wang, *et al.*, working in the independent research group of Popescu, developed an imaging module dubbed "spatial light interference microscopy" (SLIM), which builds on the principles of FPM.[6] An external module, consisting of a pair of lenses, a liquid-crystal phase modulator, and a CCD camera attached to the imaging port of a commercial white-light inverted microscope is set up with a phase-contrast condenser and microscope objective. In contrast to FPM, the LCPM is programmed to step the spatial frequencies corresponding to the phase-contrast ring rather than the DC spatial component. The quantitative phase distribution is calculated identically to FPM using 4 phase-shifted interference images. By using a broadband white-light illumination source, coherent noise is reduced, resulting in a temporal sensitivity of σ_t = 0.029 nm and spatial sensitivity of σ_s = 0.28 nm. The LCPM also allows faster modulation (up to 15 calculated quantitative phase-contrast images per second), though the SLIM system presented is limited by the camera to a rate of 2.6 images/s. The major drawback of SLIM is that the resulting quantitative phase images suffer from the same halo and shade-off artifacts that are seen in traditional phase-contrast imaging.

2.1.2 Off-axis Holographic Phase Microscopy

Off-axis holography allows the recovery of phase images from single interferograms, thus offering a time advantage over phase-shifting algorithms that require multiple exposures to reconstruct a single phase image. Rather than being limited by the rate at which the phase may be shifted, off-axis holography is only limited by the rate at which photons may be collected by the camera. As camera speed increases, this allows for the investigation of high-speed dynamics that are otherwise missed by phase-shifting microscopes. However, off-axis phase microscopy trades detector spatial bandwidth for speed in order to recover phase information, therefore limiting either resolution or field of view to less than what could be achieved using phase-shifting interferometry.

Cuche, *et al.*, describe a quantitative phase- and amplitude-microscope setup that employs an off-axis Mach-Zehnder interferometer with a camera placed intermediately between the microscope objective and the estimated image plane.[7] In this scheme, the sample and reference beams are carefully constructed plane waves. An image is not formed on the detector, but rather the interferogram is first detected then numerically-propagated using the Fresnel kernel to the image plane, where the complex amplitude and phase of the magnified object are recovered.

Ikeda, *et al.*, introduced Hilbert phase microscopy (HPM) as a method of recovering phase information from a single interferogram.[8] A modified Mach-Zehnder

interferometer is used to produce off-axis interferograms of microscopic fields of view in which the carrier frequency is large enough to separate the sample-reference cross-correlation terms from the autocorrelation terms of the two fields and retain diffraction-limited resolution. One key difference between the work Ikeda, *et al.*, and that by Cuche, *et al.*,[7] is that the microscope configurations of the sample and reference fields image the sample onto the detector plane. Because a tube lens is used in an infinity-corrected geometry, the interferograms have the potential to be refocused over a large range while retaining uniform magnification (however this is not discussed or demonstrated). High-pass spatial filtering is used to remove the image autocorrelation terms from the interferogram, and the phase of the resulting data is recovered through the use of a Hilbert transform and the arctangent operation. The phase of the carrier frequency is removed by linear subtraction of a phase ramp in one direction. This technique is demonstrated with a frame integration time of 10.3 ms; furthermore, because multiple interferograms are not required, the phase uncertainty only arises from temporal instability in the interference pattern over this ms-scale integration time window. Although each image benefits from single-shot stability, the phase noise over time is σ_t=1.25 nm, approximately 1-2 orders of magnitude worse than the common-path phase-shifting microscopy methods described above.

Popescu, *et al.*, addressed the temporal instabilities present in HPM by developing a near-common-path geometry off-axis phase microscope module referred to

as diffraction phase microscopy (DPM).[9] Like FPM and SLIM, DPM uses the output from the imaging port of a commercial inverted microscope; however, in these experiments, the microscope is illuminated with a 532nm laser, which has significantly higher coherence than the SLD and white-light sources used in FPM and SLIM. A grating is placed in a conjugate image plane, separating the optical field into a sample (+1 order) and reference (0 order) field. Both fields are imaged onto a camera using two lenses in a 4F imaging configuration. This configuration allows access to the Fourier plane of both the sample and reference fields; an aperture placed in this plane filters the reference field through a pinhole to create a planar wave, and allows the sample spatial frequencies to pass through. The DPM components are chosen such that the angle between the 0- and +1-orders allows the diffraction-limited resolution as defined by the microscope objective to be preserved in the resulting phase images. Captured interferograms are processed using the Hilbert transform method[8] to produce quantitative phase images. This DPM system preserves the single-shot nature of HPM, and moderately improves on the noise characteristics: a 3x3-pixel area has a temporal noise of σ_t = 0.53nm (1000 images over ~10s) while the field of view has a spatial noise of σ_s = 0.7 nm.

2.2 Spectroscopic Quantitative Phase Microscopy

Several techniques have been developed based on QPM to examine the spectroscopic information of microscopic samples. Certain molecules exhibit absorption

peaks with corresponding refractive index nonlinearities, allowing spectroscopic detection and quantification. Multiple imaging methods have recently been developed to capture spectroscopic phase information and investigate dispersive and absorptive features in order to gain further information about the molecular composition of microscopic objects.

Several spectroscopic phase microscopy systems have been developed using the DPM design framework to investigate endogenous spectral features of cells at a handful of discrete wavelengths. In 2009, Park, *et al.*, constructed a system illuminated by a spectrally-filtered white light source to capture phase images at 7 center wavelengths across the visible spectrum with ~10-20nm of spectral bandwidth.[10] This system was used to characterize the dispersion and RI increments of bovine serum albumin (BSA) and hemoglobin. These data were then used to estimate cell volume and hemoglobin concentration in a population of 25 RBCs (results were consistent with normal physiological ranges[11]). The measurements were reported to exhibit a phase noise of ~3 mrad, corresponding to RI increment uncertainties of ~ ± 0.003 – 0.005 ml/g and sensitivity to changes of 0.08 – 0.13 pg of hemoglobin. More recently, Park's research group presented a similar DPM-based microscope that used three lasers matched to the RGB channels of a color camera to simultaneously capture three spectrally-distinct interferograms of RBCs simultaneously.[12] Although comparable noise figures are not presented, fitting the phase measurements to a nonlinear model produced mean cell

volumes and mean cell hemoglobin concentrations in a population of 24 cells that also matched hematology reference ranges. Another system from Park's group was developed to image the dispersion of individual cells by measuring phase at two specific wavelengths, 310nm and 410nm.[13] In that work, measurements of the RI increments of DNA and protein solutions were accurate to ±0.001 – 0.014 ml/g, and ratiometric images of the OPL at the two wavelengths indicated that the relative dispersion of HeLa cells ranges ~σ = 1 – 2% over the projected cell area.

High resolution spectroscopic quantitative phase microscopy has only recently been developed. Robles, *et al.*,[14] in our research group made use of spectral domain phase microscopy (SDPM[15]), an extension of optical coherence tomography (OCT), to estimate the thickness and measure the nonlinear refractive index features of individual RBCs arising from hemoglobin in the visible spectral range. This system acquired successive interferometric spectra of spatial lines across the sample, which was translated laterally in small increments to build up a two-dimensional image. Using the nonlinear RI spectrum of hemoglobin calculated from the absorption spectrum by the modified Kramers-Kronig relations[16], the concentration of hemoglobin within a single cell was calculated to be 33.4 ± 7.7 g/dL (variability represents intracellular concentration variation). The system's phase sensitivity of ~10 mrad places a lower bound on concentration estimation of ~0.5 g/dL.

Soon after the work of Robles, *et al.*, I developed quantitative phase spectroscopy (QPS)[17], a method of off-axis transmission QPM using a swept spectral source, as discussed in detail in section 3.2. This system used a supercontinuum laser source filtered by an acoustooptic tunable filter to step the illumination wavelength in 1 nm increments across the visible spectrum, acquiring holograms at each wavelength. In the published work, the refractive index spectra of fluorescent microspheres and serial dilutions of hemoglobin were measured, qualitatively demonstrating spatially-resolved nonlinear spectral features. Jung, *et al.*,[18] adapted this system to use a DPM interferometric geometry and a xenon arc lamp that was spectrally-filtered and tuned using a diffraction grating in combination with a galvanometer scanning mirror ("galvo"). This new system captured 82 holograms across a range of 466 – 732 nm with a spectral bandwidth of ~7.5nm for each hologram. The swept-source DPM (ssDPM) system was used to measure phase and amplitude spectra of light transmitted through individual RBCs from which subsequent relative RI increment spectra and absolute molar extinction coefficient spectra were determined. The RI increment and molar exctinction coefficient spectra averaged over 10 cells show reasonable qualitative agreement with referenced values and do contain the nonlinear spectral features consistent with hemoglobin absorption, but are not quantitatively compared. Both the ssDPM and QPS systems described in the literature capture their respective hyperspectral holographic image sets over a ~5-6s time.

While spectroscopic holography is being pursued to capture molecular information about cells during holographic imaging, other approaches obtain molecular information by integrating fluorescence microscopy with single-wavelength holographic microscopy. Mann, *et al.*, presented a combined fluorescence and holographic microscopy system that uses optical shutters to sequentially capture co-registered fluorescence and phase images of individual cells.[19] This system allows morphological phase images to be captured in conjunction with fluorescence images that provide molecular specificity, however, the frame rates are limited by the use of an optical shutter. Very recently, Chowdhury, *et al.*, developed a structured illumination super-resolution optical system that excites fluorophores with a 410nm source and then splits the transmitted light from the flouorescence using a dichroic mirror. Each channel then passes through separate common-path off-axis interferometers adapted from the DPM design which recombines the light and images both channels onto a camera. The fluorescence and transmitted interferograms are separated in the spatial frequency domain and further processed to recover sub-diffraction-limited phase and fluorescence images. While both of these combined fluorescence and phase microscopy imaging systems exploit spectral features to investigate sample morphology with molecular specificity, they also are designed to be used with exogenous constrast agents which offer a fluorescence emission that is orders of magnitude weaker in intensity than the transmitted light used for phase imaging.

2.3 Applications

Off-axis QPM is well-suited for studying the temporal dynamics of semitransparent microscopic objects, and QPS provides a platform for measuring spectral features of microscopic objects. In this dissertation, the two instruments are applied to investigate three systems of biological interest: (1) microbicidal films for topical delivery of anti-HIV drugs; (2) the mechanical and morphological properties of RBCs during hydrodynamic flow, and (3) spectral changes that occur during infection of individual RBCs by *P. falciparum* parasites. The following sections provide background on each of these, and provide context for the studies conducted with QPM and QPS.

2.3.1 Microbicidal Films

Thin polymeric films have been developed as solid dosage forms for delivering drugs topically. These films can be less messy than gels, creams, or lotions, and are capable of delivering precise dosages. Upon exposure to moist mucous membranes, these films hydrate and undergo a complex set of dynamics including swelling, polymer chain disentanglement, fragmentation, and diffusion.[20–22] In the process of hydration, drug molecules contained within films are released and delivered to the tissue of interest. Microbicides are chemical substances that can be applied either vaginally or rectally to reduce the risk of HIV/AIDS transmission.[23] These substances may be loaded into a wide array of delivery vehicles, and have shown recent promise in clinical trials.[24,25] In order for microbicides to be effective, the drug must have the proper

pharmacodynamic action, but must also be properly administered by the user and must adequately reach the site of intended action. Gels and creams can provide rapid drug delivery and good coverage of the target tissue surface, but are associated with leakage and messiness. Suppository pills and vaginal rings mitigate these to drawbacks, but may not provide adequate coverage and drug delivery to the entire tissue surface. Microbicide film formulations offer a tidy method of local delivery with large surface area, and are therefore being evaluated as options for reducing the risk of HIV/AIDS transmission.[26]

Topical drug delivery films are engineered to produce specific drug release rates and spatial distributions of the active pharmaceutical ingredient (API), which are governed by the hydration and subsequent spreading behavior of the delivery vehicle.[27–29] These products are typically evaluated by measuring macroscopic disintegration and drug release rates as well as the composite film physicochemical properties. While film disintegration testing is performed during product development using standard USP methods, these methods require large volumes of testing medium and do not reproduce *in vivo* fluid kinetics. Visual assessment of dissolution in a volume of fluid comparable to that found in the vagina is a more biorelevant evaluation technique that has been used, however these tests are subjective in nature.[30,31]

Computational models of film hydration and spreading have been developed to investigate the dynamic rheological properties, polymer spreading, and drug delivery

rates.[32] However, as films are designed with more advanced dissolution and delivery characteristics, there is a need for quantitative methods that can verify that film hydration proceeds with the intended spatiotemporal kinetics and is able to adequately deliver APIs to the entire tissue surface.

In an initial pilot study, I demonstrated that transmission QPM can be an effective method for measuring the RI of microbicide film samples as they hydrate.[33] Because microbicide films are semitransparent and are manufactured in thicknesses ranging from tens to hundreds of microns,[26] quantitative phase images of these materials can be processed using appropriate phase unwrapping techniques to recover two-dimensional images of the water-film mixture's RI at each location. In turn, these RI maps indicate the relative quantity of water infiltrating the polymer and are used to track the mass transport of polymer material laterally in the field of view. Having demonstrated the QPM measurement technique, the study presented in Chapter 5 outlines a standardized assay for comparing film samples and develops spatiotemporal analyses to characterize the effects of microbicide film thickness and composition on the polymer dissolution kinetics. The resulting data are expected to be useful in conjunction with mathematical models of film hydration and distintegration[32] to improve the understanding of polymer vehicle behavior and its impact on efficient topical drug delivery.

2.3.2 Red Blood Cell Biophysics

Red blood cells (RBCs) are the simplest of human cells; they lack intracellular organelles and are composed of an aqueous cytosolic mixture of hemoglobin, ions, and other bio-relevant molecules surrounded by a phospholipid bilayer membrane. An underlying spectrin cytoskeleton is anchored to the outer membrane and maintains the strength, shape, and motility of the RBC.[34,35] Despite their relative simplicity, RBCs comprise 45% of blood volume and are responsible for delivering oxygen from the lungs to all other cells within the human body. Efficient delivery relies upon proper circulatory function, which is governed by the fluidity of blood as determined by the cellular interactions between RBCS and their surrounding environments.

As RBCs move from large vessels through narrow capillaries as small as 5-10 μm in diameter[11], they experience shear forces and drastic elastic deformations during their ~120 day lifespan. Decreases in RBC deformability are seen in a wide range of disease states and may play an important role in microvacular occlusion.[36] Many computational and experimental studies of RBCs have been conducted to elucidate the mechanisms underlying the mechanical deformability of individual cells. RBCs are known to exhibit a biconcave disc shape in the absence of shear stresses as well as membrane shape "memory": after deformations by external forces that cause significant shape changes and bilayer membrane shifting above the cytoskeleton, the same parts of the membranes always reform the rim.[37] Subsequent experiments have indentified flow conditions and

shear stresses that result in rolling, tumbling, and tank-treading cell motions[38]. Models and experimental analysis of RBC deformation and cytoskeleton-membrane interactions all assume constant cell surface area (membrane inelasticity) and constant cytosol volume during deformation.[39–41]

Studies of dynamic cell behavior in response to flow make use of two-dimensional intensity images to estimate cell morphology.[38,41] QPM offers a significant improvement over this method of imaging, as it allows volumetric estimation of objects. QPM has previously been used to characterize the temporal fluctuations and viscoelastic properties of static RBCs.[42–45] However, QPM has not yet been applied to study RBC morphology in dynamic environments. In Chapter 7, we make use of an endothelialized microfluidic model of capillaries to investigate the morphological and volumetric changes in response to mechanical deformations.

2.3.3 *P. falciparum* infection of RBCs

P. falciparum is the primary cause of malaria, which affects more than 200 million individuals worldwide.[46] Upon infection, *P. falciparum* enters RBCs and begins to grow from a small ring-shaped parasite (*trophozoite* stage) into a *schizont*-stage organism which can then divide, rupture the RBC, and infect multiple otherwise healthy RBCs. During residence within an RBC, the *P. falciparum* parasite breaks down hemoglobin, incorporating the proteins as it grows. This process releases a cytotoxic iron-based compound (α-hematin or ferriprotoporphyrin IX), which is then sequestered through

dimerization to form inert hemozoin crystals. *P. falciparum* has been observed to consume 50-55% of the hemoglobin in human RBCs, and up to 80% of the RBC hemoglobin in monkeys.[47] In addition to biochemical changes, RBCs infected by *P. falciparum* also exhibit decreased deformability.[48]

QPM has previously been applied to the investigation of RBCs infected by *P. falciparum* to estimate cell and parasite volumes, RIs, and mechanical properties.[49–51] However, spectroscopic changes in individual infected RBCs have not previously been investigated by QPM. In Chapter 6, a pilot study is presented characterizing the structural and spectral changes in RBCs infected by *P. falciparum* using QPS.

2.4 Summary

This chapter has presented background information to provide context for the QPM and QPS instrument development and applications presented in this dissertation. Section 2.1 presented a review of phase-shifting and off-axis digital holographic microscopy techniques and reviewed their advantages and disadvantages. Section 2.2 described recent developments that extend quantitative phase microscopy into hyperspectral quantitative imaging modalities and enable molecular investigation of microscopic samples. Finally, section 2.3 gave background on the three model systems that are investigated by QPM and QPS in Chapters 5 – 7. This information provides a context for the studies presented in subsequent chapters of this thesis.

3 Instrumentation

Chapter 2 presented a review of quantitative phase microscopy systems that use digital holography as well as efforts made to combine spectral information with phase microscopy, and discussed their advantages and limitations. In this chapter, the design, construction, and associated image processing techniques of two instruments that recover high quality phase measurements are presented. The off-axis quantitative phase microscopy (QPM) system outlined in section 3.1was first built to capture high-speed interferograms for investigating temporal dynamics. The methods of off-axis phase retrieval, phase referencing to separate sample phase delays from the optical system's phase contributions, and phase unwrapping are also outlined in this section.

Section 3.2 discusses modifications to this off-axis QPM system that were introduced to enable high-resolution hyperspectral quantitative phase microscopy. The resulting quantitative phase spectroscopy (QPS) instrument sweeps the sample illumination wavelength across the visible spectrum over ~5s, capturing interferograms at discrete center wavelengths with a small but finite spectral bandwidth. The impact of low temporal coherence on the off-axis field of view is discussed, and the procedure for synchronous hologram acquisition and spectral sweeping is detailed. Methods of removing spectral image misalignment and averaging to reduce phase noise are outlined, and a detailed analysis of the resulting spatiotemporal phase sensitivity of the QPS instrument is presented.

3.1 Off-Axis Quantitative Phase Microscopy

3.1.1 System Design

To enable the study of microscopic objects with high temporal resolution, we have developed an off-axis quantitative phase microscope (QPM) capable of recovering phase images from individual holograms (Figure 3.1). A laser with good temporal coherence is used as an illumination source. During development, both a diode-pumped solid state (DPSS) 532nm laser and a helium-neon (HeNe) 632.8 nm laser were tested. In the experiments presented in Chapter 5, light from a HeNe laser is used for system illumination because the temporal stability was found to be far superior to the DPSS laser. The laser light first passes through lenses L1 and L2 and aperture A, which spatially filter the illumination and remove higher order spatial modes. The collimated light enters the interferometer and is split into sample and reference arms by beamsplitter BS1. The sample field interacts with the sample, which is placed in the focal plane of microscope objective MO1. MO1 and tube lens TL form an infinity-corrected imaging system with magnification $M = F_{TL} / F_{MO1}$ which images the sample onto the camera's sensor. Microscope objective MO2 in the reference arm is matched to MO1 to reduce wavefront aberrations, and is also placed in 4F configuration with TL. The reference arm mirror and MO2 are aligned such that the reference beam is centered and parallel to MO2's optical axis; however, the reference mirror and MO2 are translated laterally relative to the TL to create a reference wave incident on the camera

sensor with an angular tilt relative to the sample wave. The sample and reference waves interfere at the detector plane to create an "off-axis" intensity fringe (Figure 3.2 (B)). In addition to the spatially linear phase map, appearing as the intensity fringe, the wave fronts also contain minor aberrations due to the distinct spatial areas of the TL that each traverses as well as optical imperfections throughout the earlier elements of the system. The angle between the beams is adjusted so that each linear fringe covers ~3 pixels on the detector in order to most effectively isolate the spatial frequencies of the beam that interacts with the sample; this selection will be discussed further in section 3.1.2.

In the dynamic QPM experiments presented in Chapter 5, 2.5× objectives (Zeiss A-Plan, 0.2 NA) are inserted as MO1 and MO2, and the TL is selected as a 150-mm focal length achromat (Thorlabs), creating an effective magnification of ~2.28×. A global shutter high-speed USB 3.0 camera (Point Grey, Flea 3.0 FL3-U3-13Y3M-C) is used in these experiments for capturing 1.3 megapixel (MP) interferograms of a 2.0 x 1.5mm sample-plane field of view (FOV). In the remainder of the experimental data presented in Chapters 3.2.5, 6, and 7, the QPS system is occasionally used as a high-speed single wavelength QPM instrument; this mode of operation is further described below in section 3.2.

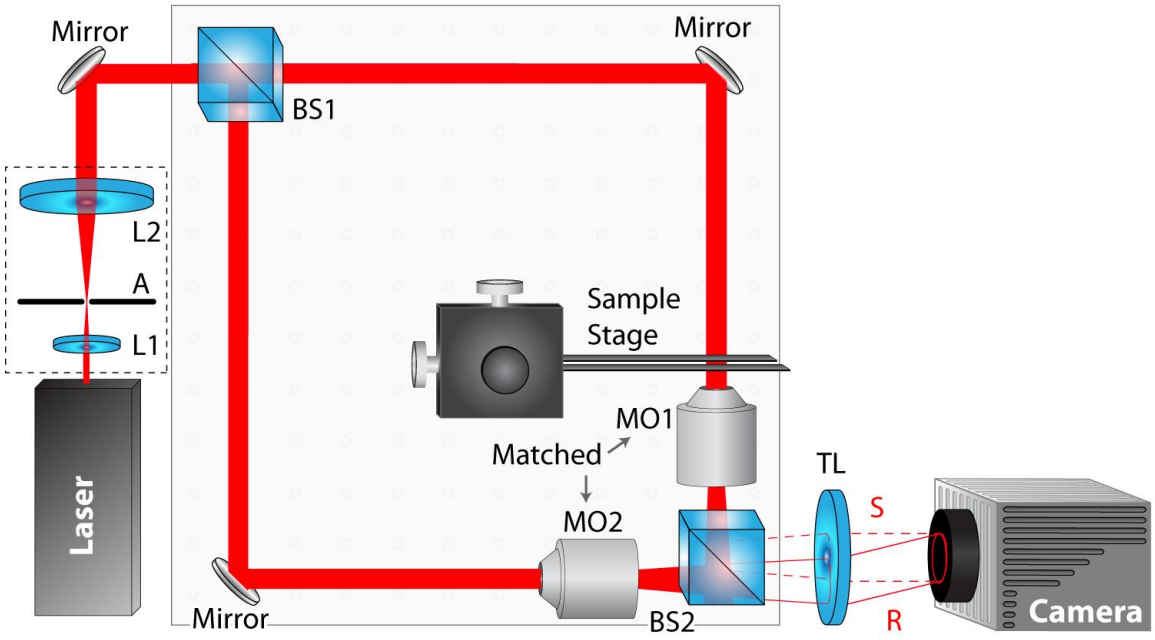

Figure 3.1: Off-axis quantitative phase microscope system design

3.1.2 Off-axis Phase Retrieval: Theory

In QPM, light from a source is split into a sample and a reference arm. The sample arm light passes through a transmissive sample where it accumulates spatially-dependent phase and amplitude modulation. The modulated sample arm light is magnified and recombined with the reference arm light beam before being imaged onto a camera sensor. If the illumination source offers sufficient coherence, an interference pattern is visible and is recorded by the camera as an interferogram. The interferometric superposition of the two beams at the camera plane is written as:

$$I(k,\vec{r}) = \left|E_s + E_R\right|^2 = E_R E_R^* + E_S E_S^* + E_S E_R^* + E_R E_S^* \qquad (3.1)$$

where E_R and E_S are implicit functions of $k = 2\pi/\lambda$ and the spatial coordinate vector, $\vec{r}$. The first two terms of equation (3.1) correspond to the intensities of the reference

and sample fields (autocorrelation terms) while terms 3 and 4 represent cross-correlations between the two. Mathematically isolating the third or fourth term allows subsequent recovery of the complex information of the sample arm electric field.

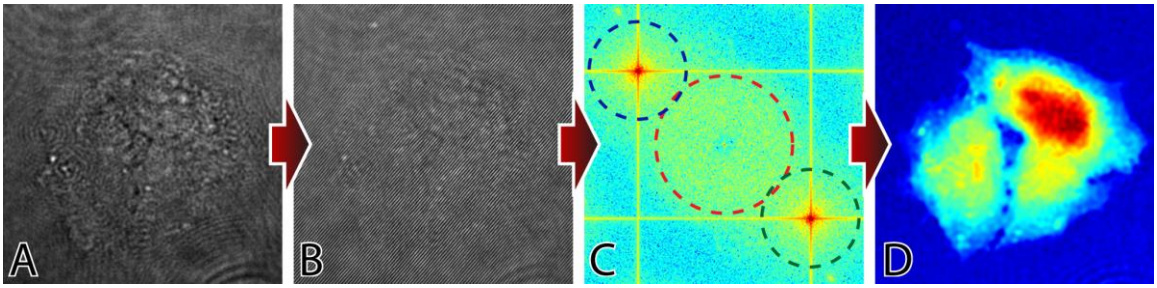

Figure 3.2: Off-axis QPM processing. (A) Brightfield intensity image of rat glioblastoma (GBM) cells; (B) off-axis interferogram of the same cells; (C) two-dimensional spatial Fourier transform of (B) showing the autocorrelation terms (center red), the -1 crosscorrelation term (upper-left blue), and the +1 crosscorrelation term (bottom-right green); (d) quantitative phase image of GBM cells, processing described in the text.

In off-axis DHM, the use of an angular tilt, $\theta(k,\vec{r})$, between the sample beam and the reference beam at the camera plane introduces a spatial carrier (Figure 3.2(B)) into the recorded interferogram that is spatially-analogous to frequency modulation (FM) radio encoding. Assuming that the reference arm has no significant attenuation or phase delays, the reference and sample fields can be written as:

$$E_s(k,\vec{r}) = E_0(k,\vec{r})A_s(k,\vec{r})e^{i\phi_s(k,\vec{r})} \tag{3.2}$$

$$E_R(k,\vec{r}) = E_0(k,\vec{r})e^{i(\theta(\vec{r})\cdot\vec{r})} \tag{3.3}$$

where A_s and ϕ_s are the amplitude and phase modulation imparted on the electric field by the sample.

Substituting equations (3.2) and (3.3) into the third term of equation (3.1) yields:

$$I_3(k,\vec{r}) = \left|E_0(k,\vec{r})\right|^2 A_s(k,\vec{r}) e^{i(\phi_s(k,\vec{r}) - \theta(\vec{r})\cdot\vec{r})} \tag{3.4}$$

Fourier transforming equation (3.4) yields a two-dimensional frequency space (Figure 3.2(C)) in which the angular tilt, $\theta(\vec{r})$, between the sample and reference beams creates a frequency offset, akin to a carrier frequency, modulated by the spatial frequency information of the sample (green dashed circle). Filtering an area surrounding the carrier frequency, recentering the complex information in Fourier space, and inverse Fourier transforming the result yields a demodulated complex data set:

$$G_{filtered}(k,\vec{r}) = \left|E_0(k,\vec{r})\right|^2 A_s(k,\vec{r}) e^{i\phi_s(k,\vec{r})} \tag{3.5}$$

The phase of the complex dataset expressed in equation (3.5) and shown in Figure 3.2(D) can be calculated using the four quadrant tangent function, yielding values between $-\pi$ and π. The phase measurement can further be related to the optical path length (OPL), RI, and total thickness of the sample as:

$$OPL(k,\vec{r}) = \Delta\phi(k,\vec{r}) * \frac{\lambda}{2\pi} = \Delta n(k,\vec{r}) * d(\vec{r}) \tag{3.6}$$

3.1.3 Minimzing system aberrations by wavefront referencing

A quantitative phase microscope measures the difference in wave phase and amplitude between the reference and sample beams. While these two beams may be very similar, they are seldom exactly the same. Therefore, the measured complex wave can be represented as a multiplication of the sample wave before it interacts with the sample by a complex transmission function imparted by the sample:

$$E_{measured} = A_0(x,y)e^{i\varphi_0(x,y)} \cdot A_s(x,y)e^{i\Delta\varphi_s(x,y)}$$
$$= A_0(x,y) \cdot A_s(x,y)e^{i(\varphi_0(x,y)+\Delta\varphi_s(x,y))} \quad (3.7)$$

In order to isolate A_s and $\Delta\varphi_s$, an interferogram of the aqueous chamber with no cells in the field of view is acquired and processed to measure A_0 and $\Delta\varphi_0$. While this removes many of the features inherent in the sample beam, the optical system is not completely free from mechanical drift. Small changes in the system alignment result in spatial "ripples" in $\Delta\varphi_0$ which drift over time. These ripples are removed by subtracting a two-dimensional polynomial from each referenced phase image $\Delta\varphi_s$. This polynomial is fit only to the areas in the field of view that contain no sample features, i.e., only locations without cells.

3.1.4 Phase Unwrapping

Phase measurements in digital holography are typically calculated using the arctangent operation. The signed two-argument arctangent function is inherently limited to a measurement range of $-\pi$ to π, leading to 2π ambiguities when the sample contains features that span more than one wavelength in optical thickness. Many unwrapping algorithms have been developed to remove 2π discontinuities from phase measurements. While these algorithms tend to perform well when evaluating simulated data or specific classes of samples, there are three major constraints: (1) true phase changes larger than π between two adjacent spatial locations are not able to be unwrapped if the algorithm assumes a "smooth" phase profile (many do); (2) noise can

obscure data, resulting in discontinuities that lead to path-dependent residuals and errors in the unwrapped data; and (3) phase unwrapping algorithms tend to be computationally-intensive, and the required time to complete the unwrapping process grows nonlinearly with the size of the spatial phase dataset.

Many two-dimensional (2D) phase unwrapping algorithms have been developed to mitigate the effects of these three constraints. Classical algorithms maximize robustness against noisy data while aiming to minimize computation time.[52–55] One alternative to 2D spatial unwrapping is temporal phase unwrapping at each pixel: this 1D unwrapping method is a substantially faster than 2D algorithms, and is applied to systems where relative phase deformations over time are of interest.[56] All of these algorithms are limited by the assumption that the phase change between each spatial or temporal point is less than π. When examining samples with sharp features that create large phase changes between adjacent points, the measurement range of phase microscopy can be extended through the use of two or more wavelengths.[57–63] These techniques have noise-considerations, however the effective measurement range may be extended to the "beat wavelength" between the closest two illumination sources. Several of these techniques have been developed to multiplex holographic measurements at multiple wavelengths simultaneously on the same camera sensor, trading spatial bandwidth for extended phase measurement range but also allowing single-shot operation and characterization of dynamically changing samples.[63–66]

Finally, some phase retrieval methods are not inherently limited to a measurement range of $-\pi$ to π. One approach recovers phase information free from wrapping by solving the transport of intensity equation[67] with three images that have been defocused by different amounts.[68] Another method introduces a quadratic phase term with a dispersive element to measure phase differentials that may be integrated to yield unambiguous phase information.[69] More recently, researchers have developed a processing technique for phase data acquired from common-path spectral-domain OCT measurements that recovers unambiguous phase information over a range of 2mm by spectral filtering.[70]

3.1.4.1 Simultaneous Two-wavelength Phase Unwrapping with a Color Camera

We have developed a simple optical system that employs a color camera to capture off-axis interferograms at two wavelengths simultaneously to be used for two-wavelength phase unwrapping. While several instruments designed for two wavelength phase unwrapping use complicated interferometers with separate reference arm optics for each wavelength to multiplex complex information in the Fourier plane of the hologram[64–66], our approach uses a color camera to spectrally separate interferograms that have identical reference wave off-axis angles.[63]

Two laser beams (HeNe 632.8 nm and DPSS 532nm) are spatially-overlapped and combined with a beamsplitter prior to entering the optical system shown in Figure 3.1 at Lens L1. MO1 and MO2 are selected to be infinity-corrected 40× objectives

(Newport, L-40X, NA = 0.66) to produce holograms of microstructures with diffraction-limited resolution of 0.492 μm and 0.585 μm (d=0.61λ/NA) at the two imaging wavelengths. Interferograms are recorded on a Bayer-mosaic color camera (12-bit Coolsnap *cf*, Roper Scientific) with 1392x1040 4.65 μm square pixels. The red and green color channels of the camera effectively separate the HeNe and DPSS intensity interferograms, with ~5% spectral crosstalk between channels.

After recovering OPL maps from the phase images at each of the two wavelengths according to methods in sections 3.1.2 & 3.1.3, an OPL map at the synthetic beat wavelength, Λ, of 3.334 μm ($\Lambda=\lambda_1\lambda_2 / |\lambda_1 - \lambda_2|$) is calculated. The OPL map at Λ is free of wrapping artifacts over an OPL range of 0 – 3.334 μm, but contains amplified noise; using this map as a guide for unwrapping the 532nm OPL maps retains the lower noise of the individual OPL image while extending the unambiguous measurement range to Λ.[61]

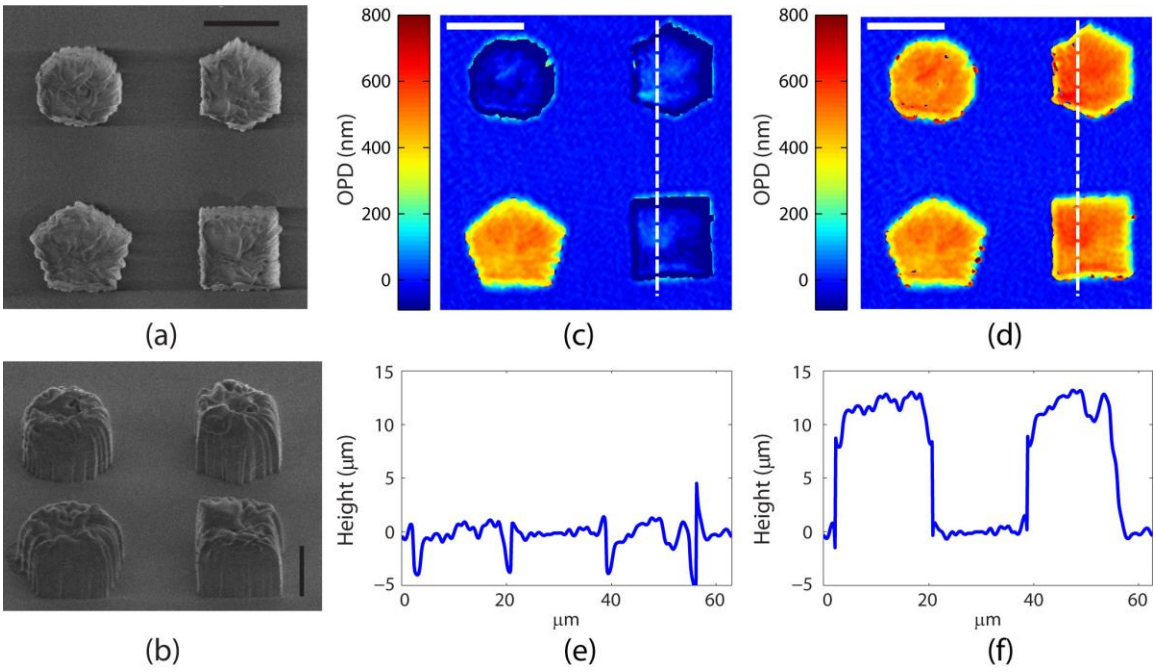

Figure 3.3: Microstructure OPL and height profiles. (A) *en face* SEM image, (B) 45° SEM image. (C) 532 nm OPD map after quality-map guided unwrapping, (D) 532 nm OPD map after two-wavelength unwrapping. (E) incorrect object height profile, from the dotted line in (C); (F) object height profile from two-wavelength unwrapping, from the dotted line in (D). All scale bars are 15μm. Taken from Rinehart, *et al.*[63]

The performance of this simultaneous two-wavelength transmission phase microscope is validated by measuring polymer microstructures with OPL changes larger than either individual wavelength and comparing the results of the two-wavelength unwrapping algorithm to a well-known quality-map guided unwrapping algorithm[52]. The microstructures are constructed by holographically patterning[71] a ~10 μm-thick layer of UV-cure optical adhesive (NOA 63, n = 1.56, Norland Products) on a glass substrate, and are immersed in index-matching oil (n = 1.515) for evaluation. Figure 3.3 (A) & (B) shows representative SEM images of the microstructures, and compares the OPL and

height profiles of the microstructures calculated after traditional phase unwrapping (Figure 3.3 (C) & (E)) to those calculated after two-wavelength unwrapping (Figure 3.3 (D) & (F)). The quality-map guided algorithm fails to correctly unwrap the phase for three of the four structures, while the two-wavelength algorithm correctly measures the phases of all of the microstructures. Some errors remain at individual points at the edges of the microstructures, which are due to local noise[64,72], however almost all of the image points are accurately reconstructed and the unwrapped OPL image at 532nm retains the same background noise characteristics of the wrapped OPL image (σ = 13.8nm over a 100 x 100 pixel region).

3.2 Quantitative Phase Spectroscopy

QPM is extended to capturing spectroscopic holographic data by modifying the system design shown in Figure 3.1 to use a broadband illumination source with an appropriate tunable spectral filter and by syncing the camera's acquisition to the source's wavelength step. The following subsections detail the design of the resulting quantitative phase spectroscopy (QPS) instrument, discuss the theory and implications of finite-bandwidth illumination filtering, and finally present the signal conditioning steps used to produce hyperspectral phase images of microscopic samples. The system described here is used to acquire spectra that are analyzed in sections 4.3 & 4.4; it is also used to acquire data both in a spectroscopy mode and a single-wavelength high speed imaging mode which are analyzed in Chapters 6 & 7.

3.2.1 QPS Microscope Design & Alignment

QPS is implemented using a modified Mach-Zehnder off-axis interferometer similar to the system presented in Figure 3.1. The laser input is replaced by the spectrally-filtered output of a supercontinuum light source (SC450-2-AOTF, Fianium) with high spatial coherence (Figure 3.4). After spectral filtering (described in-depth below), the illumination light has a finite bandwidth, on the order of 1-5 nm, with a slight spatial variation with center wavelength. Therefore, the light is coupled into a single-mode fiber (Thorlabs, S405-XP) with its output recollimated by MO1 (Zeiss, 10× Achroplan) and passed through linear polarizer LP such that the output remains at a single location. The interferometer splits the incident light into sample and reference beams as in the QPM system, and uses matched 40×, NA = 0.75 microscope objectives MO1 and MO2 (Zeiss, Neofluar) with a high degree of lateral chromatic aberration correction. In this system, the tube lens used earlier is removed in order to minimize chromatic aberration mismatch between the interferometer arms. Instead, the camera is placed at a distance from the MOs that produces a ~108× optical magnification, creating oversampled images that retain diffraction-limited resolution after off-axis spatial filtering. Interferograms are captured by a 12-bit high-speed CMOS camera (Fastcam SA4, Photron) with 20-μm pixels and a 1024x1024 sensor. In the experiments presented here, a 512 x 512 region is recorded, corresponding to a field of view of ~95.2 × 95.2 μm in the sample plane. The integration time is adjusted within a range < 1ms to maximize

the dynamic range without overexposing any pixels. MO2 and the incident beam are aligned so that the reference arm intensity pattern remains centered on the camera across an illumination range of 460 – 720nm.

After initial alignment, captured interferograms are used to fine-tune the system alignment. Retroreflectors (RRs) coarsely match the pathlength of the interferometer arms, while a motorized axial translator on the reference arm RR allows for fine path length matching and adjustment of the system to account for added path length when samples are placed in the system. Once the system is pathlength-matched, the bottom reference arm mirror and MO2 are laterally translated to produce a linear off-axis fringe with 1 cycle / 3.5px at λ_0 = 500nm and 1 cycle / 5.76px at λ_0 = 720nm to optimally use the camera's spatial frequency bandwidth for off-axis interferometry.[73] Note that the fringe spatial frequency is linearly related to the center wavelength, as is described below in section 3.2.2. MO2 is then translated axially along its optical axis until the wavefront curvature mismatch of the two arms is minimized. Because the optical system is slightly sensitive to polarization, the linear polarizer at the input of the interferometer is rotated to maximize the fringe efficiency and finally the polarization controller (PC) paddles are adjusted to maximize the system's intensity throughput.

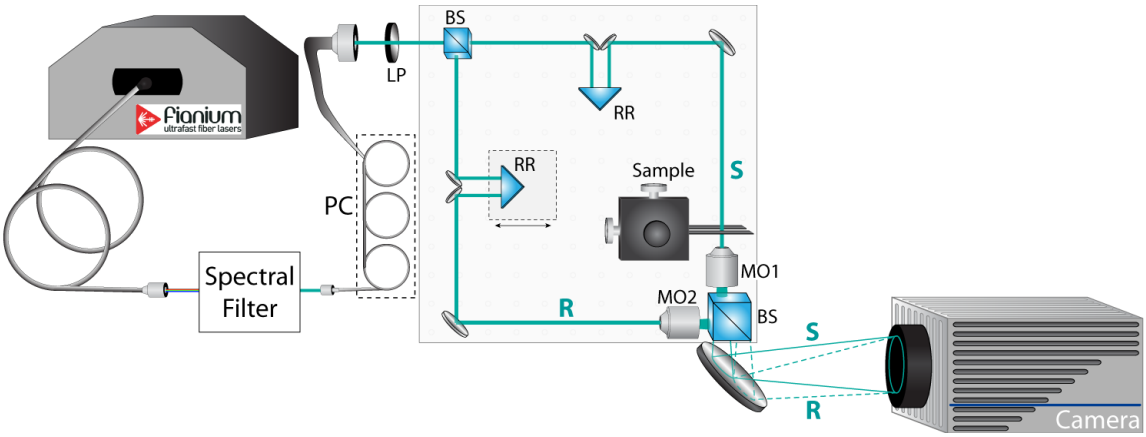

Figure 3.4: QPS System Design

The QPS system initially was constructed using a rapidly tunable acoustooptic spectral filter controlled by a programmable frequency synthesizer (iDDS-2-SE, Isomet), with a FWHM bandwidth ranging from 2.9 nm at λ_0 = 460nm to 8.5nm at λ_0 = 700nm (Figure 3.5 (A)). This filter was replaced with a custom-designed tunable filter (Figure 3.5 (B)) consisting of a diffraction grating (Thorlabs, 600 lp/mm, GT25-06V) that is imaged by a 4F system onto a galvo scanning mirror. Rotating the mirror changes which center wavelength is coupled into the single-mode fiber. This new tunable filter decreases the illumination linewidth to a constant $\delta\lambda$ = 1.12 nm regardless of the center wavelength, which increases the coherence length of the illumination light significantly. Center wavelengths and bandwidths for each filter were measured by coupling the single-mode fiber into a high resolution spectrometer with a 5-μm pinhole for an entrance aperture (HR4000, 388-843nm, 0.125nm resolution, Ocean Optics). The implications of the spectral bandwidth are discussed in Section 3.2.2. Both the acousto-optic filter and the galvo mirror are controlled by a LabVIEW interface, which either sets

a static center wavelength or steps the wavelength and outputs a TTL camera trigger while the wavelength is held constant.

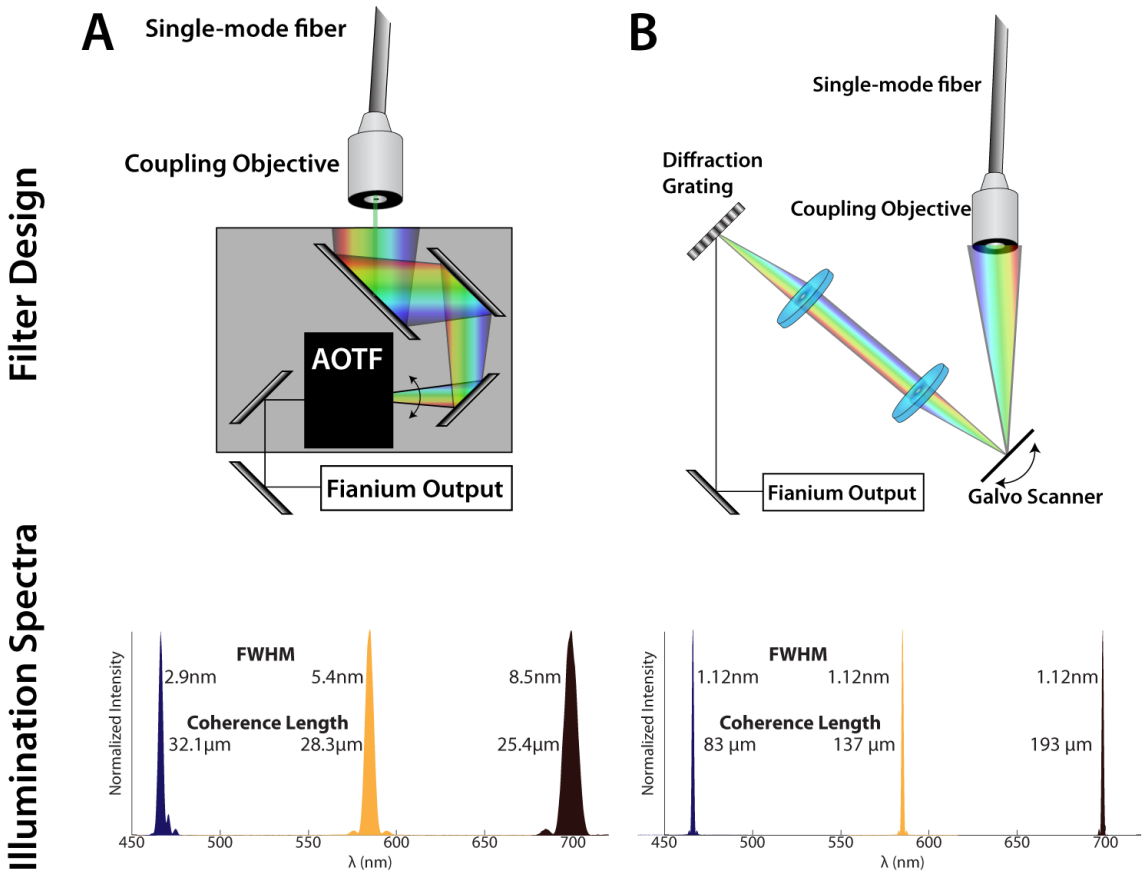

Figure 3.5: Spectral filter designs and resulting spectral bandwidth characteristics.

3.2.2 Low-coherence off-axis interferometry

The cross-correlation term of the interference presented in equation (3.4) can be rewritten as $I_{INT} \propto \mathrm{Re}\left\{e^{i(k\vec{\theta}\cdot\vec{r}+k\delta z+\Delta\varphi(k,\vec{r}))}\right\}$ to include a phase term accounting for the average optical path length (OPL) difference between the two interferometer arms, δz.

This term can be ignored when the temporal coherence of the illumination source is long relative to the delays measured across a field of view, however must be considered when illumination a sample with a source with finite bandwidth. Modeling the source bandwidth as a Gaussian distribution yields a detected interference term that is integrated across the wavenumber spectrum:

$$I(k,\vec{r}) \propto \int_0^\infty e^{\frac{-(k-k_0)^2}{\delta k^2}} \operatorname{Re}\left\{e^{i(k\vec{\theta}\cdot\vec{r}+k\delta z+\Delta\varphi(k,\vec{r}))}\right\} dk \tag{3.8}$$

Here, δk is a measure of the spectral bandwidth of the illumination and $k_0 = 2\pi/\lambda_0$ is the center wavenumber. Assuming a small bandwidth across which the wavenumber is approximately constant and the spectral dispersion of $\Delta\phi$ is minimal allows the phase delays of the sample to be written as $\Delta\phi(k_0,\vec{r})$. Integrating the remaining terms yields:

$$I(k,\vec{r}) \propto \operatorname{Re}\left\{e^{i\Delta\varphi(k_0,\vec{r})} \cdot e^{-ik_0(\vec{\theta}\cdot\vec{r}+\delta z)} \cdot e^{\frac{-(\vec{\theta}\cdot\vec{r}+\delta z)^2\delta k^2}{4}}\right\} \tag{3.9}$$

The first exponential term in equation (3.9) describes the relative phase delays of the sample object, the second term captures the high-frequency spatial carrier, and the third exponential term describes a coherence envelope that modulates the amplitude of the complex interferometric information. This spatial fringe visibility envelope as well as the angular carrier frequency are determined by $\vec{\theta}$; for a given spectral bandwidth δk, a fixed number of fringes are visible with high interferometric efficiency.

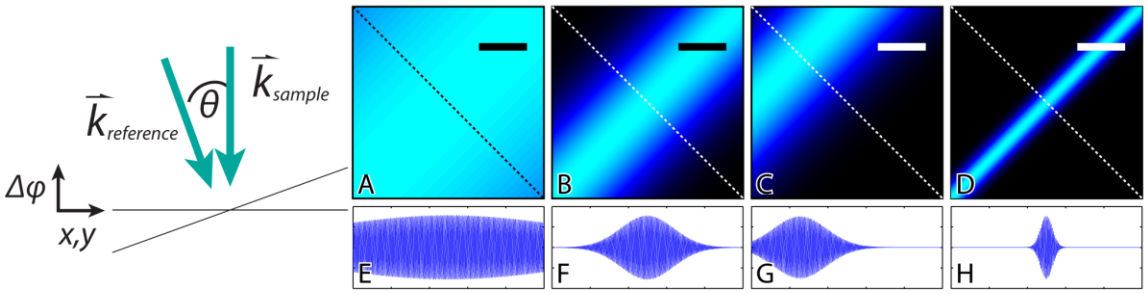

Figure 3.6: Simulation of the effects of low coherence illumination on off-axis QPM carrier frequency (λ_0=500nm): (A-D) Amplitude of complex envelope (term 3 of Eq. 2) of the interference cross-term. (E-H) High-frequency spatial modulation (term 2 of Eq. 2) cross-sections from dotted lines in corresponding (A-D). (A,E) δz = 0μm, δλ = 1nm; some roll-off of amplitude is seen. (B,F) δz = 0μm, δλ = 5nm; amplitude roll-off obscures signal at edges of field of view. (C,G) δz = 20μm, δλ = 5nm; peak of coherence envelope moves across field of view due to path length offset. (D,H) δz = 0μm, δλ = 22nm; large bandwidth severely limits field of view. Note that the angle between the sample and reference beams, and hence the spatial carrier frequency, are fixed in all of these figures. Lateral scale bars: 50 μm. Adapted from Rinehart, *et al.*[17]

Figure 3.6 simulates the relationship between off-axis angle and the resulting complex envelope for a range of bandwidths δk and average OPL differences δz between the interferometer arms. Increasing the spectral bandwidth from 1nm to 5nm reduces the fringe visibility at the edges of the field of view, while increasing the bandwidth to 22nm (roughly 1/10th the spectral range measured during QPS hyperspectral sweeps) reduces the usable field of view to a small stripe only tens of microns across. Figure 3.6 (C) & (G) also illustrate the importance of path-matching the interferometer: a 20 μm path difference between the interferometer arms shifts the coherence envelope from the center of the field of view to the edge of the field of view. The decrease in fringe visibility at the edges of the field of view results in decreased phase sensitivity.[74] The

use of diffractive optics to create an off-axis reference without introducing this spatially-dependent envelope effect when illuminating samples with wide spectral ranges.[75,76]

3.2.3 QPS Hologram Acquisition

The QPS instrument is used in both a single-wavelength "static" mode and a spectral sweep "spectroscopy" mode. In the static mode, the center wavelength is set to a specific value and held constant. The camera is then software-triggered to begin data collection. In these experiments, the center wavelength is typically either set to λ_0 = 532nm or λ_0 = 589nm. When using these wavelengths and the grating-galvo spectral filter design, the light throughput is high enough to enable a 0.5 ms integration time and the camera records holograms at a user-defined rate up to 2000 frames per second (fps).

In spectroscopy mode, the LabVIEW custom VI steps the spectral filter to the desired center wavelength and then triggers the camera to burst-acquire 4 images with a 0.5 – 1 ms integration time, set to maximize dynamic range without overexposing any pixels during the entire wavelength sweep. The galvo mirror requires a 7 ms delay between step signaling and camera acquisition to fully change and stabilize; this is realized by triggering both the step and acquisition simultaneously and programming a 7 ms acquisition delay in the camera software (Photron Fast Viewer, PFV). Each spectral step is separated by 15 ms to allow for acquisition. In the experiments described in section 4.4 and Chapters 6 & 7, the spectral filter is tuned from 475 nm to 700 nm in 5 nm steps (48 spectral points), and is swept 8 times for each experiment, with a 50 ms delay

at the end of each sweep to allow the galvo mirror to travel from one end of the spectrum back to the other. Repeated sweeps result in 32 holograms acquired at each center wavelength. The combination of a short burst of interferograms along with multiple sweeps allows the use of averaging to reduce slow drift noise of the interferometric system. In total, the spectral acquisition of a single sample takes ~6s.

The camera records all interferograms (1568 total) to on-board memory, which is then read out to the computer after the full spectral acquisition. Each off-axis interferogram is then processed as follows: the carrier frequency location is measured once for each wavelength and then used for Fourier domain filtering and recentering of the interferometric term (equations (3.1) - (3.4)). Each wrapped phase image is referenced to the phase of a small spatial location (because the average phase drifts over the acquisitions), and is then put into complex form $C_{temp}(x,y) = e^{i\Delta\varphi(x,y)}$ before being summed to produce an average. The arctangent is computed from this average to recover the averaged phase image. Averaging in this fashion avoids creating noise in the averaged phase image from phase wrapping occurring at different spatial locations in individual phase images. A background set of hyperspectral holograms at a nearby feature-free location is used to reference averaged phase images at each wavelength, and polynomial surfaces are fitted and removed as described in section 3.1.3. Amplitude images are averaged across all repeated measurements at each wavelength, and are similarly referenced to the amplitude images of the background holograms.

3.2.4 FOV Resizing and Alignment

The QPS system magnification changes slightly across the visible range of acquired wavelengths, and there is a very slight lateral shift in the field of view. These errors are quantified from a set of hyperspectral interferograms of a USAF test target, group 7 elements 2-6. Holographic information was first extracted as described above and upsampled by a factor of 30 for precision alignment. Then, binary masks of the amplitude images were calculated and the area within elements 2-6 were measured. The hologram taken at λ_0 = 475 nm had the smallest field of view (95.2 x 95.2 μm as determined by measuring the USAF element 5-bar widths), and was used to calculate the relative magnification and resize each of the remaining spectral channels. The normalized cross-correlation between the resulting magnified images (all different sizes) and the 475 nm amplitude image was then used to define beginning and ending coordinates for aligning the fields of view. Finally, all fields of view are cropped to the area of the 475nm field of view. The magnifications and cropping parameters were saved and applied to each hyperspectral dataset.

3.2.5 Noise

The QPS interferometric system is inherently "noisy" despite being constructed on an air-floated vibration-dampening table. Even in an enclosed system, mechanical vibrations, temperature-dependent changes in the air's RI, and density-dependent changes in the air's RI caused by airflow cause the average path length between the two

interferometer arms to drift, and change the exact location of each beam on the camera. Therefore, each frame's phase information is only an accurate measurement of relative path lengths across the field of view.

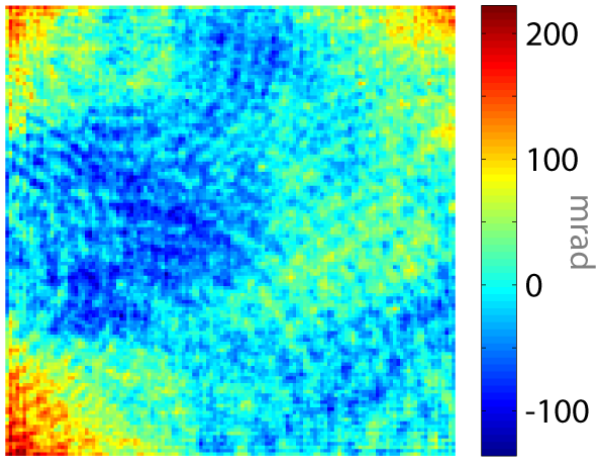

Figure 3.7: Background phase image averaged over 5000 frames (10s). This serves as the subtractive reference for the phase images used to compute the temporal fluctuation maps displayed in Figure 3.8.

Referencing each frame to a point or area accounts for average path length differences; however, lateral deviations of the interfering beams on the camera creates some structure to the remaining noise. Furthermore, the wavefronts are approximately Gaussian in shape with matched magnification, but contain other wavefront structure including non-static spatial mode patterns, laser noise (speckle), and diffraction or multiple reflection artifacts arising from imperfect optics in the system and temporal drift in the exact beam paths (Figure 3.7). In the constructed QPS system, there is significant structure to the background phase images, with a range of 358 mrad, a spatial

standard deviation of σ = 44.6 mrad, and temporal deviations of σ_{avg} = 5.1 mrad across the field of view after subtracting a first-order polynomial surface.

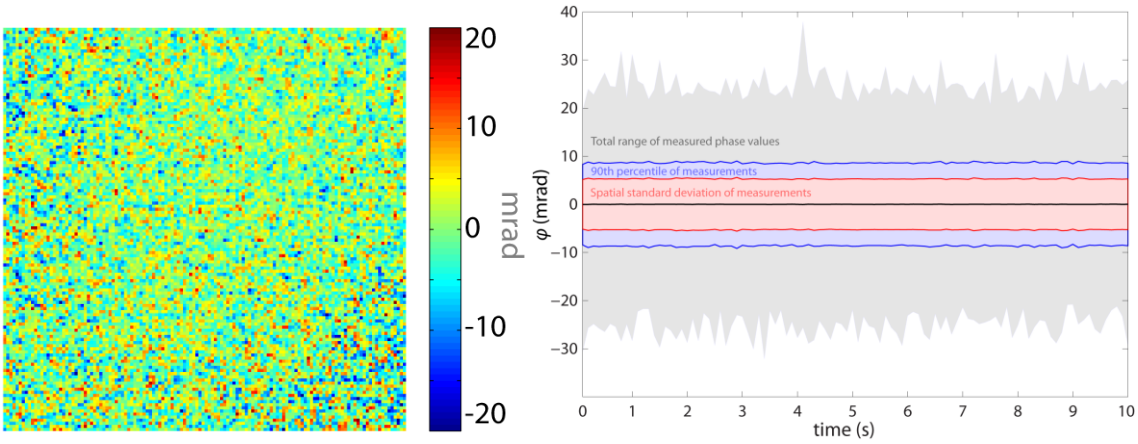

Figure 3.8: Spatial deviations of phase images, with no sample present and both a background phase image and first-order polynomial surface subtracted. (A) A single frame within the time series, $\sigma_{x,y}$ = 5.3 mrad (0.46 nm). (B) For each frame (100 total), the total phase range is shown in gray; the blue region indicates the range in which the middle 90% of values fall; the red region bounds $\pm\sigma_{x,y}$.

3.2.5.1 Spatial Noise

In order to characterize the spatial accuracy & uncertainty of the QPS system, 5000 frames over 10 s were captured at λ_0 = 550nm with a 2 ms integration time (maximizing camera dynamic range, incident power of ~150 μW) and all processed using the methods described above. The temporally-averaged phase image (Figure 3.7) as well as a first-order polynomial were subtracted from each of the frames, isolating the spatiotemporal noise seen in Figure 3.8 (A). Figure 3.8 (B) shows the maximum range (~45 mrad) and spatial standard deviation (~5.3 mrad) of one frame (taken every 0.1 s for 10 s). The measurement accuracy of the QPS system at any one time is limited by this

noise, which may originate from statistical shot noise, non-optical sources (CMOS camera electrical noise, read noise, dark noise, pixel-to-pixel nonlinearity), or possibly spatial structure induced by the temporal drift of the interferometer.

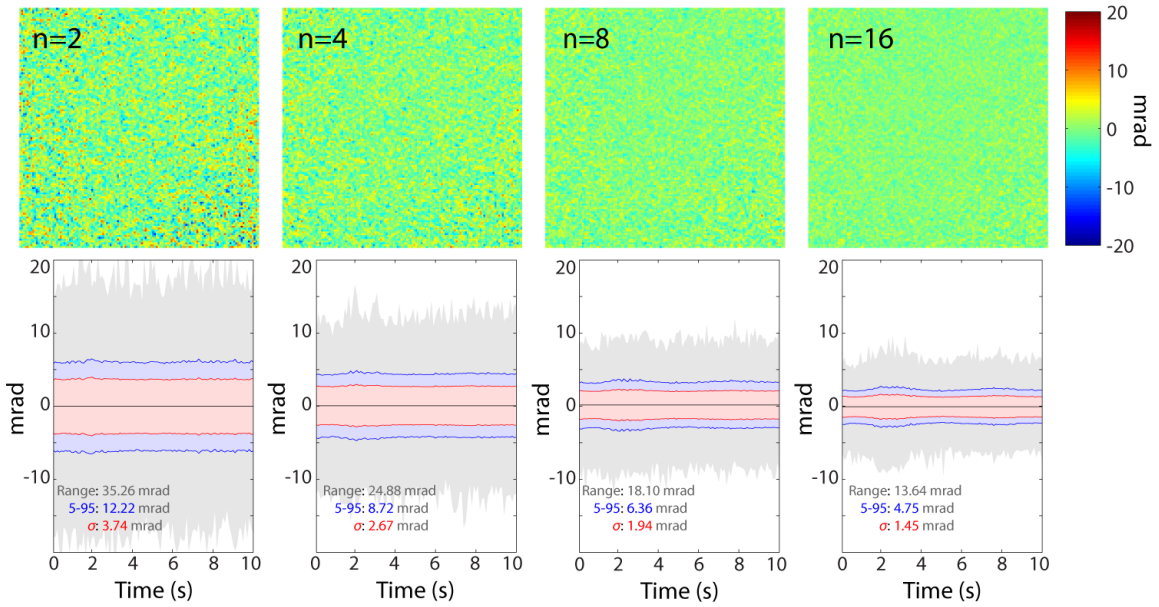

Figure 3.9: Spatial noise across a field of view, 2-, 4-, 8-, and 16-frame averages. Lower row: each time-point's statistics correspond to one n-frame averaged phase image. 5-95 value gives the range that 90% of the total pixels fell between and is a better representation of quantitative imaging than the commonly-reported standard deviation and is not affected by outlying noise pixels.

Because the camera sensor has a finite dynamic range (12-bits, 62.18 dB SNR), multiple phase images must be acquired and averaged to reduce the overall spatial noise. Every 2*n images averaged result in a ~6dB improvement in raw image SNR, corresponding to one extra bit of sensor dynamic range. In Figure 3.9, this effect is demonstrated by averaging 2, 4, 8, and 16 phase images from each 100 ms timespan. The top row shows representative subtracted phase images, and the bottom row shows

corresponding temporal behavior of the spatial phase statistics, demonstrating a decreasing noise amplitude with averaging. The non-averaged phase image in Figure 3.8 has a range of ~45mrad (4 nm) and $\sigma_{x,y}$ = 5.3mrad (0.464 nm); combining 16 images required 32ms of total acquisition time and yields an average range of just 13.6mrad (1.19 nm) and σx,y = 1.45mrad (0.127 nm).

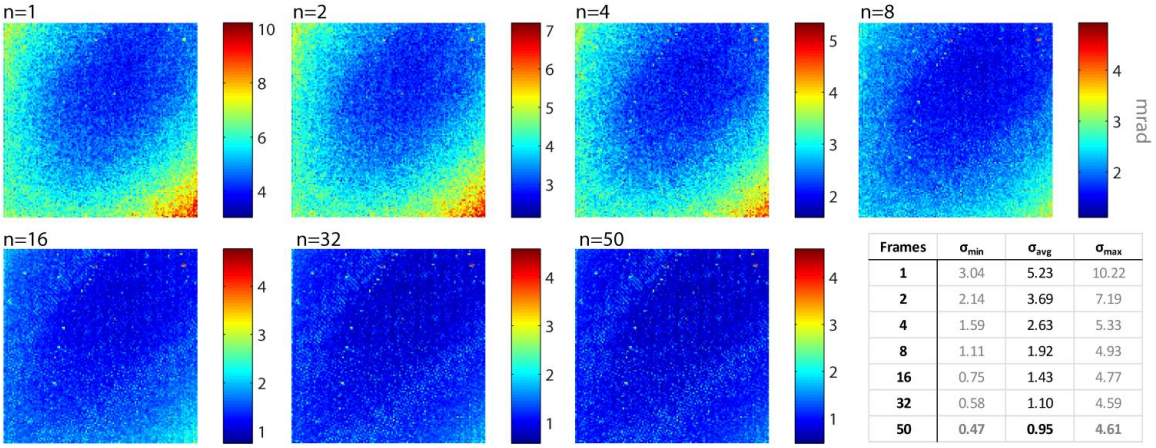

Frames	σ_{min}	σ_{avg}	σ_{max}
1	3.04	5.23	10.22
2	2.14	3.69	7.19
4	1.59	2.63	5.33
8	1.11	1.92	4.93
16	0.75	1.43	4.77
32	0.58	1.10	4.59
50	0.47	0.95	4.61

Figure 3.10: Temporal standard deviation images, <σt>(x,y). As n approaches its maximum value (50) for the 100ms time steps, the average temporal noise across the field of view approaches 0.95mrad, or 83pm of optical path length.

3.2.5.2 Temporal Noise

In addition to spatial noise reduction, the temporal noise can also be reduced by multi-frame averaging. Figure 3.10 shows spatial maps of the temporal standard deviation of the phase image sequences averaged over 1-50 frames, indicating that the temporal noise characteristics at each pixel also improve as *n* increases. The temporal deviation images are scaled relative to their maximum and minimum values; therefore

the spatial shape of the noise is indicative of the relative contributions across the field of view.

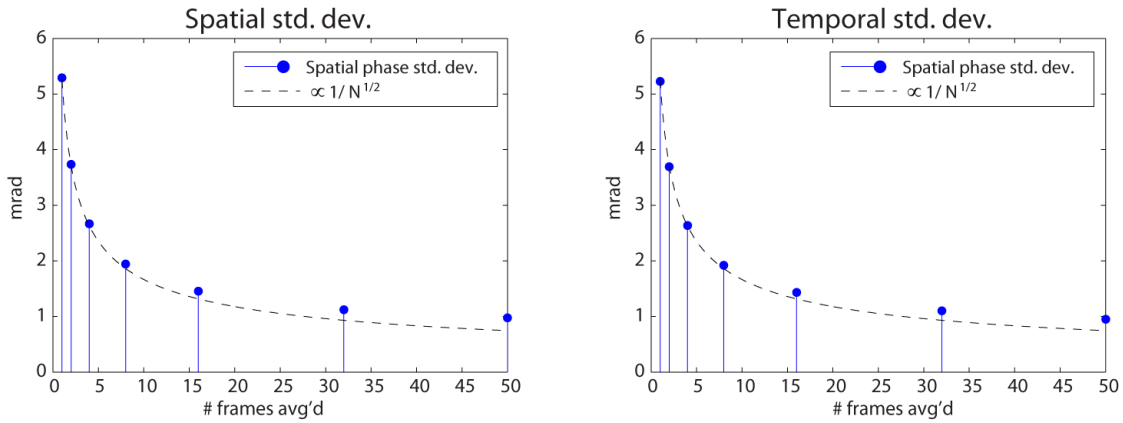

Figure 3.11: Summary of noise. Both the spatial and temporal noise decrease proportional to $1/n^2$ when averaging n frames.

At low n-values, the temporal noise across the field appears to be inversely proportional to the magnitude of the carrier fringe, as shown in Figure 3.12, suggesting that the temporal stability of a single phase image is limited by the number of photons collected (shot noise). There is a similar trend in the spatial deviations in Figure 3.9, although it is not immediately apparent due to the contrast of the display color scale of the image. Averaging beyond 4 frames begins to reveal spatial structure (vertical striping) and hot spots associated with the camera sensor's pixel-by-pixel calibration. A transition occurs between n = 16 and n = 32, and the noise pattern begins to deviate from the shape of the fringe envelope. This suggests that averaging beyond n = 16 reduces the effect of shot noise to the point that it is no longer the dominant source of noise.

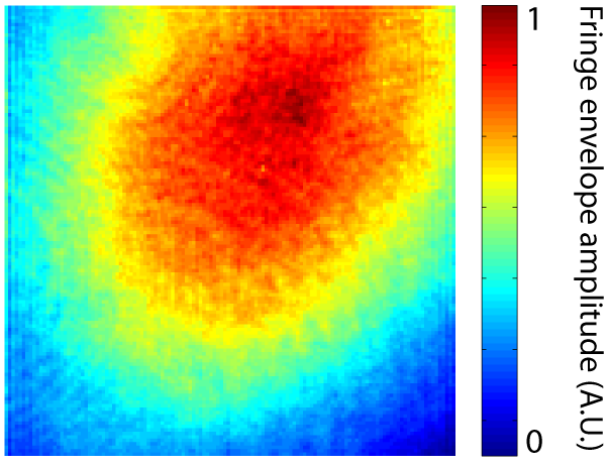

Figure 3.12: Interferometric fringe amplitude.

Averaging for the purpose of noise reduction can be performed at multiple different points in the phase image processing. There are two nonlinear operations in holographic phase retrieval that transform the noise characteristics of the captured interferograms: (1) spatial filtering and recentering in Fourier space, (2) taking the angle of the complex data. Phase images presented above are averaged after phase has been computed and unwrapped. If sequential phase images contain wrapping artifacts at different spatial locations, then averaging the images will result in "noise" that is not able to be removed by subsequent phase unwrapping (discussed in 3.2.3). Averaging complex information before taking the arctangent mitigates this effect, and is substantially faster because unwrapping can be performed on one averaged phase image rather than each image prior to averaging. However, averaging the complex signals before taking the angle can erode the noise benefits of averaging if the complex signals are far out of phase from one another.

In the experiments presented in here, averaging the complex information after filtering degraded the average spatial deviations by ~0.01mrad, the 5-95 deviations by ~0.02mrad, and the overall range of the spatial deviations by ~0.1mrad. The maximum temporal standard deviations were also degraded by 0.05-0.08mrad as more shots are averaged. Averaging the raw interferograms prior to spatial-filtering appeared to have the same effect as averaging the complex information. While the most efficient method of processing from a time standpoint is averaging raw interferograms, both this approach and averaging the complex information risk degradation of phase sensitivity. These effects are on the order of 10s of picometers for the data analyze here, and therefore are negligible for the current system. However, if a future system is optimized to further reduce noise to the picometer level, then the exact method of averaging will likely need to be reexamined.

3.2.5.3 Spectral Noise

The previous subsections analyzed the spatiotemporal noise of the QPS system when run in a "static" mode at a single wavelength. Here, the spectral noise that appears when operating the QPS instrument in a spectroscopy mode is characterized. As detailed in section 3.2.3, the QPS system captures a burst of 4 interferograms at each wavelength, and "sweeps" through wavelengths 8 times, resulting in 32 interferograms acquired at each wavelength (5nm steps from 475 – 700 nm). The phase and amplitude information of these 32 interferograms is then averaged to reduce noise. A reference

hyperspectral dataset of a background area is subtracted from the sample's phase images.

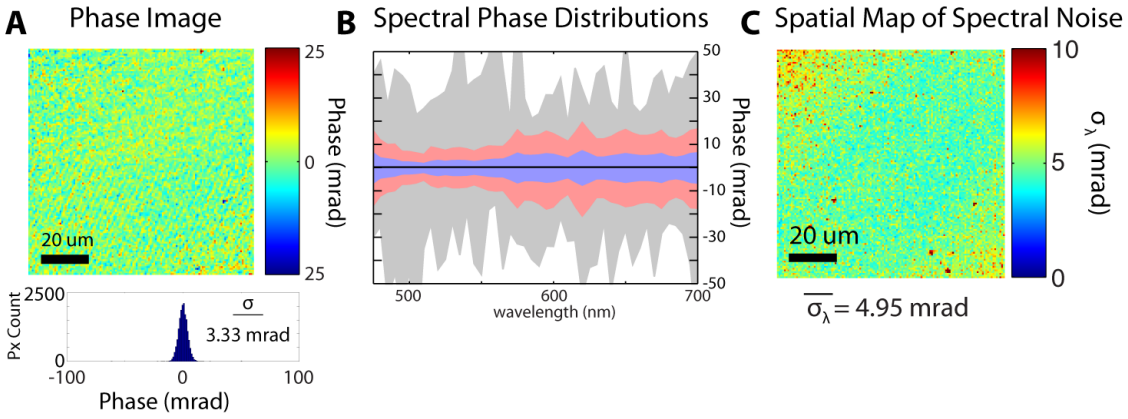

Figure 3.13: Characterization of spectral phase noise with background-subtraction and 1st order polynomial removal. (A) phase image at λ_0 = 550 nm. (B) Spectral plot of the spatial phase distributions at each wavelength. Blue area indicates $\pm\sigma_{xy}$, red area shows the 99th percentile range of all pixels, and grey shows full range of all pixel values. (C) Spatial map of the spectral noise, σ_λ.

To characterize the performance of the QPS instrument in spectral mode, two hyperspectral interferogram datasets are captured with no sample present. Figure 3.13 (A) shows the resulting phase image at λ_0 = 550 nm after phase referencing and additional 1st order polynomial subtraction to remove any "tilt". The distribution in the histogram below this image shows an approximately Gaussian spatial noise distribution with a standard deviation of σ_{xy} = 3.33 mrad. The spatial noise distributions of all wavelengths captured are summarized in Figure 3.13 (B), showing that the spatial noise has some dependence on wavelength due to spectral variation in illumination intensity (blue region shows ± σ_{xy}, red region shows 99th percentile of all pixel-values). The

average spatial noise across wavelengths is $\overline{\sigma_{xy}} = 4.88 mrad$ and remains below $\overline{\sigma_{xy}} = 7.64 mrad$ for all wavelengths. While Figure 3.13 (A) & (B) characterize the spatial noise at each wavelength, Figure 3.13 (C) examines the spectral noise, σ_λ, at each pixel across the field of view. The spectral noise is worse at the edges of the FOV where the interferometric amplitude is low (Figure 3.12); this agrees with the trend seen in the spatial mapping of the temporal noise (Figure 3.10). The average spectral noise across the FOV, $\overline{\sigma_\lambda} = 4.95 mrad$, is in good agreement with the average spatial noise in each wavelength, $\overline{\sigma_{xy}}$.

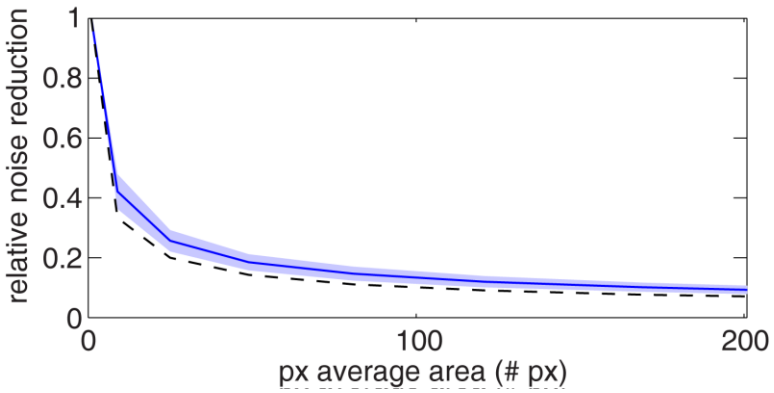

Figure 3.14: Spectral noise reduction achieved by averaging within spatial regions of increasing areas from the FOV analyzed in Figure 3.13. Black dotted line indicates 1/sqrt(n) ideal noise reduction. Blue solid line and light blue region show the average and standard deviation in relative noise reduction when comparing multiple regions across the FOV.

The spectral phase noise can further be reduced by averaging spectra across an area of an image. To demonstrate this effect, the spectra from the data shown in Figure 3.13 were averaged over areas ranging from 1x1px up to 19 x 19 px (361 px^2 area). The

resulting spectral noise, σ_λ, over each area was then normalized by the average single-pixel spectral noise within that area. Figure 3.14 shows the relative spectral phase noise reduction achieved by averaging measurements over progressively larger regions. The black dotted line shows the expected 1/sqrt(n) decrease that would be expected when averaging uncorrelated noise, while the blue line shows the relative noise averaged over 144 separate areas in the field of view (light blue area shows standard deviation of the noise reduction across these areas). For reference, an individual RBC laying flat may occupy ~90 pixels. While there is some discrepancy between the measured noise reduction and a perfect 1/sqrt(n) improvement, the data closely follows this trend.

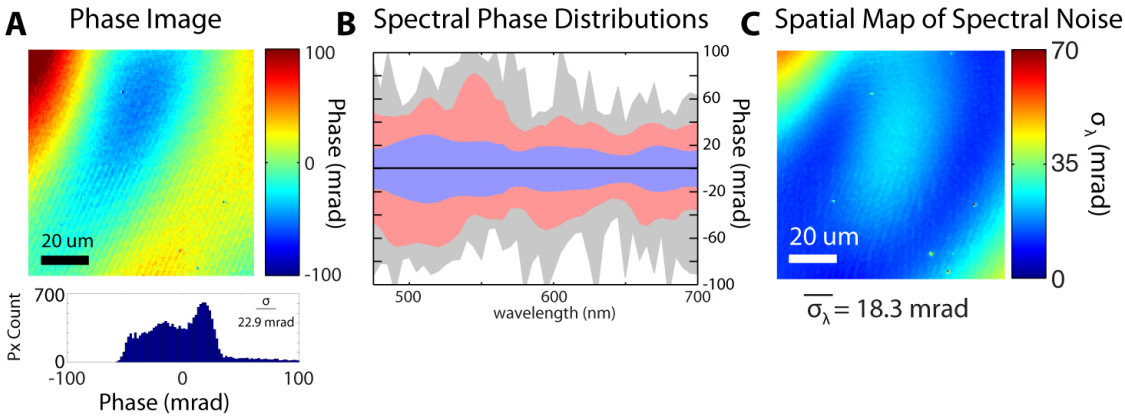

Figure 3.15: Characterization of spectral phase noise after camera has been on for ~30 minutes. The background phase and a 1st order polynomial have been removed. (A) Phase image at λ_0 = 550 nm. (B) Spectral plot of the spatial phase distributions at each wavelength. Blue area indicates $\pm\sigma_{xy}$, red area shows the 99th percentile range of all pixels, and grey shows full range of all pixel values. (C) Spatial map of the spectral noise, σ_λ.

As mentioned at the beginning of section 3.2.5, the interferometric system is sensitive to mechanical vibrations, temperature fluctuations, and other sources of

temporal drift. The data used for the spectral noise analysis presented in Figure 3.13 was taken within 5 minutes of turning on the supercontinuum laser and the camera. When the camera has been running for a significant period of time (more than ~30 minutes), the QPS instrument begins to exhibit phase instability. Figure 3.15 shows that low-frequency oscillations in the spatial phase appear when the camera has been running for more than ~30 minutes, increasing the average spatial noise across the spectral range to $\overline{\sigma_{xy}} = 19.7 mrad$ and the average spectral noise across the field of view to $\overline{\sigma_{\lambda}} = 18.3 mrad$.

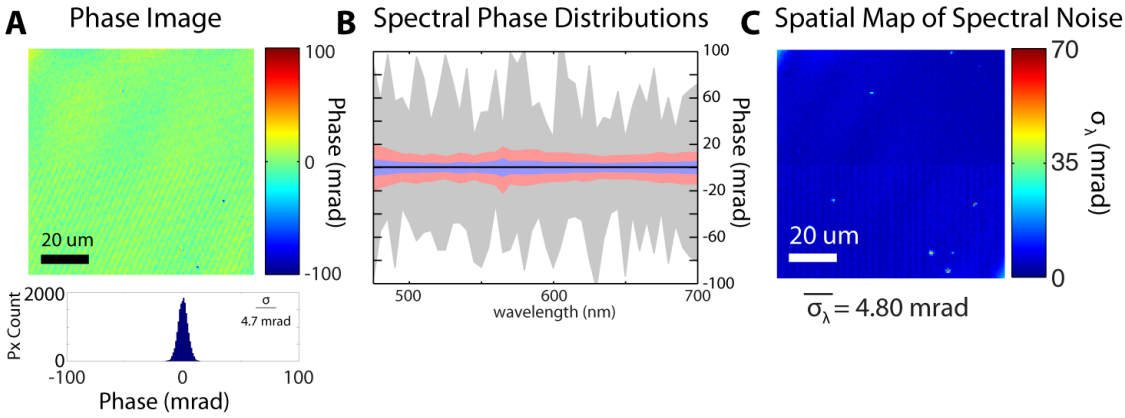

Figure 3.16: Characterization of spectral phase noise after camera has been on for ~30 minutes. The background phase and a 5th order polynomial have been removed. (A) Phase image at λ_0 = 550 nm. (B) Spectral plot of the spatial phase distributions at each wavelength. Blue area indicates $\pm\sigma_{xy}$, red area shows the 99th percentile range of all pixels, and grey shows full range of all pixel values. (C) Spatial map of the spectral noise, σ_{λ}.

The smooth variations in phase seen in Figure 3.15 can be fit to a low-order two-dimensional polynomial and removed. Subtracting a polynomial surface from the data taken when the camera is first turned has little effect on the spatial and spectral noise

metrics. However, removing a 5th order polynomial from each spectral phase image does significantly reduce the noise back to the range found when the camera is initially turned on, resulting in $\overline{\sigma_{xy}} = 4.93 mrad$ and $\overline{\sigma_{\lambda}} = 4.80 mrad$ (Figure 3.16). While the noise appears to be reduced, the phase oscillations dampen the impact of spatial averaging to reduce spectral noise (Figure 3.17). Unlike the trend that Figure 3.14 shows, the relative noise reduction achieved by averaging successively larger regions does not follow a 1/sqrt(n) trend, suggesting that the spectral noise is still spatially-correlated even after removing a 5th order polynomial from each wavelength's phase image.

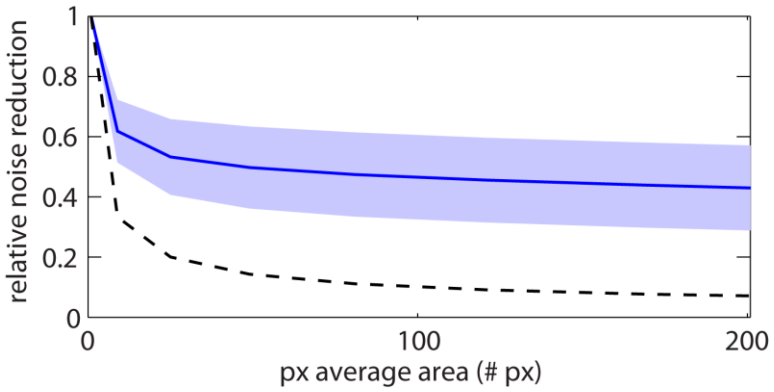

Figure 3.17: Spectral noise reduction achieved by averaging within spatial regions of increasing areas from the FOV analyzed in Figure 3.16. Black dotted line indicates 1/sqrt(n) ideal noise reduction. Blue solid line and light blue region show the average and standard deviation in relative noise reduction when comparing multiple regions across the FOV.

3.3 Summary

In this chapter, the development of off-axis quantitative phase microscopy and spectroscopy instruments was presented. The off-axis QPM instrument captures

interferograms that are spatially-filtered to recover quantitative phase images of microscopic objects. These phase images are then conditioned by subtraction of a low-order polynomial surface and a reference phase image to reduce structured phase aberrations arising from the optical system. Methods of removing 2π ambiguities by phase unwrapping were also reviewed, and one method of simultaneously capturing interferograms for two-wavelength phase unwrapping on a color camera was detailed.

The extension of QPM capture spectroscopic holographic data was achieved by modifying the system design to use a broadband illumination source with an appropriate tunable spectral filter and by syncing the camera's acquisition to the source's wavelength step. The resulting QPS instrument can either be set to a single wavelength to capture high-speed dynamics at >kHz frame rates or utilized to capture interferograms across the visible wavelength range (475 – 700nm) in ~5s for spectral characterization of samples. The effects of the low-coherence illumination source were discussed and mathematically modeled, and the method for acquiring hyperspectral phase image stacks was outlined. An analysis of the system's spatial, temporal, and spectral phase noise verified sub-nanometer single image sensitivity after background phase image subtraction and polynomial subtraction. Averaging phase information from multiple interferograms significantly decreased both the spatial and temporal noise characteristics, primarily because more photons are gathered and averaged to increase the optical signal-to-noise ratio (OSNR) when calculating phase images. This noise

analysis inidicates that the QPS microscope can perform sub-milliradian measurements both spatially and temporally with effective integration times on the order of tens of milliseconds. Similar noise characteristics can be achieved at higher effective frame rates using the same system with a proportionally larger amount of optical power.

4 Image Processing Methods

Chapter 4 presents several novel methods of analyzing the quantitative phase information produced by the QPM and QPS systems. Section 4.1 describes the method of holographically-refocusing individual phase images and reviews several metrics that are used to automatically find the "best focus" of an image. Section 4.2 presents optical volume (OV) as a novel metric for evaluating microscopic objects whose height profiles cannot be separated from their RIs, and experimentally validates the use of automatic digital refocusing to accurately measure OV using microspheres with known sizes as well as individual RBCs whose RI and thicknesses are not well-characterized. After demonstrating noise-reduction in phase images by spectrally-averaging multiple measurements obtained by QPS (section 4.3), the methods of extracting spectral dispersion and molecular content characterization are discussed in section 4.4. A glass microchannel system containing serially-diluted rhodamine 6G (R6G) samples is measured by QPS, and a subsequent concentration estimation from the holographic phase and amplitude data compares the sensitivity of each method for quantifying spectral features.

4.1 Digital Refocusing

Holographic images can be refocused digitally after recording. Refocusing by Fresnel propagation is achieved by convolving the complex in a given plane by the free

space impulse response. It is commonly implemented using Fourier transform methods by multiplying the complex wave's angular spectrum by the transfer function of free-space (Fresnel Kernel) and then inverse Fourier transforming back:

$$E(x,y,z) = FT^{-1}\left\{ FT\left\{E(x,y,0)\right\} \cdot e^{i2\pi\frac{z}{\lambda}\sqrt{1-(\lambda f_x)^2-(\lambda f_y)^2}} \right\} \qquad (4.1)$$

Determining a suitable metric for assessing the plane of best-focus is not straightforward, and methods have been attempted by several groups. Algorithms are typically validated using simulated defocused data, however when assessing real holograms where the initial defocus distance is unknown, there is no quantitative validation that a "best focus" plane corresponds to the maximization/minimization of the focus metric apart from the visual quality of the reconstructed images.

Liebling and Unser developed an algorithm for refocusing holograms using a Fresnel-wavelet ("Fresnelet") propagation method.[77] This method projects the propagated holograms onto a Fresnelet basis, and then calculates sparsity by measuring how much energy (intensity) resides in some predetermined fraction of the Fresnelet coefficients. When the energy contained within this fraction of coefficients is maximized, the hologram is considered to be optimally focused. The authors show that this focus metric produces an intensity profile that is sharper in depth, and therefore more sensitive, than examining the Laplacian or squared-intensity in the spatial-domain

representation of the object. As an example, one simulated hologram is propagated over a range of ~200mm and the best-focus plane is accurately measured at 100mm.

Dubois, et al., proposed an amplitude-summation metric for determining the best-focus-plane of holographic images.[78] Although energy of an optical field is conserved during free-space propagation ($E=\sum|A(x,y)|^2=Const.$), the amplitude of the complex wave is shown to either be maximized for an amplitude object or else minimized for a phase-only object at the plane of best-focus. The authors calculate local minima over 50- and 100-μm ranges for amplitude objects, and a local maximum over a 250-μm range for a neuron (phase-object), although the only validation of finding the "best focus" is a qualitative display or refocused images. Thus it is not clear how accurately the objects are in fact refocused and no bound is placed on the uncertainty/error of the method.

Langehanenberg compares several amplitude-based metrics for holographic refocusing.[79] Specifically, a weighted spatial frequency summation that indicates sharpness of high-frequency information (SPEC), edge detection via summed gradient (GRA) or Laplacian (LAP), amplitude variance (VAR) quantities are calculated at each focal depth for the field of view over a ±15cm image plane range. After accounting for magnification, the algorithms all appear to find a best focus plane in the range of a few micron differences, although it is not clear how accurately the sample is refocused. All of the refocusing metrics presented appear to precisely and repeatably find a plane of

best focus, although VAR and LAP metrics do not appear to be unimodal in their minimum values and therefore may be limited in range or lack robustness across varied sample geometries.

More recently, Xu, et al., proposed a phase-based metric for determining the best focus of holographic phase images.[80] This metric is calculated by (1) evaluating the spatial differences between two phase images propagated to two different planes separated by some δz; (2) digitally removing noise and enhancing feature contrast; (3) calculating the metric, $\eta\{d\}$, based on the variance between two of the differential phase images. $\eta\{d\}$ can be viewed as an indicator of how much refocused images at adjacent depths differ from one another. On either side of the best-focus plane, the indicator has a non-negative value (positive or negative depending on which side of focus the metric is computed on) and crosses zero at the plane of best focus. The images shown in this study are of macroscopic objects – pennies & keys containing mm-scale sharp features such as writing – that are refocused over a range of 1200mm. The refocusing algorithm's accuracy is again based on visual image quality assessment rather than a quantitative measurement of a known feature size.

In the work presented in this dissertation, an amplitude-based metric is used to determine the plane of best-focus. Similar to DuBois and Langehanenberg, individual cells, used as imaging targets, are assumed to only weakly absorb light. Consistent with these approaches, the metric used here also assumes that phase-based metrics are not

reliable due to phase wrapping. First, the measured complex wave is propagated over a range of ±z from the initial measurement plane. Then, the variance of the amplitude of the propagated wave is computed either across the entire field of view or within a region surrounding a single cell of interest. Plotting the variance over the defocus distance reveals a minimum variance at the plane of best-focus. While previous research has demonstrated optimal focus by displaying images that appear to be sharpest or cleanest, quantitative phase information is primarily interesting due to its quantitative nature: the ideal focus will produce quantitative images that allow accurate computation and comparison of OPL-based metrics.

4.2 Optical Volume

The physical volume of an object can be calculated from a two-dimensional (*x,y*) thickness map as:

$$V = \iint_{x,y} h(x,y)dxdy = SA \cdot \bar{h}_{x,y} \tag{4.2}$$

Here, *h(x,y)* is the thickness (height) map of the object, *SA* is the projected surface area, and $\bar{h}_{x,y}$ is the average height across the object.

Determining the volume of microscopic objects from optical images is not as straightforward, however quantitative phase microscopy measurements can be mathematically related to volume because the optical phase delays, $\Delta\varphi(x,y)$, are proportional to the height of the object:

$$h(x,y) = \frac{\Delta\varphi(x,y)\cdot\lambda}{2\pi\cdot\Delta n(x,y)} \tag{4.3}$$

where $\Delta n(x,y)$ represents the difference in refractive index between the sample material and its surrounding medium. Note that the height map of an object can only be calculated if the refractive indices of the object and surrounding material are known at each spatial location. Equation (4.3) can be reorganized to relate the measured phase to relative optical path length changes, $\Delta OPL(x,y)$:

$$\Delta OPL(x,y) = \frac{\lambda}{2\pi}\cdot\Delta\varphi(x,y) = \Delta n(x,y)\cdot h(x,y) \tag{4.4}$$

Optical path length is a useful quantity to describe an object whose refractive index is not specifically known, and is directly proportional to the sample's physical properties. Unlike phase, typically ΔOPL is not a linear function of wavelength. ΔOPL, can be integrated to yield a new metric, the Optical Volume (OV):

$$OV = \iint_{x,y} \Delta OPL(x,y)dxdy = \iint_{x,y} \Delta n(x,y)\cdot h(x,y)dxdy \tag{4.5}$$

If the refractive index of the object is assumed to be homogeneous, i.e., $\Delta n(x,y) \approx \overline{\Delta n}_{(x,y)}$, then the optical volume is linearly related to the true volume of the object:

$$OV = \overline{\Delta n}\cdot\iint_{x,y} h(x,y)dxdy = \overline{\Delta n}\cdot V \tag{4.6}$$

When the refractive index of the object or surrounding media is dynamically changing or is not well-characterized, the optical volume provides an effective metric for characterizing the sample's dynamic changes as will be shown. Note that the refractive index, measured phase, optical path length, and optical volume are all implicitly functions of wavelength; this dependence has been omitted in the above framework for the sake of convenience but incorporating spectroscopic information may further provide a means for characterizing microscopic objects using this framework.

4.2.1 Use of Optical Volume as a Focus Criterion

The relationship between object volume, refractive index, and optical volume as defined by equation (4.6) is valid when homogeneous objects are measured in homogeneous media, $\Delta n(x,y) \approx \overline{\Delta n}_{(x,y)}$. When inhomogeneous objects are measured, this relationship may still be valid if the object's refractive index can be written as a linear combination of its constitutive components:

$$n_c = n_0 + \sum_i \alpha_i C_i \tag{4.7}$$

Barer, *et al.*, and Davies, *et al.*, demonstrated that RI increments, α_i, could be used to directly relate interferometric phase measurements to the dry mass of living cells, and further measured RI increments for a range of proteins, salts, and other biologically-relevant solutes.[81–83] Furthermore, the RI of bovine serum albumin was measured to be linear as a function of mass/volume concentration up to concentrations of 55%.[84]

Consistent with these findings, a discrete microscopic sample's average RI may to first approximation be considered to remain constant with an additionally varying term that is linearly proportional to the solute's mass with increasing concentration of the solute.

It is worth noting that several refractive index mixture rules have been devised to characterize inhomogeneous solutions[85]. Born and Wolf's explanation[86] of the Lorentz-Lorenz equation suggests that the RI of mixtures is accurately described as mole-fraction linear combinations of molar refractivity values of materials. Equation (4.7) is not equivalent to a mole-fraction or volume-fraction summation, but is conceptually similar and adequately approximates the RI of aqueous solutions of biomaterials at sufficiently low concentrations.

In the following sections, the Optical Volume quantity will be shown to be useful as a criterion for best focus determination, even in the case where RI changes are induced by physical volume changes. In the context of the off-axis QPM and QPS systems presented in this dissertation, the imaged samples are typically thin and semi-transparent, avoiding complications caused by diffraction and multiply-scattered light arising from the three-dimensional nature of thicker samples. The use of OV defined in Equations (4.5) and (4.6) as a focus criterion is therefore confined to semi-transparent objects that act as a single-plane complex transmittance mask.

4.2.2 Optical Volume as a Performance Metric for Digital Refocusing

Section 4.1 describes methods of digital refocusing and criteria by which to automatically assess a plane of best focus. While these criteria produce refocused phase and amplitude images that appear visually well-focused, no independent metric is presented to validate whether a plane of best-focus has been achieved. Generally, when the refractive indices of an object and its surrounding medium are well-characterized, the measured volume may serve as such a metric. However, even when exact refractive indices are not known, optical volume measurements are shown here to still serve as a robust characterization of a sample, providing an effective metric by which to gauge the best focal plane of the system.

To demonstrate the effectiveness of using volume and OV as refocusing performance metrics, polystyrene NIST-certified microspheres with known refractive indices and sizes (Duke Scientific, $n_D = 1.5916$) were imaged by quantitative phase microscopy ($\lambda_0 = 589nm, \delta\lambda = 1.12nm$). Four nominal sizes were used: d = 4.000μm ± 1% coefficient of variation (C.V), d = 6.007 μm ± 1% C.V., d = 6.982 μm ± 1% C.V., and d = 7.979 μm ± 1.1% C.V.. Each microsphere sample was washed with DI water twice and placed in vacuum over night to fully dehydrate the spheres. The spheres were then diluted in immersion oil (Cargille, $n_D = 1.5150$) and loaded into rectangular capillary tubes (Vitro, d = 0.3mm) and allowed to settle to the bottom surface overnight. Each of the four samples were then imaged via QPM after hand-focusing the sample; each

interferogram showed ~2-5 microspheres that were spatially separated, and images of 30 microspheres were captured for each sample.

Interferograms were processed according to the methods presented in section 3.1: phase and amplitude images were recovered, referenced to background holograms captured of oil-only fields of view, and then fit to 5^{th}-order polynomials to remove any background phase and amplitude structure. Each FOV's phase and amplitude were then Fresnel transformed using equation (4.1) to digitally propagate the wavefront from -25 μm to +25 μm in 0.5 μm steps (100 total positions). The amplitude of the propagated FOV was used to calculate the amplitude variance metric discussed in section 4.1. The amplitude variance was then interpolated to steps of $\Delta z = 10$ nm, and the depth associated with the minimum variance was taken to be the best plane of focus. The Fresnel transform was then used to propagate the original complex wave data to this plane, and the phase image was again flattened using a 5^{th}-order polynomial fit to background points.

The obtained complex wave was then segmented. Microspheres were selected using a semi-automatic segmentation algorithm: this algorithm identifies and isolates phase objects with values greater than a specific threshold and within a specific size range. These segmentation parameters are adjusted by sample in order to capture all objects of interest. In the experiments presented here, the object's phase threshold is set

to 0.2 radians, and the area captured by the threshold operation is expanded slightly to capture all of the surface area of the object.

Figure 4.1 illustrates the refocusing procedure used on an image of a single 8-μm diameter microsphere. This microsphere image has been focused over an expanded z-range of ±100 μm to illustrate the effects of defocus. As this microsphere image was hand-focused, the amplitude cross-section appears to be well-focused with minimal wavefront variation near 0 μm. The corresponding phase image also appears to be approximately spherical while the defocused phase images quickly lose fidelity. Examining the amplitude variance of the FOV, the minimum variance occurs at z = -2.46 μm. The variance also monotonically increases on either side of the minimum-variance location up to a range of ~ ±50 μm. When hand-focusing an object prior to image acquisition, it is fairly easy to place the object within ~ ±20 μm of the true focus; once the microsphere image is manually defocused to ±100 μm, the image quality is extremely poor, and diffraction rings indicate an incorrect focal plane. Because the errors of hand focusing are in-practice very small, this automated refocusing method has the potential to be performed much more efficiently than is presented here by restricting the range of refocus without risk of identifying local minima that do not correspond to a best-focus plane.

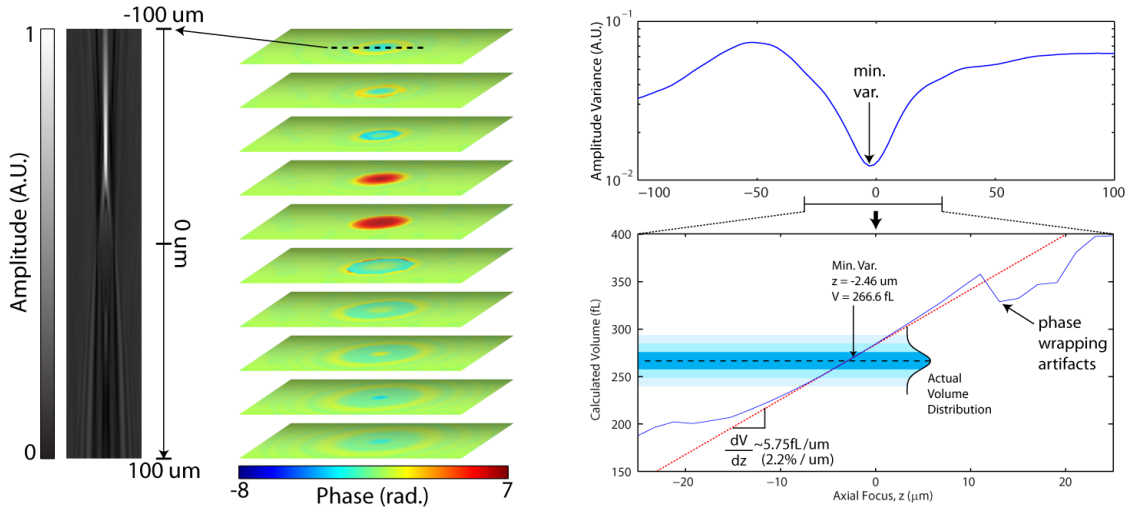

Figure 4.1: Digital Refocusing of a Single Microsphere. (A) xz-slice of amplitude focus; (B) representative phase images of microsphere at multiple propagation distances; (C) amplitude variance as a function of propagation distance, minimum variance location indicated with arrow; (D) measured microsphere volume vs. focal distance, red line indicates change in volume measurement with defocus distance, dashed lines and blue regions indicate the actual microsphere population distribution, ±σ, 2σ, 3σ.

Once the best focus is chosen according to the above variance criteria, it is next helpful to examine the effects of defocus on volume calculation. Accordingly, the phase image of the 8-μm microsphere in Figure 4.1 is analyzed at each defocus distance over the axial range. After phase image referencing and polynomial subtraction, the optical volume over the displayed region is calculated according to equation (4.5). The true volume of the microsphere is then calculated using the RIs of both the index-matching oil and polystyrene ($\Delta n = 0.0766$) which are both well characterized for this example. Figure 4.1 shows that the measured volume changes significantly with defocus position: for every micron of defocus, the measured volume changes by 2.2% (slope of the tangent

line at the minimum-variance axial position). Once the microsphere image is refocused further than ~ ±10 μm from the optical focus, phase wrapping artifacts begin to further degrade the accuracy of the volumetric measurement. The NIST-certified microsphere population has a diameter distribution of 1% C.V., which corresponds to a volume distribution of 3% C.V. Each shaded blue region in Figure 4.1 represents an increasing variance in multiples of ± σ with lightening shade. The hand-focused microsphere image yields a calculated volume of 281.7 fL, which is 5.9% (~2σ) higher than the specified population average volume of 266.0 fL; once digitally-refocused, the microsphere's volume is measured to be 266.6 fL, within 0.22% of the specified population average volume. This analysis illustrates that even a slight defocus of 2.46 μm, an amount well within the variation of manual focus, can introduce significant error in volume measurement.

Comparison of the measured diameters and volumes of the four microsphere populations (n=30 in each) against the reference diameters and volumes demonstrates the accuracy of volumetric measurements by QPM (Figure 4.2) when using the method of digital refocusing with the new Optical Volume variance minization. The equivalent diameters are computed from the measured volumes as $d = 2 \cdot (\frac{3}{4\pi} V)^{1/3}$. The dashed lines indicate perfect agreement with the nominal diameter and volume, while the blue error bars indicate the range of parameters for the population of all microspheres measured. The root-mean-square (RMS) errors across all diameter measurements is

1.7%, and 5.24% for the volume measurements; the obtained errors showed no trend with object size. Closer examination of the 7-μm microsphere population reveals that the hand-focused population mean diameter is 3.6% higher than the true population mean with a coefficient of variation of σ = 1.06% (specified CV = 1%). Digital refocusing reduces the population mean diameter error to +0.63% and reduces the CV (σ = 0.91%) to less than the specified CV.

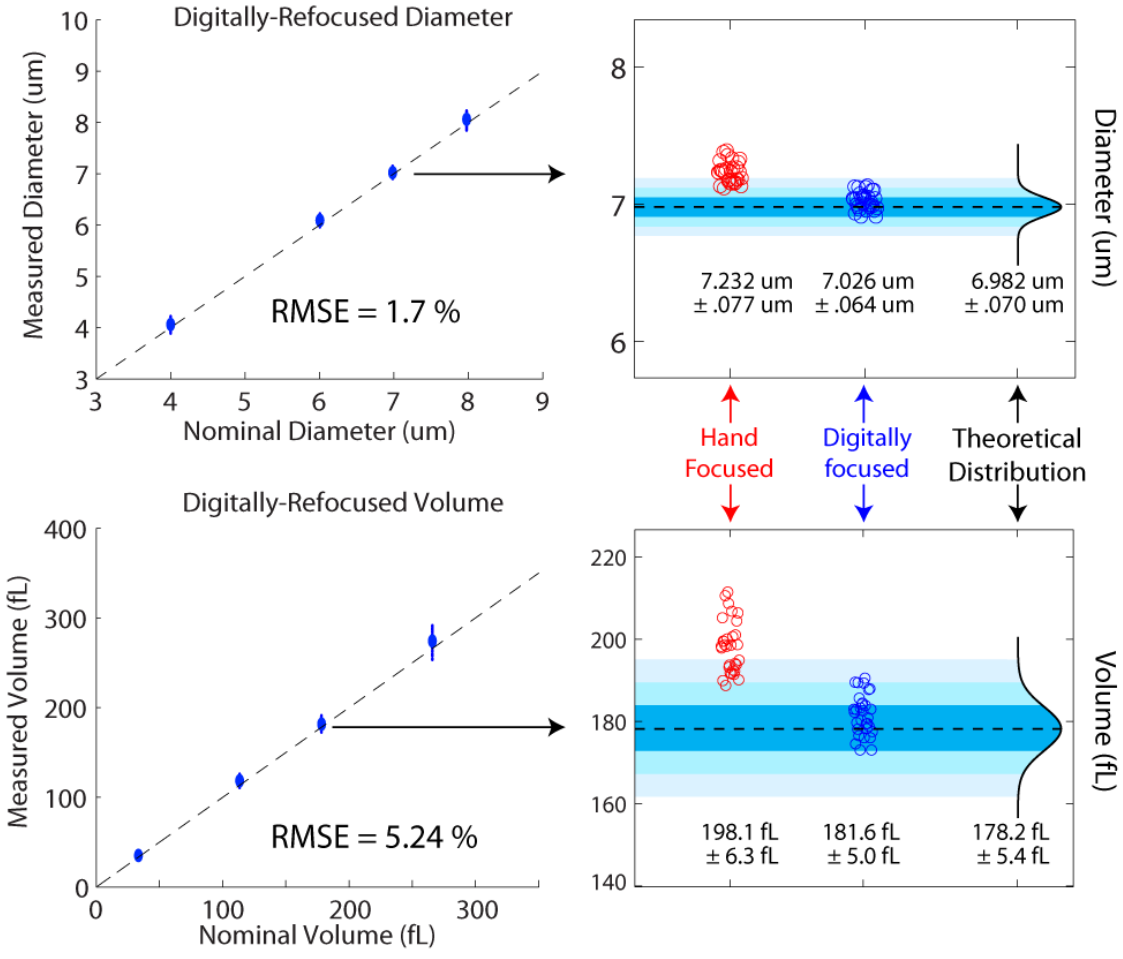

Figure 4.2: Diameter and volume prediction plots for four microsphere populations. Left: blue dots and bars indicate population mean and standard

deviation. Right: Data for 7-μm diameter microspheres. Red circles indicate measurements of the hand-focused images, while blue circles indicate the digitally-refocused measurements. Dashed lines and blue regions indicate the actual microsphere population distribution, ±σ, 2σ, 3σ. Metrics are reported as means ± standard deviations.

The precision of diameter and volumet measurements presented here may be characterized using the average CV across the four populations, which are 1.15% and 3.45% respectively. These represent an upper bound on the accuracy of the digital refocusing technique. The precision of QPM diameter and volume measurements after digital refocusing by these methods may in fact be lower, however the variation of microsphere sizes within each population, and available characterization of only the population variations, limits our ability to quantify the true bounds on precision.

4.2.3 Digitally-refocused Optical Volume of a Red Blood Cell

In the following experiments, we demonstrate the effect of defocus on optical volume measurement by imaging a single red blood cell at multiple focal planes over a range of ~200μm (Figure 4.3). The top row displays the amplitude images recovered from the holograms; this is representative of what a microscope user relies on as a visual guide while attempting to focus the sample prior to acquisition. The bottom row shows the phase images corresponding to each amplitude image above. The center image was judged to be the "best focus plane" by eye when acquiring these images. Each of the manually defocused holograms is refocused over a range of ±150 μm. Each cell's amplitude variance (bottom left) shows a distinct global minimum, indicating the

distance of original defocus, or the error produced by manual focusing. After refocusing each hologram, the resulting phase images are qualitatively similar. The slight variations in shape are due to the RBCs being dynamic objects: slight membrane fluctuations, internal distribution changes of hemoglobin and other biomolecules, and potential fluid transport across the membrane account for the differences in the morphology of the refocused RBCs across the images in A-G.

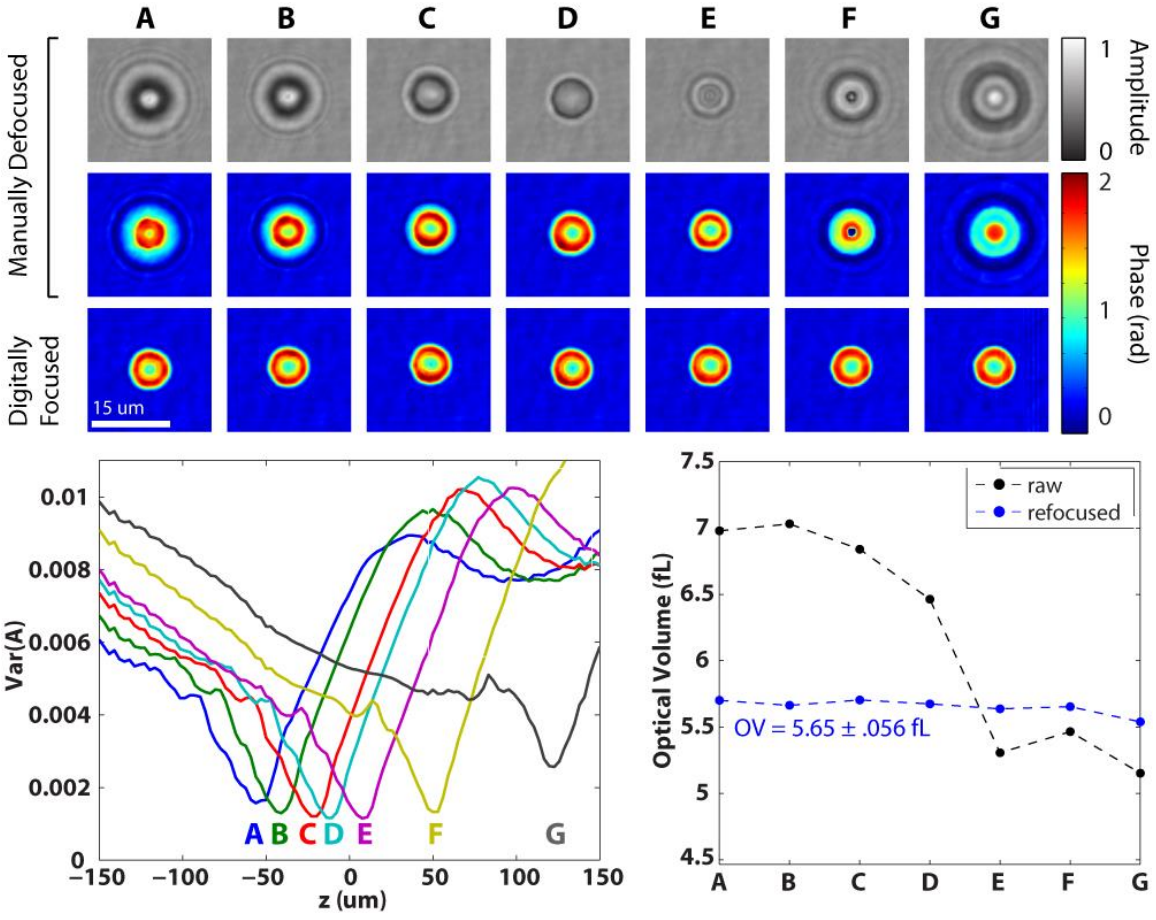

Figure 4.3: Digital refocusing of a single red blood cell and corresponding optical volume measurements. Top: Amplitude and phase of manually-defocused holograms of the same cell, followed by digitally-refocused phase images. Bottom-Left: Amplitude variance metric of holograms A-G. Bottom-Right: Computed OV of

RBC from manually-focused phase images (black) and digitally-refocused phase images (blue). OV reported as mean ± standard deviation.

Because the contents and morphology of RBCs vary across a population, the RI and three-dimensional structure are not known *a priori*. Thus, optical volume can be an effective metric for classifying RBCs since it does not require assumptions about the RI or thickness profile. Prior to refocusing, the measured OV of the RBC shows large variation, ranging from 5.15-7.03 fL (σ = 13.55%). After refocusing, the measured OVs range from 5.54-5.70 fL (σ = 0.99%), indicating high precision of measurements. There is a slight negative trend in refocused OV from A to G, suggesting that the refocus distance may affect the calculated volume. However, this effect is minor in this example. These results indicate that automated digital refocusing using a minimum amplitude variance metric allows consistent measurements of the OV of individual RBCs over time.

4.3 Spectral Averaging of Phase Measurements

QPS captures holograms with narrow-band illumination over a wide spectral range. Narrow-band illumination permits measurements at precise wavelengths and also results in a wide field of view with high SNR in the off-axis QPS system presented in section 3.2. However, coherent artifacts arising from spurious reflections and speckle have a high visibility. A wider illumination bandwidth may be used to reduce coherent noise, but drastically limits the field of view in this experimental setup (Figure 3.6). Averaging phase information captured at multiple narrow-band center wavelengths significantly reduces coherent noise while retaining the field of view of each narrow-

band phase image and increasing the overall SNR of the resulting images. If the phase delay through a microscopic sample contains no chromatic dispersion (i.e., phase is linear in *k*) over the wavelength range of averaging, then the averaged phase may be written as:

$$\overline{\Delta\varphi}(k_0^{'},\vec{r}) = \frac{\sum_{i=1}^{N}\left\{\Delta\varphi(k_0^i,\vec{r})\right\}}{N} \tag{4.8}$$

where $k_0^{'} = mean\left(k_0^1, k_0^2, k_0^3, ..., k_0^N\right)$. When samples exhibit phase delays that are nonlinear in *k*, $\overline{\Delta\varphi}(k_0^{'},\vec{r})$ may be used as a reasonable first-order approximation of $\Delta\varphi(k_0^{'},\vec{r})$; however, dispersion and nonlinear features corresponding to absorptive features via the Kramers-Kronig relations[16] may be obscured when averaging in this fashion.

The reduction of coherent artifacts by averaging QPS measurements at multiple center wavelengths is demonstrated by imaging a custom-molded PDMS phase object (polydimethylsiloxane, Sylgard 184, Dow Corning). PDMS is poured over a glass photomask with features etched in a 90-nm thick layer of chrome ("BIOS LAB") and allowed to set at room temperature overnight. The thin PDMS layer is then carefully peeled off of the photomask and placed feature-side-up on a microscope slide. The PDMS-air interface RI mismatch (Δn≈0.41) creates a pure phase object for evaluation. Figure 4.4 (A) & (D) show a single phase image acquired at $\lambda_0 = 603nm$ with a bandwidth of $\delta\lambda = 5.4nm$ at different spatial scales. The finite illumination bandwidth

limits the field of view, however coherent artifacts are still visible. Figure 4.4 (B) & (E) present the spectral average of 220 phase images taken in 1-nm steps across the full spectral range of the QPS instrument, 500-720nm, producing a phase image with an effective center wavelength of $\lambda_0^{'} = 603nm$ ($\lambda_0^{'} = 2\pi / k_0^{'}$, see above). The resulting phase map has significantly reduced coherent artifacts and extends the imaging field of view achieved in each of the individual phase images. The remaining bullseye phase ripples, likely due to out-of-plane dust contaminants, are greatly reduced and the bottom half of the letter 'B' is now visible as a result of the increased SNR. The spatial standard deviation of a featureless region indicated by the white stars decreases from σ = 27.7 mrad to σ = 8.6 mrad after spectral averaging, demonstrating a ~3.2× reduction in coherent noise.

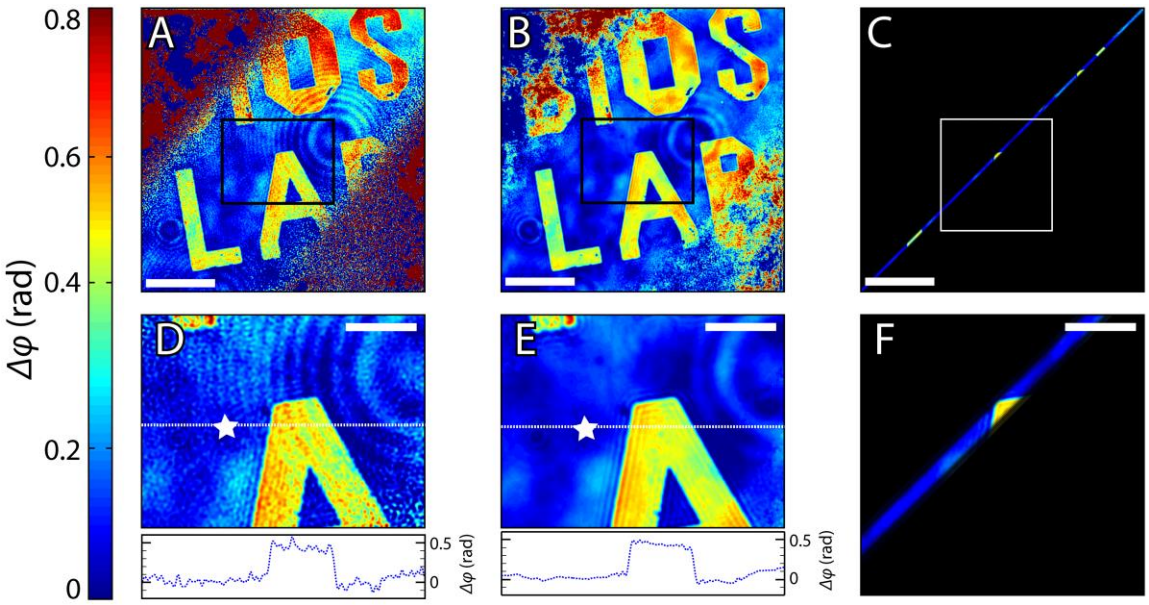

Figure 4.4: Phase images of a transparent PDMS phase object, demonstrating a reduction of coherent noise by spectral averaging. Letters have a nominal 90nm

thickness. (A,B) Full field of view (~200x200μm) with reduced SNR at the edges; 50μm scale bars. (D,E) zoomed in view with insets corresponding to plots at the dotted lines; 20μm scale bars. (A,D) imaged with λ_0=603nm, δλ=5.4nm; (B,E) computed by averaging 220 phase maps across 500-720nm, λ_0^'=603nm. (C,F) Simulation of a phase image acquired with δλ=220nm; note the area over which high-SNR phase information is significantly reduced. Taken from Rinehart, *et al.*[17]

Alternatively, coherent artifacts may be reduced by illuminating the sample with a wider bandwidth source with lower temporal coherence. For comparison, Figure 4.4 (C) & (F) simulate the field of view that would result from such illumination: the calculated complex envelope of the acquired interference fringes is used to mask the spectrally-averaged phase images seen in Figure 4.4 (B) & (E). The resulting high-SNR field of view is limited to a fraction of that achieved by spectrally averaging phase images with a small- but finite-bandwidth illumination. In addition to reducing coherent artifacts and maintaining a wide field of view, acquisition of multiple phase images over the visible range with narrow bandwidth preserves spectral features of microscopic objects for subsequent analysis.

4.4 Molecular Concentration Determination

The optical absorption of a sample is mathematically related to the refractive index of the sample through the Kramers-Kronig relations. Using these equations, one spectrum (absorption of refractive index) may be calculated from the complete spectrum of the other, making each accessible when only the other is measured. Furthermore, truncated absorption spectra surrounding local features may be used to approximate the differential contributions to the refractive index function and vice versa. When the real

part of the refractive index, $n(\omega)$, of a substance is known at a specific wavelength, the refractive index spectrum can be calculated from attenuation data as:

$$n(\omega) = n(\omega_0) + \frac{2}{\pi}(\omega^2 - \omega_0^2) P \int_0^\infty \frac{\omega' \kappa(\omega')}{(\omega^2 - \omega'^2)(\omega_0^2 - \omega'^2)} d\omega' \qquad (4.9)$$

where the complex refractive index is defined as $\tilde{n}(\omega) = n(\omega) + i\kappa(\omega)$, and $\kappa(\omega)$ is related to the attenuation coefficient of a material as $\kappa(\omega) = \mu_a'(\omega) \cdot \frac{c}{2\omega}$. Likewise, the Kramers-Kronig relations may be extended to relate the molar extinction coefficient and refractive index increment (material properties), as well as absorbance spectra to OPL spectra (concentration- and pathlength-dependent properties).

In the experiments presented below, we demonstrate the ability of the QPS system to effectively measure molecular concentrations of a liquid in a microchannel. For each of three cases 1) the empty microchannel, 2) the microchannel containing water only, and 3) the microchannel containing concentration samples, the phase and amplitude data are collected and processed as follows. Each spectral phase dataset is averaged over multiple acquisitions (32 holograms captured across a range of wavelengths) and referenced against both a background phase image and a first-order polynomial fit to non-sample regions of the image to produce wrapped phase images. Corresponding amplitude images are similarly averaged and then divided by the reference amplitude to produce relative amplitude transmittance images at each wavelength.

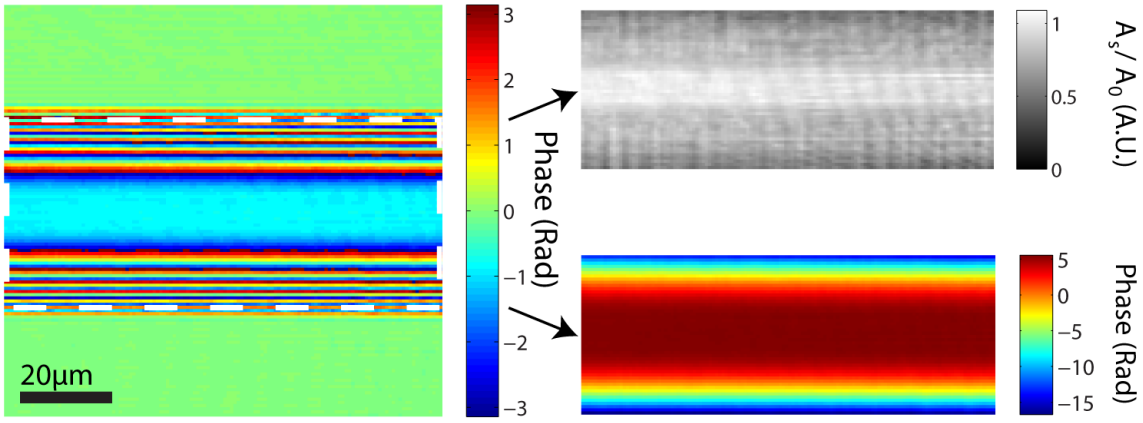

Figure 4.5: Glass microchannel for QPS concentration measurements (λ_0 = 590 nm). (A) wrapped phase image of the empty channel, (B) relative amplitude image of the white dotted ROI in (A), (C) unwrapped phase image of the white dotted ROI in (A).

4.4.1 Air-Glass Holographic Spectroscopy: Empty Microchannel

To validate the ability of QPS to measure aqueous molecular concentrations, the OPL spectra of multiple media were measured in a rigid borosilicate glass microchannel (Micronit, FC_X3550CH.3) over a wavelength range of 475-700nm in 5nm steps. The microchannel has a nominal 20 ± 3 μm maximum height[87], while the refractive indices of the glass is specified at two wavelengths as n_D = 1.5230 and n_e = 1.5255.[88] The microchannel's height is first calculated to be 20.140 μm from measurements of the phase spectrum through the thickest section of the channel using equation (3.6) and the nominal reference RIs (measurements at λ_0 = 590nm and λ_0 = 545nm approximately correspond to n_D and n_e, respectively). As Figure 4.5 shows, the RI mismatch between the glass and air creates an optical pathlength with significant wrapping artifacts that are not easily removed with two-dimensional phase unwrapping algorithms. However,

the middle section of the microchannel has a sufficiently smooth phase profile (white dashed ROI) to be mostly unwrapped when isolated from the background: phase unwrapping fails in this case only at the edges of the microchannel where the spatial phase gradient exceeds the sampling resolution.

Using the measured height, the attenuation coefficient spectrum of the glass is calculated from the holographic amplitude images, and the refractive index spectrum is calculated from the quantitative phase measurements (Figure 4.6). The microchannel's glass is specified to have a transmittance of 91.7% across 380-780nm when measured through a 150μm thick coverslip, which corresponds to an absorption coefficient of 5.7765 cm^{-1} (black dashed line in Figure 4.6 (B)). The single-point and area-averaged (671 spatial points over 360 μm^2) attenuation coefficient measurements contain spectral noises of $\sigma_{pt} = 54.8\ cm^{-1}$ and $\sigma_{avg} = 35.4\ cm^{-1}$, respectively. The calculated refractive index spectrum of this glass shows good agreement with the given literature values (green stars in Figure 4.6 (C)), with an average absolute error of 2.57×10^{-4} at these points. A curve with the form of the Sellmeier equation is fit to the refractive index spectrum calculated from the area shown in Figure 4.5 (C) for use as a noise-free RI spectrum of the glass in future experiments:

$$n_{glass}{}^2(\lambda) = 1 + \frac{B_1\lambda^2}{\lambda^2 - C_1} + \frac{B_2\lambda^2}{\lambda^2 - C_2} + \frac{B_3\lambda^2}{\lambda^2 - C_3} \tag{4.10}$$

After subtracting the Sellmeier fit, the refractive index residuals are $\sigma_{pt} = 2.17 \times 10^{-4}$ and $\sigma_{avg} = 1.31 \times 10^{-4}$, which bound the spectral RI measurement precision when measuring homogeneous fluid samples within the 20-μm microchannel.

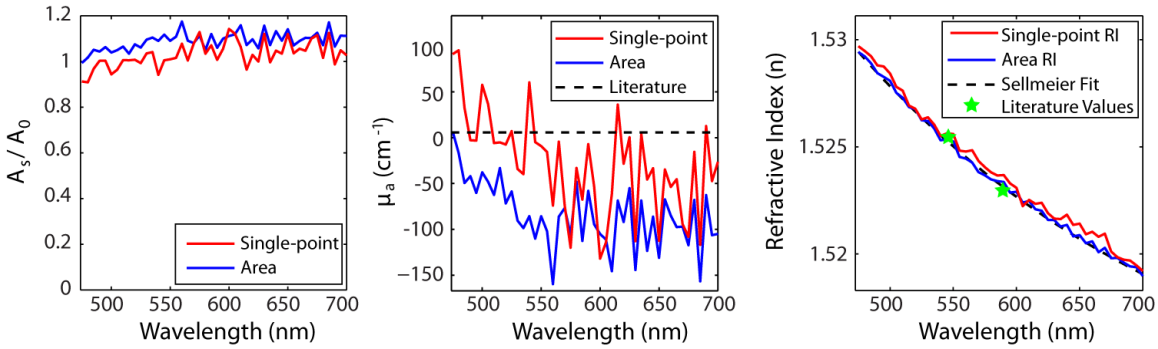

Figure 4.6: Glass microchannel characterization: (A) holographic relative amplitude spectrum, (B) calculated attenuation coefficient, (C) Calculated refractive index. Red lines correspond to point-measurements, blue lines indicate area-averaged measurements over 671 spatial points, or 360 μm^2. Black dashed line in (B) indicates literature attenuation coefficient. Black dashed line in (C) shows Sellmeier fit to the data. Green stars in (C) indicate published RI of the microchannel's glass.

While the known thickness of the channel allows calculation of the refractive index, it is not straightforward to separate the refractive index from the physical thickness of individual microscopic objects such as cells without assuming population averages for one of the two parameters. Therefore, the attenuation coefficient and RI measurement errors are converted to absorbance and OPL errors for reference when measuring such objects, yielding an absorbance sensitivity of $\sigma_{pt} = 0.1104$ OD and an OPL sensitivity of $\sigma_{pt} = 4.37$ nm.

4.4.2 Dispersion Evaluation: Water

After calibrating the microfluidic chamber's height and RI relative to air, the channel is filled with deionized water to evaluate the accuracy and precision of QPS for measuring fluidic samples. Figure 4.7 shows the measured holographic amplitude of the water-filled channel as well as the calculated refractive index of water. The amplitude, when averaged over an area of 360 μm^2 (671 spatial measurements), appears to have less spectral structure compared to the air-filled channel; this is likely due to a reduction in scattering at the glass-medium interfaces. The calculated RI spectrum of water is on average 0.0022 RI units below the literature values (black dashed line)[89], which indicates an error in measured Δn of 1.17% relative to the glass channel's RI. While the error is an order of magnitude larger than the spectral noise measured in section 4.4.1, after removing a Sellmeier RI fit from the measurements, the spectral noise is measured to be $\sigma_{pt} = 1.65 \times 10^{-4}$ and $\sigma_{avg} = 0.48 \times 10^{-4}$. The spectral noise is ~2.7× smaller than that measured in section 4.4.1; this improvement can be attributed to the decrease in coherent artifacts stemming from multiple reflections at the glass-medium interface. Furthermore, these numbers predict an OPL measurement sensitivity at each spatial point of $\sigma_{pt} = 3.32$ nm.

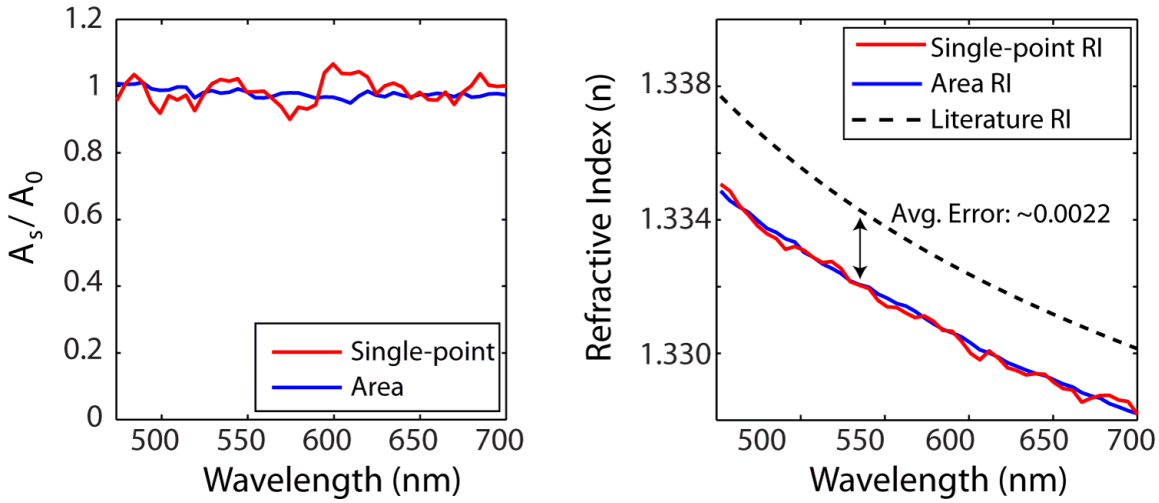

Figure 4.7 Measured amplitude and RI spectra of water in glass microchannel. Comparison of the area-averaged spectra (blue) to the single-point spectra (red) illustrates noise reduction by spatial averaging to remove coherent artifacts.

4.4.3 Rhodamine 6G in Ethanol: Molecular Concentration Determination

Absorbing molecules both attenuate incident photons and modulate the refractive index of the medium, creating both phase and amplitude spectral features. Therefore, hyperspectral holographic imaging systems can be used to measure molecular concentrations by probing both phase and amplitude. While the molar extinction coefficient and refractive index increment are linearly related by the Kramers-Kronig relations, amplitude and phase measurements exhibit distinct spectral noise characteristics. Therefore, this section evaluates how precisely amplitude and phase spectra may be used to extract concentration, as well as the ability to combine these two parameters for increased measurement precision.

Rhodamine 6G is a highly fluorescent molecule that absorbs light strongly in the green region of the visible spectrum, and is commonly used in dye lasers and ex vivo biological applications including fluorescence microscopy and flow cytometry. Four serial dilutions of Rhodamine 6G were prepared in ethanol, with nominal concentrations ranging from 5 mM to 1.25 mM. Although Rhodamine 6G absorbs so strongly at these concentrations that traditional absorbance measurements in 1cm cuvettes are infeasible, the 20 μm pathlength of the glass microchannel detailed above produces absorbance values that are detectable by holographic imaging yet do not overwhelm the dynamic range of the measurement system. The molar absorption coefficient and corresponding refractive index increment as calculated by the KK relations are shown in Figure 4.8 (A) & (B).

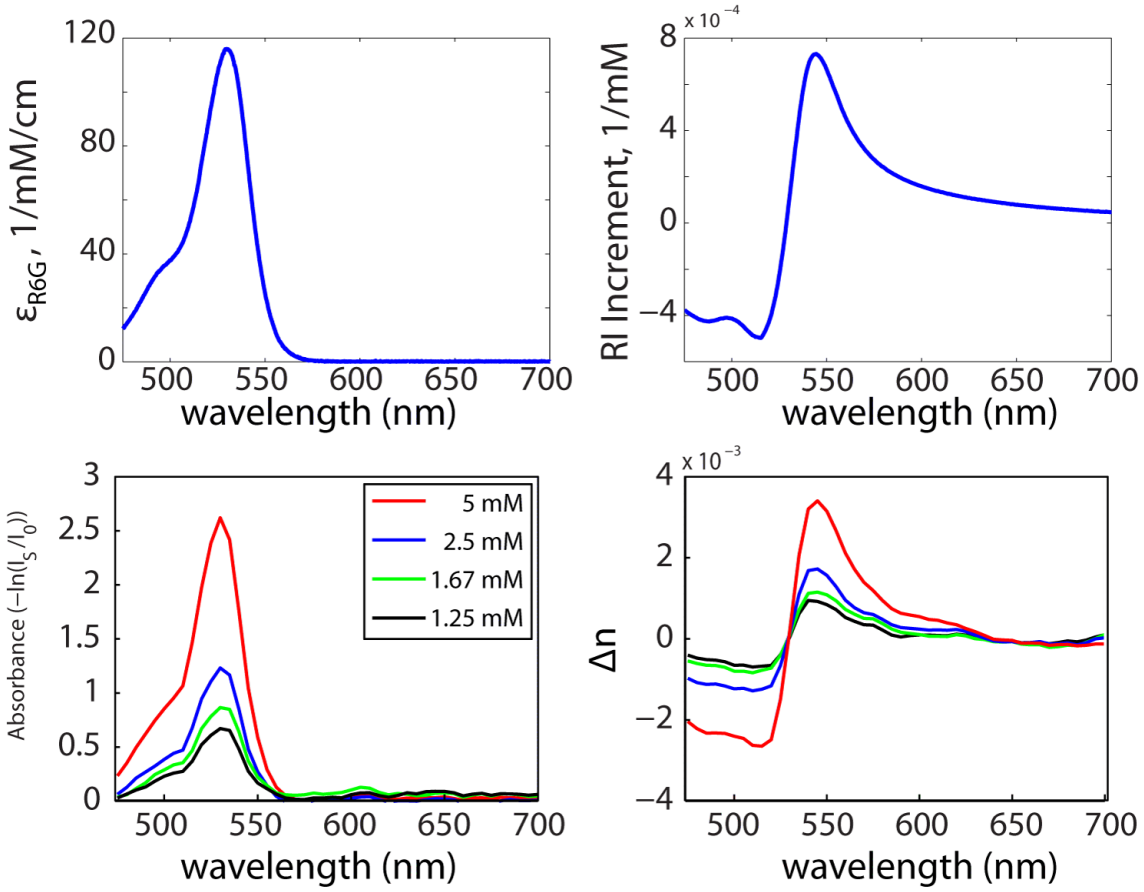

Figure 4.8: Literature molar extinction coefficient (A)[90] and calculated RI increment (B) of Rhodamine 6G in ethanol. Holographically-measured absorbance (C) and RI (D) of four R6G serial dilutions in glass microchannel.

Phase and amplitude spectra of the R6G dilutions were acquired from 475-700nm in 5nm steps, with spectral bandwidths of ~1-1.25 nm. The absorbance and RI spectra were then calculated at each point throughout the thickest section of the microchannel (d=20.140 μm, see section 4.4.1). Averaged absorbance and RI spectra over a 5.9 x 5.9 μm^2 area are displayed in Figure 4.7 (C) & (D) (121 measurements total, corresponding to a volume of 696 fL). The RI spectra have been detrended using a Cauchy equation fit, which removes components that correspond to the dispersion of ethanol relative to the

glass of the microchannel (constant w.r.t. λ, λ^{-2}, and λ^{-4}) and allows only the nonlinear refractive index contributions to be evaluated for concentration measurements.[14] The absorbance and nonlinear RI features clearly show a qualitative linear concentration-dependence.

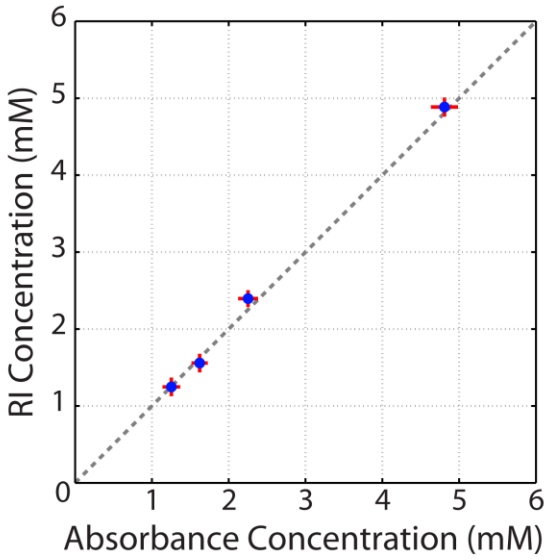

Figure 4.9: Consistency of RI- and absorbance-based concentration measurements. Dashed line shows agreement between the two measurements. Blue dots indicate area-averaged concentration measurements (5.9 x 5.9 μm² area, 696 fL effective volume). Red bars indicate the spatial standard deviations of concentrations measured over these errors.

R6G concentrations are recovered from each spatial location's absorbance spectra through linear least-squares regression using the Beer-Lambert law: $C(\lambda) = A(\lambda) / (\varepsilon(\lambda) \cdot L)$, where L is the thickness of the microchannel. Corresponding RI spectra are fit through linear-least squares regression to $C = \alpha_{R6G}(\lambda) / \Delta n(\lambda)$. The point-wise concentration measurements are then averaged over the 5.9 x 5.9 μm² area used in Figure 4.8. Figure 4.9 demonstrates that the concentrations measured by RI are

consistent with those calculated from absorbance. Furthermore, the spatial standard deviations over the ROI for both absorbance- and RI-based concentrations are similar (red bars), suggesting that both measurements are equally sensitive to concentration changes. Examining these values closer (Table 4.1), the uncertainty of the absorbance measurements appears to loosely increase as R6G concentration increases, while the RI-based uncertainty does not exhibit this trend. Despite this minor trend, the measurement uncertainty of the absorbance fits ($\sigma = 0.1318\ mM$) closely matches the uncertainty of the RI fits ($\sigma = 0.1187\ mM$). Note that the differences in measured concentrations compared to the nominal concentrations are likely due to slight inaccuracies in preparing the samples.

Table 4.1: Concentrations of R6G as measured by absorbance, RI, and combined

	Absorbance From Amplitude		*RI From Phase*		*Combined*	
Nominal	**Mean**	**Std**	**Mean**	**Std**	**Mean**	**Std**
5 mM	4.8087 mM	±0.1764	4.8869 mM	±0.1246	4.8478 mM	±.0676
2.5 mM	2.2528 mM	±0.1294	2.3964 mM	±0.1087	2.3246 mM	±.0655
1.667 mM	1.6217 mM	±0.1063	1.5586 mM	±0.1210	1.5901 mM	±.0503
1.250 mM	1.2543 mM	±0.1149	1.2483 mM	±0.1206	1.2513 mM	±.0588

Amplitude and phase measurements are sensitive to different optical processes: amplitude measurements probe the relative number of photons absorbed by the sample, while phase measures the temporal delay of photons that are transmitted through the sample. Furthermore, amplitude values are nonlinearly transformed to produce absorbance measurements. Therefore, the hyperspectral absorbance and RI data exhibit disparate noise characteristics, and the two measurements potentially could be

combined to improve the accuracy of concentration determination. To demonstrate this effect, each of the absorbance-based and RI-based concentrations at each spatial location are averaged (Table 4.1, "Combined" column) and the spatial standard deviation is taken over the averaging area. The resulting concentration uncertainty is improved ~2× over the individual measurements for each of the 4 concentrations examined here.

4.5 Summary

In this chapter, several methods for analyzing quantitative phase data were presented. Section 4.1 outlined a procedure for digitally refocusing holograms using Fresnel propagation and reviewed potential criteria that can be used to automate the refocusing process. Section 4.2 presented the mathematical framework for optical volume measurements, showing that OV is an effective metric for comparing microscopic objects whose exact physical dimensions and refractive index are unknown. This section also demonstrated that the correct hologram focus is critical for making precise OV measurements. The remainder of the chapter addressed digital image processing methods specific to quantitative phase spectroscopy. Section 4.3 analyzed the effects of partially-coherent light on phase noise and described a framework for reducing coherent artifacts in phase images by spectral averaging. Finally, Section 4.4 detailed a set of experiments validating the utility of QPS for measuring absolute refractive index, dispersion of aqueous samples, and the concentrations of strongly absorbing molecules in sub-picoliter volumes using both amplitude and phase

information. Taken together, the hologram processing methods presented here provide a set of tools for advanced quantitative analysis of individual cells in Chapters 6 & 7.

5 Imaging Refractometry of Microbicidal Films

5.1 Introduction

Section 3.1 outlined the details of the off-axis quantitative phase microscope, which allows quantitative phase images to be recovered from single time-points. Here, Chapter 5 describes the application of this microscope system for measuring spatial distributions of microbicide films as they hydrate. This study uses QPM measurements to compare the hydration and dissolution kinetics of a panel of film candidates loaded with tenofovir (TFV), an antiretroviral drug that has shown promise as a topical vaginal prophylactic against HIV infection.[24,25] These dynamic processes impact drug release profiles and ultimately underlie drug pharmacokinetics. We begin with a brief description of the assay configuration, which allows different film compositions to be measured and directly compared (section 5.2). After establishing the experimental technique, section 5.3 describes the data processing methods used to analyze each film sample. Next, the film compositions, geometries, and summary optical characteristics are briefly described in sections 5.4.1-5.4.2. Finally, the remainder of section 5.4 presents data that show both the structural and dynamic dissolution differences of the four distinct polymeric compositions. The results of this study demonstrate that QPM is capable of measuring detailed spatial and temporal features of polymer drug delivery vehicles during film hydration and disintegration. The demonstrated assay and analysis

methods can aid both our understanding of *in vivo* film behavior as well as the development of films that are effective for vaginal delivery of anti-HIV microbicides.

5.2 Experimental Design

The hydration dynamics of microbicidal film samples were examined in a reusable flow chamber (Bioptechs, FCS3 chamber) as seen in Figure 5.1. The upper surface of the flow chamber consists of a round piece of glass with inlet/outlet flow ports and a 250μm-thick rubber gasket around the edge. A custom designed transparent physical ramp composed of Sylgard 184 (Dow Corning) functions as a refractive index reference and had previously been bonded to the center of a clean #0 coverslip, which serves as the lower surface of the chamber. The ramp is the same thickness as the rubber gasket and makes contact with the top surface when the chamber is sealed, thus forming a section of the image in which the refractive index is known and remains constant throughout the hydration experiment. Film samples for the hydration assay are cut from the manufactured sheets using a 1-mm biopsy punch and gently pressed flat against the round coverslip in close proximity to the reference ramp using the blunt end of a pair of tweezers (Figure 5.1C); the films do not deform under this pressure, but also adhere to the glass strongly enough to prevent lateral motion when the chamber is filled with water.

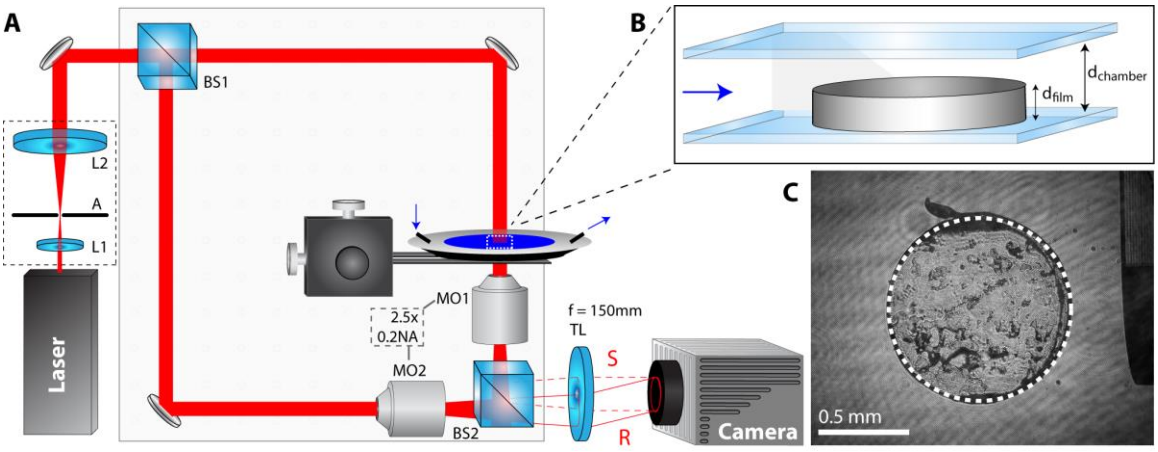

Figure 5.1: Microscope and flow chamber configuration & hydration assay, as seen in Rinehart, *et al.*[91] (A) Experimental setup for film hydration studies, λ=632.28m. (B) The blue arrows indicate water flow at t = 0, which begins the process of hydration. (C) Imaging field of view, containing 1mm film sample and reference ramp structure.

After preparing the sample, water is rapidly injected into the chamber using a syringe pumped by hand until the entire chamber is filled (~2-3s). After the film sample is completely immersed and the chamber is filled, flow is halted. Interferograms are acquired every 2s for 20 minutes as the films hydrate and dissolve. Then, the chamber is flushed with water to remove all film material, and a final interferogram of the empty chamber is acquired to serve as a reference phase measurement. The hydration assay was repeated three times for each of the four film compositions listed in Table 5.1.

5.3 Data Analysis

5.3.1 Relating Phase Measurements to Dry Mass

Quantitative phase images are recovered using the processing methods described in sections 3.1.2 and 3.1.3, and 2π ambiguities are removed using a

combination of spatial[52] and temporal[56] unwrapping as described in section 3.1.4. This spatiotemporal unwrapping method produces a map of the relative phase delays under the assumption that the phase does not change by more than π radians between adjacent spatial locations and time points.

Because each polymer composition has differing refractive indices, phase images must first be converted to refractive index maps, which must then be mathematically decomposed into film and water fraction components. The average refractive index is calculated from the phase images, $\Delta\varphi(\vec{r},t)$, as:

$$\bar{n}(\vec{r},t) = \frac{\Delta\varphi(\vec{r},t)}{d_{chamber}} \frac{\lambda}{2\pi} \tag{5.1}$$

where the chamber height is measured by digital calipers to be $d_{chamber}$ = 250 ± 10 μm. $\bar{n}(\vec{r},t)$ is the refractive index averaged over the height of the chamber, comprising a linear combination of polymeric film and water refractive indices:

$$n_{h_2o} d_{h_2o} + n_f d_f = \bar{n}\left(d_{h_2o} + d_f\right) \tag{5.2}$$

The height of the sample chamber along with the xy-lateral dimensions of the microscope form voxels whose refractive indices are linear combinations of the RIs of the water, n_{h_2o}, and film, n_f, components weighted by the composite height of the water and film, d_{h_2o} and d_f, respectively. The percent fraction of polymer contained in each voxel, $F(\vec{r},t)$, is calculated as:

$$F\left(\vec{r},t\right)=\frac{\overline{n}\left(\vec{r},t\right)-n_{h_2o}}{n_f-n_{h_2o}}*100 \tag{5.3}$$

The polymer mass density distribution, $M\left(\vec{r},t\right)$, is finally calculated as:

$$M(\vec{r},t)=F(\vec{r},t)*250\times10^{-6}\,\frac{ml}{mm^2}*\varrho_f \tag{5.4}$$

using the fixed geometry of the chamber as well as the density of each film (ϱ_f in *g/ml*, see Table 5.2).

5.3.2 Spatial Fourier Analysis of Mass Density

Hydration dynamics of the varied polymer films may be further compared using spatial Fourier analysis (SFA) of the mass density distributions to measure how each radial spatial frequency evolves over time. SFA has previously been utilized as a tool for studying diffusional transport of molecular solutions: spatial frequency amplitude and phase changes can be indicative of diffusional or flow phenomena.[92,93]

The mass density distributions (Figure 5.2 (A)) are first interpolated to polar coordinates (Figure 5.2 (B)), then Fourier transformed in the radial dimension, and finally averaged over θ to yield the time decay of the power spectral density contained in each of the spatial frequency components $\left\langle \hat{M}(\rho,t)\right\rangle_\theta$ (Figure 5.2 (C) & (D)). Specific characteristic length scales, $R = 1/\rho$, are then compared across the varied films.

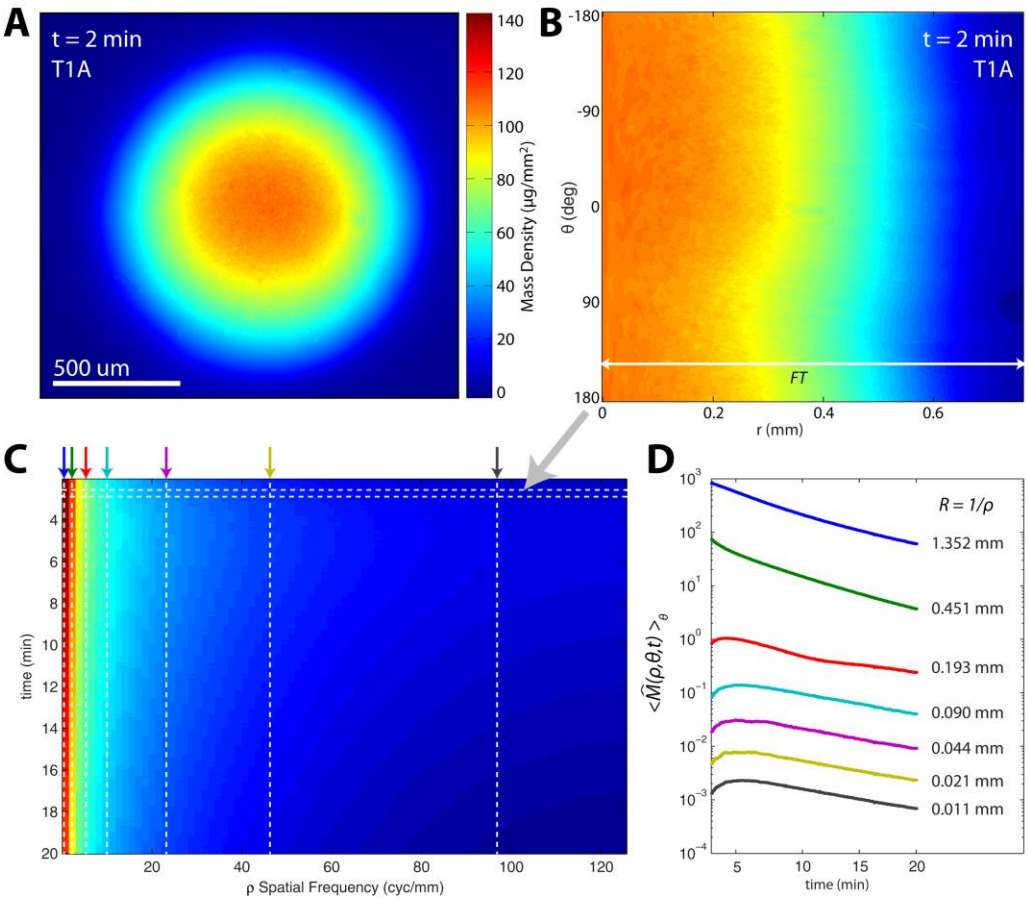

Figure 5.2 Spatial Fourier analysis of mass density, as taken from Rinehart, *et al.*[91]

5.4 Results

5.4.1 Microbicidal Film Characteristics

Microbicidal films were manufactured according to the formulae presented in Table 5.1 using a solvent casting method similar to that described by Akil, *et al.*[30] Thin 8- x 12-inch sheets were cast, dried, and cut into individual 1- x 2-inch strips using a die press. Post-evaporation water content was measured using a Karl Fisher titration apparatus. Resulting film thickness was measured with mechanical calipers with a measurement resolution of ± 10µm. Four tenofovir-loaded films were manufactured for

evaluation (Table 5.1): Three differ in polymer composition but retain identical geometry (T1A, T2A, and T3A), while two share the same composition but differ in thickness (T1A and T1B).

The initial compositions, residual water content after evaporation, thickness, and refractive indices of each film composition are summarized in Table 5.1. While Films T1A and T2A differ in composition only slightly (2%), T3A contains two unique polymers and almost double the glycerin content of T1A and T2A. The higher refractive indices of films T1A and T3A are due to the inclusion of sodium carboxymethylcellulose (NaCMC, n = 1.515) while T2A does not contain NaCMC and thus has a lower refractive index.

Table 5.1: Compositions and Thicknesses of films, taken from Rinehart, *et al.*[91]

	Composition prior to evaporation									Post-evaporation properties		
	PVP	MC	HPMC	HEC	Na CMC	TFV	GLYC	NaOH	H_2O	H_2O	Thickness (μm)	RI
T1A	--	--	6	6	2	2	2	0.28	81.72	5.47	120	1.486
T2A	--	--	7	7	--	2	2	0.28	81.72	7.15	120	1.477
T3A	10	2	--	--	2	2	3.6	0.28	80.12	10.51	120	1.485
T1B	--	--	6	6	2	2	2	0.28	81.72	7.31	240	1.486

* All values are given as % w/w, except for thicknesses and RIs.
* Ingredient abbreviations: hydroxyethyl cellulose (HEC), hydroxypropyl methylcellulose (HPMC), carboxymethylcellulose sodium (NaCMC), Tenofovir (TFV), glycerin (GLYC), sodium hydroxide (NaOH), polyvinylpyrrolidone K90 (PVP), methyl cellulose (MC), water (H_2O)

5.4.2 Refractive Index Measurements

The RIs of each of the four films were determined using a surface refractometer (Bellingham & Stanley, RFM 340). The RI of equilibrium serial dilutions of each of the polymer film samples in deionized (DI) water were measured and fit to a linear model

as $n(C) = dn/dC_v * C_v + n_{h_2o}$, where C_v is the volume concentration, to determine the volume-fraction refractive increment, dn/dC_v for each film. These values were then converted to volume-to-mass RI increments, α (this parameter is widely reported in interferometric dry mass analysis of biomaterials[81,83,94]) using film densities calculated from compositions reported in Table 5.1.

The calculated densities, fitted α increments, and calculated RI for each of the experimental films and DI water are summarized in Table 5.2; error bars correspond to the 95% confidence bounds of the fit model. Film T3A exhibits a significantly lower RI increment than the other three films despite having a similar RI to T1A; this is due to the T3A composition having a significantly higher density than the other compositions.

Table 5.2: Specific film refractive indices and measured dissolution parameters from Rinehart, *et al.*[91]

	dn/dc (ml/ml)	Density, ρ_f (g/ml)	α (ml/g)	Refractive Index	τ_H (m:ss)	Λ	Γ
H_2O		1.000		1.3329 ± .0001			
T1A	0.154 ± .002	1.183	0.130 ± .002	1.486 ± .002	5:16	.076 ± .002	0.165 ± .033
T2A	0.144 ± .001	1.118	0.129 ± .001	1.477 ± .001	5:44	.105 ± .003	0.253 ± .100
T3A	0.151 ± .008	1.315	0.115 ± .006	1.485 ± .008	8:52	.016 ± .001	0.061 ± .031
T1B	0.154 ± .002	1.180	0.130 ± .002	1.486 ± .002	7:48	.116 ± .003	0.125 ± .007

* α values are given as mean ± 95% CI. τ_H is hydration time; Λ and Γ given as mean ± σ.

5.4.3 Effects of Film Thickness on Hydration

Figure 5.3 compares the hydration and dissolution of two film samples with identical polymer compositions but different thicknesses, T1A and T1B. Representative film volume fraction images (Figure 5.3 (A)) reveal qualitative differences in kinetics

over the experimental time course while summary volume fraction time curves (volume average over the initial film area, r = 0 mm to r = 0.5 mm) quantify these differences and also display the variability in measurements across three repeats of the assay for each film type (Figure 5.3 (B)). Initially, T1A contains half the volume of polymer as T1B. The fractional volume of T1A polymer within the initial area remains approximately half that of T1B, indicating that both films spread laterally at approximately the same rate. It is also worth noting that the phase data from the thinner film T1A was free of wrapping artifacts within 2 minutes of initial hydration while data from the thicker film T1B exhibited phase wrapping artifacts for 7 minutes after initiating hydration.

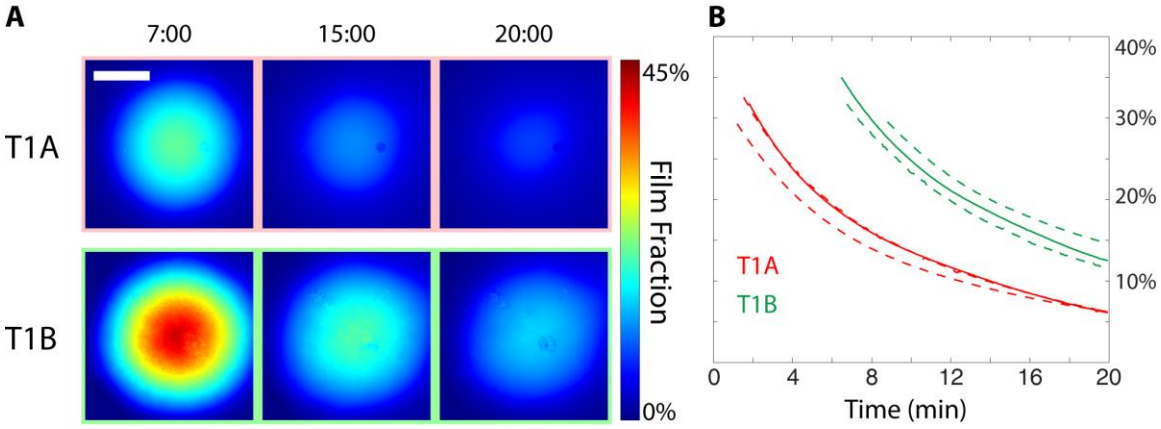

Figure 5.3: Comparison of two films with different thicknesses, T1A (120μm) and T1B (240μm). (A) Calculated film fraction at 7, 15, and 20 minutes. (B) Film fraction remaining within the initial circular film area during hydration. The three repeats of T1A (red) show a distinctly faster hydration rate than the repeated measurements of samples from the T1B film (blue). Solid lines indicate experimental data depicted in (A), while dashed lines are data from repeated experiments with identical conditions. Scale bar: 0.5mm. Figure taken from Rinehart, et al.[91]

5.4.4 Effects of Film Composition on Hydration

The hydration experiments were repeated with the three films of different compositions to explore the effect of composition on hydration dynamics (Figure 5.4). As in Figure 5.3, part (A) compares the qualitative differences in dissolution across the three samples at coarse intervals. T2A appears to contain the most polymer material 2 minutes after hydration, yet decays to the least remaining material after 20 minutes. While it is difficult to quantify the decay rates by visual inspection, both T1A and T3A appear to have similar temporal hydration rates, with T3A containing a larger film fraction 2 minutes after hydration. Figure 5.4 (B) confirms that the decay rates of T1A and T3A are similar, and that T2A decays much faster than either of the other two films. The variability in the T3A repeats may be due to initial thickness (±10μm) variation. The differences in film fraction remaining in the FOV after 2 minutes of hydration are attributed to early kinetic differences during which phase unwrapping errors obscure the data.

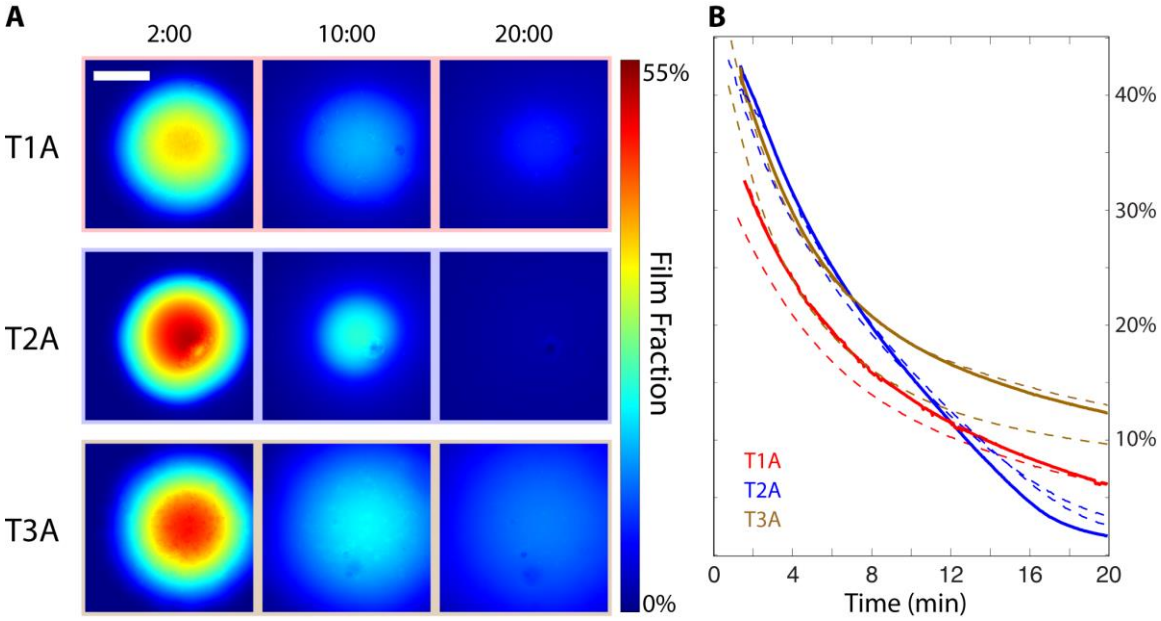

Figure 5.4: Comparison of three distinct film formulations as summarized in Table 2. (A) Calculated film fraction at 2, 10, and 20 minutes. (B) Film fraction remaining within the initial circular film area during hydration; Solid line corresponds to the hydration time course represented in (A), dashed lines correspond to triplicate repeat experiments and demonstrate assay variability/repeatability. Taken from Rinehart, *et al.*[91]

5.4.5 Radial Mass Density Profiles: Macroscopic Hydration Behavior

The polymer samples are circular, and appear to hydrate in a symmetric fashion; therefore, the azimuthally-averaged dry mass density images shown in Figure 5.5 illustrate the macroscopic radial hydration behavior. Both T1A and T2A exhibit an inflection point that remains visible after initial hydration and migrates inward during continued dissolution. T3A lacks this inflection feature, possibly due to its compositional differences to T1A and T2A (Table 5.1). While the thicker film T1B lacks this inflection point, it is compositionally identical to T1A. It is postulated that this feature is absent from T1B's mass density profiles due to both the limited field of view

and limited experimental time course; the T1A samples contain half of the total polymer material as T1B and exhibits this inflection point near the edge of the field of view. Given a longer experimental time course, a larger imaging FOV, or a smaller initial sample size, it is expected that the same feature would be visible in T1B's mass density profiles.

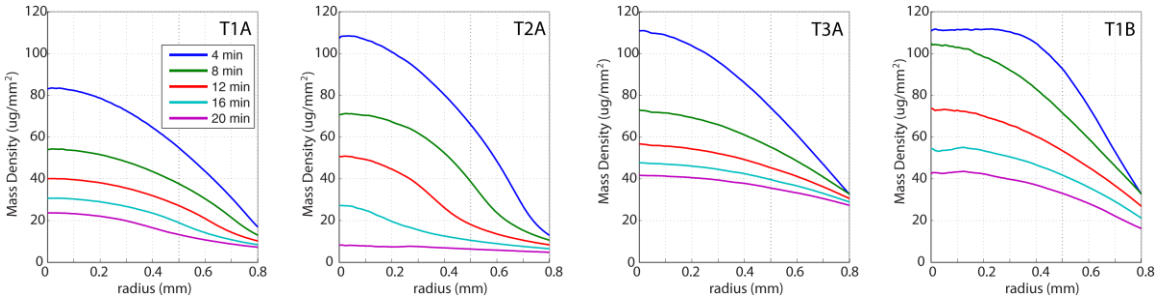

Figure 5.5: Azimuthally-averaged radial plots of mass density showing temporal dissolution, taken from Rinehart, *et al.*[91]

5.4.6 Spatial Frequency Analysis: Microscopic Hydration Behavior

Radial mass density profiles presented in section 5.4.3 are Fourier transformed and averaged according to the methods described in section 5.3.2 in order to examine the spatial frequency content at each time point. Spatial frequency analysis (SFA) can be used to quantify the dynamic behavior of matter in a system at characteristic length-scales $R = 1/\rho$. Dissolution can involve multiple mechanisms, including polymer chain disentanglement, fragmentation, swelling, and diffusion;[20–22] during these processes, the energy contained in specific length scales are expected to be modulated.

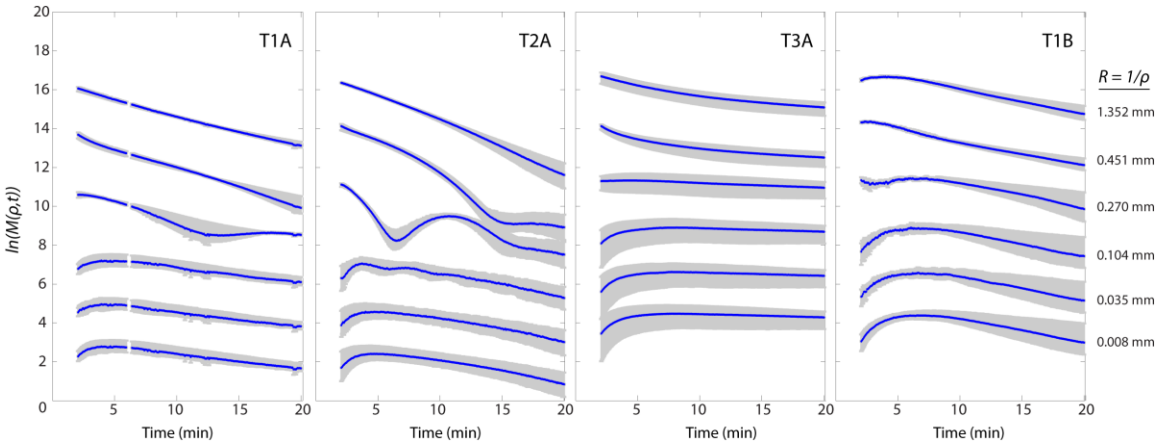

Figure 5.6: SFA reveals temporal differences of characteristic length scales across film sample compositions. Blue lines indicate mean values across three repeats, and gray ranges indicate standard deviations. Taken from Rinehart, *et al.*[91]

Figure 5.6 compares the decay of energy across the four films during hydration and subsequent disintegration. The smallest length scales represent features corresponding to the resolution limit of the interferometric imaging system, while the largest length scales characterize the macroscopic shape of the film samples. During early swelling and polymer chain disentanglement, the amplitudes for characteristic length scales less than 0.27 mm increase in relative contribution for all film samples. Films T1A and T2A also exhibit damped oscillations in length scales between 0.2-0.5mm due to complex polymer-solvent interactions; these oscillatory features do not appear in T3A, whose physical properties differ significantly as observed in sections 5.4.1-5.4.2. All of the curves appear to approach uniform decay rates as dissolution continues.

Each film's spatial frequency time series is divided into two regimes at τ_H, the time at which all spatial frequencies have passed their maximum value. This division

demarcates (1) an initial hydration regime during which there is a net generation of polymer fragment features at some length scales from (2) a subsequent dissolution regime during which all length-scale features diminish in magnitude as the system proceeds toward an equilibrium of water and polymer.

The hydration times for films T1A and T2A are quite similar, at 5:16 and 5:44, respectively; τ_H of the T3A samples is much longer at 8:52. This difference parallels the distinct composition and radial mass-density differences observed previously. Doubling the film thickness without altering the polymeric composition (T1A=120μm, T1B=240μm) increases τ_H from 5:16 to 7:48. These hydration-to-dissolution transition times τ_H are recorded in Table 5.2.

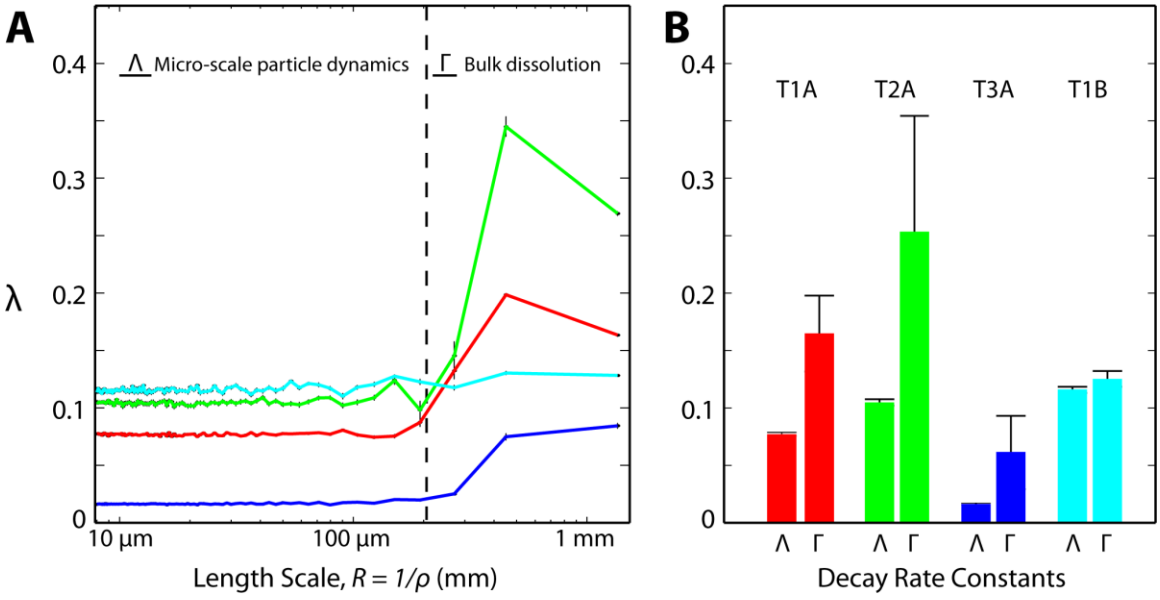

Figure 5.7: Spatial frequency decay rates.

Each characteristic length scale's dissolution regime curve is fit to an exponential decay: $e^{-\lambda(R)t}$ to determine a decay rate, λ. There is a clear difference in decay behavior between the bulk material distribution and the micron-scale particle dynamics, which are separated at a visually-chosen length scale of $R = 200\ \mu m$ (Figure 5.7 (A) dashed line). The decay rates of each film's bulk ($\Gamma = \langle \lambda \rangle_{R>200\mu m}$) and micron-scale ($\Lambda = \langle \lambda \rangle_{R<200\mu m}$) features are averaged and summarized in Figure 5.7 (B); the black bars indicate variability across three repeated assays of each film type.

While all films exhibit larger bulk decay rates, Γ, than micron-scale decay rates, Λ, increasing the film thickness appears to increase Λ and decrease Γ (red T1A *d=120μm* vs. blue T1B *d=240μm*). Varying composition while maintaining physical geometry (T3A vs. T1A/T2A) affects both Γ and Λ, however the macroscopic decay rate remains significantly higher than the microscopic particle decay rate for all three of these films. These variations indicate that polymer composition and geometry not only modulate the bulk rate of dissolution, but also the rate at which smaller-sized objects are generated and decay. Both the macroscopic and microscopic dissolution kinetics are expected to have a distinct influence on the film's ability to spread across and deliver API to a target tissue.

Pure diffusion is governed by Fick's second law, which predicts that the magnitude of the power spectrum of radial spatial frequencies to decay as:

$$\hat{M}(\rho,\theta,t) = \hat{M}(\rho,\theta,0)\,\mathrm{e}^{-4\pi^2 D\rho^2 t} \tag{5.5}$$

where $\hat{M}(\rho,\theta,0)$ is the initial mass density distribution and D is the diffusion coefficient[92,93]. In a homogeneous diffusive system, the fit parameter displayed in Figure 5.7, λ, should be proportional to the diffusion coefficient after normalization by the square of the spatial frequency, ρ^2, and would provide a robust method of recovering D.[92] However, normalizing λ produces values of D that vary both temporally and with spatial frequency; this suggests that while diffusion may play a role in the dynamic hydration kinetics, additional mechanisms of mass transport contribute significantly and limit our ability to parameterize any of the films' behaviors through diffusion coefficients.

5.5 Discussion

Topical drug delivery by films requires careful control, not only of the drug release rate but also of the spatial distribution of the active pharmaceutical ingredient (API). Although the polymer vehicle's uptake of fluid and consequent swelling, disintegration, and dissolution, govern drug release, there has been little study of the spatial behavior of film material itself, which underlies API delivery.[30,31] In the experiments presented here, quantitative imaging refractometry is demonstrated to be an effective tool for investigating differences in the water uptake and material dissolution. Film prototypes with different thicknesses as well as polymeric compositions were assessed using the approach. The measured refractive index

distributions during dissolution enabled calculations and comparison of film volume fractions, mass density profiles, and spatial Fourier analyses of various film designs.

While the analyses of film disintegration presented here illuminate differences in hydration kinetics due to sample geometry and composition, the precision and accuracy of the quantitative imaging refractometry measurements are bounded by several factors. The spatiotemporal phase noise is bounded by the sensitivity of the interferometric system and digital processing, which yield a refractive index sensitivity of $\sigma = 5.5\text{x}10^{-6}$.[33] This sensitivity corresponds to a film fraction measurement precision of 0.0035-0.0038 pp and a mass density measurement precision of $\sigma_M = 0.98 - 1.25$ μg/mm^2. The errors in film and water RI measurements given in Table 5.2 determine the absolute accuracy of the measured film fractions and mass density maps.

In addition to these bounds on measurement precision and absolute accuracy, phase wrapping artifacts can also corrupt the data. Phase wrapping presents a major challenge in holographic phase imaging of thick objects; artifacts are non-deterministic and vary depending on the exact unwrapping algorithm employed. Based on the geometry of the chamber, each 2π wrapping artifact contributes a discrete error of $\varepsilon = 2.5\text{x}10^{-3}$ RI units. The exact influence of 2π wrapping errors on volume fraction depends on the propagation of error through equations (5.2) and (5.3). Using the range of RIs of the films reported in Table 5.1, each phase wrapping artifact contributes a film volume fraction error of 1.65-1.76 percentage points. During initial hydration (t < 2:00 for T1A,

T2A, T3A; t < 7:00 for T1B), the measured phase information contains significant wrapping artifacts, rendering QIR data unsuitable for analysis. After this time period, the phase distributions become smooth and are unwrappable using standard techniques (Section 3.1.4) during the remainder of the disintegration assay.

Once in a time regime where phase unwrapping is successful, the system accuracy and precision determine the fidelity of the data. The variability in dissolution kinetics across multiple repeats of each film are larger than the measurement accuracy and are attributable to experimental variability in the samples' initial geometries and polymer kinetics. Averaging the data across repeated experiments for each film type uncovered underlying trends. A thicker film (T1B, d = 240 μm) dissolved and spread slower than the thinner film of the same formulation (T1A, d = 120 μm), and contained approximately twice as much material in the initial film area at the end of the 20 minute assay (T1B = 12.5%, T1A = 6.2%). Varying the polymer composition while maintaining identical thickness (T1A, T2A, T3A d = 120 μm) produced films with diverse dissolution rates and spatial characteristics, as demonstrated by measurements of material remaining within the initial film area as well as SFA analysis and subsequent decay rate fitting (Λ and Γ). These results illustrate that the composition and geometry of the polymer vehicle can affect both macroscopic and microscopic dissolution kinetics, which in turn can vary independently.

5.6 Summary

In this chapter, QPM was applied as a novel assay for measuring distributions of topical microbicide films undergoing hydration and dissolution. An experimental setup based on a flow chamber was designed to allow standardized comparison of film samples manufactured with varied polymer compositions and thicknesses. Film distribution and mass density maps were calculated from quantitative phase images captured over 20 minutes and were further analyzed by spatial Fourier analysis. Film thickness was found to slow the rate of hydration, while both thickness and composition were found to affect both the microscopic and macroscopic spatiotemporal dissolution kinetics. These results can be used in conjunction with mathematical models of film hydration and distintegration[32] to improve our understanding of polymer vehicle behavior and its impact on efficient topical drug delivery.

6 QPS Spectral Characterization of Infected RBC Populations

6.1 Introduction

Building on the methods for spectroscopic analysis discussed in Chapter 4, this chapter presents the application of QPS for characterizing the physiological state of red blood cells (RBCs) infected with *P. falciparum*, the primary cause of malaria worldwide. *P. falciparum* parasites invade individual cells and consume hemoglobin as they grow during their ~48-hour life cycle.[95] Section 6.2 outlines the preparation of samples, image acquisition and processing methods, and details how the resulting spectra are analyzed to estimate the mass of hemoglobin remaining in each cell. Section 6.3 compares the OV, spectra, calculated hemoglobin masses, and morphology of RBC populations imaged by QPS. Section 6.4 discusses the demonstrated advantage in using OV with spectral dependencies to enhance previously used QPM methodology, and points toward methods and future studies that may be used to automatically classify infected RBCs with high sensitivity.

6.2 Methods and Procedures

6.2.1 *P. falciparum* Culture & Isolation

The malaria-causing *P. falciparum* parasite is cultured in RBCs to a parasitemia of ~2-5% using a technique to synchronize the 48-hour life cycle. Cells containing *P. falciparum* are isolated by fractionating the RBC population by density in a Percoll

density gradient. RBCs containing schizont-stage parasites are isolated and washed to remove the Percoll medium before resuspending in a solution of 300 mOsm isotonic PBS. Cells are then loaded into a capillary tube as described above for imaging.

6.2.2 Cell Preparation

Different populations of blood cells, both normal and parasite infected, are prepared as follows. The cells are first diluted with a mixture of 300 mOsm phosphate buffered saline (PBS) and 0.075% (grams / 100ml) fraction-V bovine serum albumin (BSA) to a concentration of 0.01 – 0.04%. While the quantity of BSA is extremely low relative to the standard human serum albumin reference range (~3-5.7%)[96], the addition of BSA at this level is seen in our experiments to stabilize the morphology of human RBCs and does not significantly alter the RI or osmolarity of the PBS media. 60 μL of the dilute cell solution is then loaded into a rectangular glass capillary tube (VitroCom) with an inner thickness of ~0.3mm. The cells settle to the bottom glass surface within ~5 minutes of loading and remain stationary in the FOV for the duration of image acquisition.

6.2.3 Image Acquisition and Segmentation of Cells

QPS hyperspectral hologram datasets are acquired and processed according to the general methods described in section 3.2, the specific procedure for these studies is briefly reviewed here. Holograms are captured at center wavelengths ranging from 475nm – 700nm in 5nm steps; 8 spectral sweeps are performed in 5-6s, capturing 32 total

holograms at each wavelength. The fields of view (93.5×93.5 μm) contain ~5-15 cells each, as seen in Figure 6.1(A). The holographic data are referenced to a background set of holograms taken at a nearby cell-free region of the channel and then all complex amplitude and phase images at each wavelength are averaged. The resulting amplitude images are flatted by subtracting a 1st order polynomial while the phase images are flattened by a 5th order polynomial surface; each surface is fitted to the regions of the FOVs that do not contain cells. After flattening, the amplitude and phase images at each wavelength are digitally refocused (section 4.1) according to the spectral defocus measured using a resolution target before being resized and aligned (section 3.2.4). The cells in the resulting amplitude and phase images are all in focus and contain no chromatic defocus.

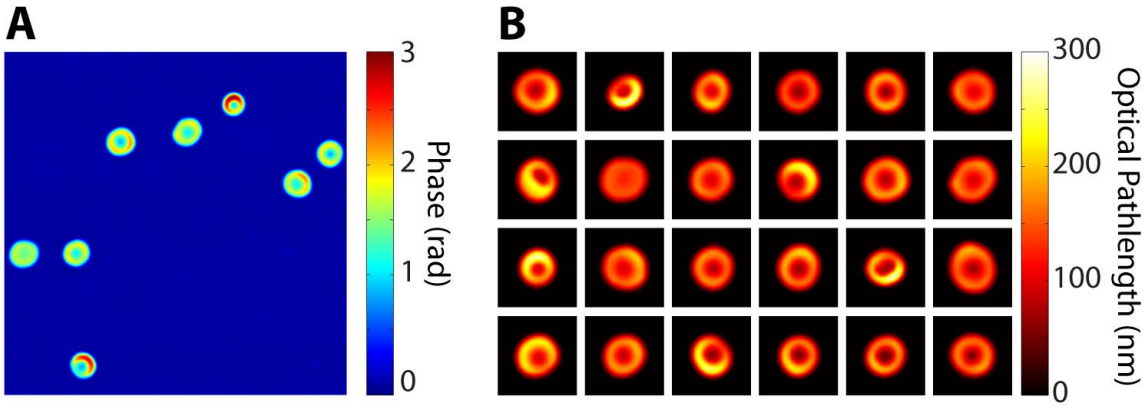

Figure 6.1: (A) Phase image of multiple RBCs in a field of view (93.5 x 93.5 μm FOV). (B) Individual cells after semi-automated segmentation (13.5 x 13.5 μm FOV each)

After conditioning the amplitude and phase images, the location of each cell is automatically identified by thresholding the phase images at 0.1 radian. Objects that are

too small (non-RBCs) or too large (clumps of cells) as well as cells that are on the borders of the FOVs are manually excluded from the data. Approximately 4-10 FOVs are captured for each sample, resulting in 35-42 segmented cells per population (Figure 6.1 (B)).

6.2.4 Mass Quantification of Molecules of Interest

In order to quantify the RBC observations we will calculate actual mass of hemoglobin in cells of each population by two methods, absorbance spectra (amplitude considerations) and optical volume spectra (phase considerations). We first return to the analysis used in section 4.4, which demonstrated the utility of QPS in determining concentrations of the strongly-absorbing molecule Rhodamine 6G in a microchannel with a fixed thickness. In that example, amplitude measurements were related to the spectral absorbance while phase measurements were related to relative refractive index spectra, calculated by the Kramers-Kronig relations. The subtractive KK relations are most widely used in the literature relate the real and imaginary part of the RI (n and κ)[14,16,97–100]:

$$\Delta n(\omega) = \frac{2}{\pi}(\omega^2 - \omega_0^2) P \int_0^\infty \frac{\omega' \kappa(\omega')}{(\omega^2 - \omega'^2)(\omega_0^2 - \omega'^2)} d\omega' \qquad (6.1)$$

However, the two sides of equation (6.1) can be manipulated to relate the refractive index increment of a material to the molar exctinction coefficient, ε. Note that the molar

exctinction coefficient may be specified in Naperian (e-based) or decadic (10-based) units. The imaginary part of the RI, κ, in equation (6.1) is related to the decadic ε as:

$$\omega \cdot \kappa(\omega) = \ln(10) \cdot \frac{c_0}{2} \varepsilon(\omega) \cdot Conc. \tag{6.2}$$

where c_0 is the speed of light in vacuum, ω is the optical frequency, and *Conc.* is the concentration of the molecule of interest. Substituting equation (6.2) into (6.1) and dividing both sides by the concentration yields the integral relationship between the relative RI increment, $\Delta\alpha(\omega)$, and molar absorption coefficient:

$$\Delta\alpha(\omega) = \frac{c_0}{\pi}(\omega^2 - \omega_0^2) P \int_0^\infty \frac{\varepsilon(\omega')}{(\omega^2 - \omega'^2)(\omega_0^2 - \omega'^2)} d\omega' \tag{6.3}$$

Equation (6.3) is derived from the subtractive KK relation calculated over a truncated spectral range; therefore, the relative RI increment indicates spectral features relative to the RI increment at ω_0. The absolute spectral RI increment would be calculated as $\alpha(\omega) = \alpha(\omega_0) + \Delta\alpha(\omega_0)$.

In the experiments presented below, the pathlength of the absorbers are not known. Therefore, the total mass of hemoglobin within the projected surface area of each cell is calculated from amplitude and phase images rather than the concentration within each cell. Intensity per unit area is calculated from the measured relative amplitude images before calculating absorbance in units of optical density (OD) as

$A(\lambda) = -\ln(\frac{I}{I_0})$. The resulting absorbance is related to the decadic molar extinction coefficient as:

$$A(\lambda) = \ln(10) \cdot \varepsilon_{10}(\lambda) \cdot Conc. \cdot L \tag{6.4}$$

where *L* is the pathlength and the concentration is expressed in terms of moles/volume. Rearranging equation (6.4) yields:

$$\frac{A(\lambda)}{\ln(10) \cdot \varepsilon_{10}(\lambda)} = Conc. \cdot L \tag{6.5}$$

The product of concentration and pathlength *L* is in units of moles/area, and is integrated over projected surface area to recover the quantity of the molecule of interest within a region of the image (in this case, each cell).

Similar to the amplitude-based quantification, phase images are processed to estimate molecular quantity by first converting them to optical pathlength images and then integrating over projected surface area to recover the optical volume (section 4.2). The RBC intracellular environment is modeled in the literature[10,12] as

$$n_{cell}(\lambda) = n_{H2O}(\lambda) + \alpha_{HbO2}(\lambda) \cdot Conc_{HbO2} + n_X(\lambda) \tag{6.6}$$

where $n_X(\lambda)$ accounts for dispersion arising from non-hemoglobin proteins and other biomolecules, and $Conc_{HbO2}$ is expressed as the ratio of the mass of hemoglobin to the total cell volume. Inserting equation (6.6) into the equation for optical volume (equation (4.6)) yields:

$$OV(\lambda) = (n_{water}(\lambda) + n_X(\lambda) - n_m(\lambda)) \cdot V + \alpha_{HbO2}(\lambda) \cdot m_{HbO2} \qquad (6.7)$$

where $n_m(\lambda)$ is the RI of the surrounding media. Hemoglobin is the only molecule in a normal RBC with significant spectral features in the visible range, with $n_m(\lambda)$, $n_{water}(\lambda)$, and $n_X(\lambda)$ accounting for dispersion. Fitting the OV to the three-term Cauchy equation, $n(\lambda) = B + \frac{C}{\lambda^2} + \frac{D}{\lambda^4}$ removes volumetric contributions arising from RI mismatch and dispersion and leaves only the nonlinear spectral features due to hemoglobin. These spectral features are then quantified by fitting to the relative RI increment of hemoglobin, $\Delta\alpha_{HbO2}(\lambda)$.

6.3 Results: P. Falciparum-infected RBCs

A pilot study was conducted characterizing the morphological and spectral changes that take place when normal RBCs are infected with *P. falciparum*, an intracellular parasite responsible for the majority of the cases of malaria worldwide. A population of 35 healthy uninfected cells are imaged by QPS and are compared to a population of 42 cells that are infected with schizont-stage *P. falciparum* (section 6.2.1). As seen in Figure 6.2, the biconcave disk-shape exhibited by healthy RBCs becomes less regular after infection.

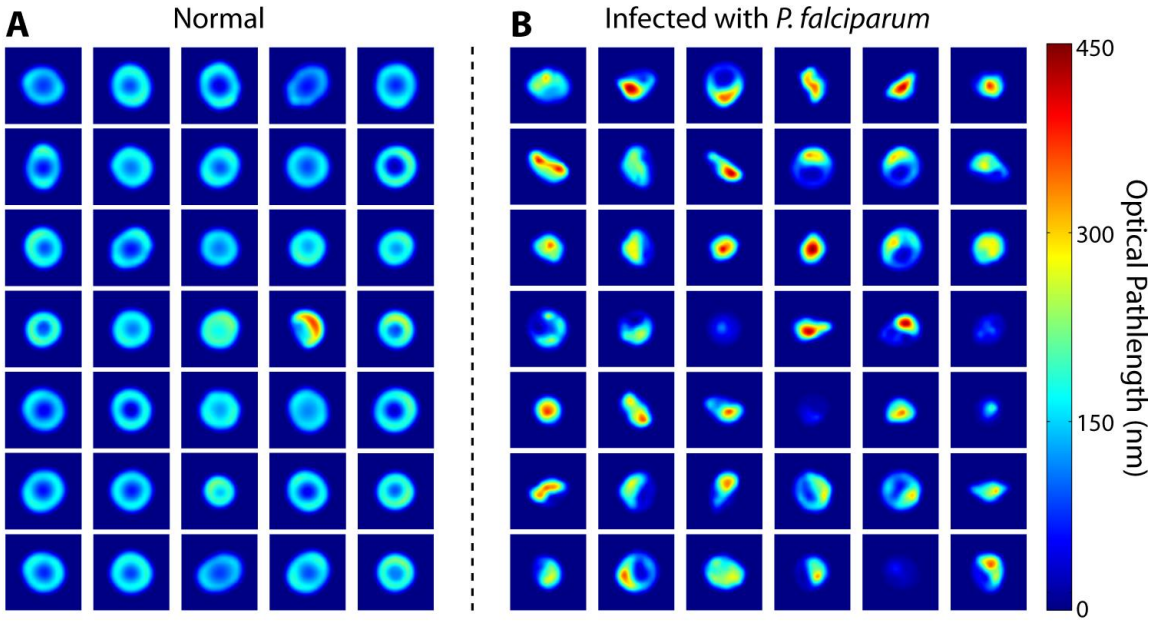

Figure 6.2: Morphological comparison of individual healthy RBCs (A) and RBCs infected with *P. falciparum* (B). Each segmented cell is shown in a 13.5 x 13.5 μm field of view.

P. falciparum grows within RBCs, consuming hemoglobin as a fuel source. The protein content of hemoglobin is consumed, leaving free heme that would otherwise be toxic both to the parasite and the RBC. To mitigate this toxicity, *P. falciparum* creates insoluble heme dimer crystals called hemozoin. In addition to the morphological changes of infected RBCs, this process reduces the total amount of hemoglobin within a cell and creates the hemozoin byproduct with its own distinct spectral features. Figure 6.3 illustrates the molar extinction coefficients and corresponding relative RI increments of oxy-hemoglobin and hemozoin as calculated by equation (6.3). Compared to Rhodamine 6G (Figure 4.8), oxy-hemoglobin is approximately half as absorptive and correspondingly has a smaller nonlinear relative RI feature, however RBCs contain a

very high concentration of HbO2 (32-36 g/dL or 5.0 – 5.6mM reference range). When hemoglobin is converted to hemozoin, the double-peak features in the 500-600nm spectral range almost disappear, and a small absorption peak appears at 650-665nm.[47] Hemozoin also lacks the large absorption feature in the Soret band (~400nm) that hemoglobin exhibits, and therefore exhibits a relative RI increment that *increases* with wavelength when calculated from the molar extinction spectrum over the range of 200-900nm.

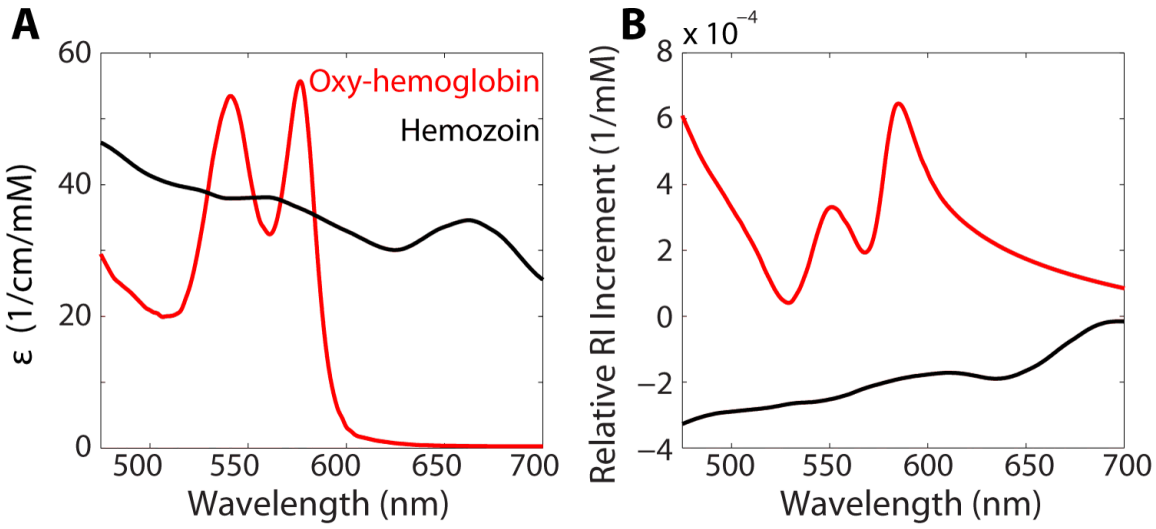

Figure 6.3: (A) Decadic molar extinction coefficients of oxy-hemoglobin[101] and *P. falciparum* by-product hemozoin[47,102]. (B) Corresponding relative RI increments calculated via the KK relations (equation (6.3)).

The OV spectrum for each cell is calculated after segmenting the RBCs from each population (Figure 6.4). Although qualitative examination of the morphological differences seen in Figure 6.2 indicates that RBCs infected with *P. falciparum* have a larger *maximum* OPL, the spectrally-averaged OV of normal RBCs was found to be

significantly higher than that of the infected cells. The cells infected with *P. falciparum* also display a wider range of total volumes, potentially indicating variation in parasite growth dynamics. Furthermore, 5 of the infected cells that were identified by automatic segmentation were identified as statistical outliers; these may be free parasites that have destroyed the RBCs or possibly cell fragments. In addition to differences in the averaged OV, Figure 6.4 also shows that the nonlinear spectral features between 520-600 nm associated with oxy-hemoglobin are present in both samples.

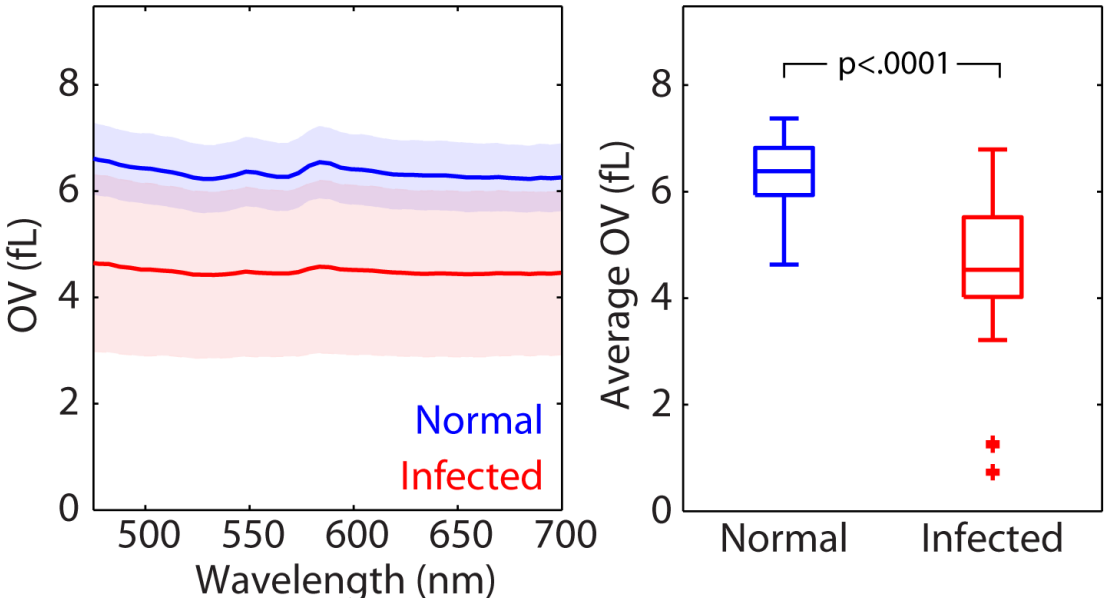

Figure 6.4: Optical volume spectra of normal and *P. falciparum*-infected RBCs. The light blue and light red ranges indicate the population standard deviation at each wavelength. Boxplots present maximum, minimum, median, and IQR ranges of each population. Crosses indicate statistical outliers.

Examining the populations' spectra more closely reveals not only a decrease in OV, but also in the average quantity of hemoglobin present. Figure 6.5 displays both the absorbance and optical volume of the normal and infected populations. The overall

absorbance increases with infection, however the characteristic hemoglobin peaks diminish significantly. The spectra are fit using non-negative linear least-squares regression to the form $A(\lambda) = C_1 + -C_2 \cdot \lambda + C_3 \cdot \varepsilon(\lambda)$ to recover mass-density concentration maps, which are then integrated over area to estimate the mass of hemoglobin contained within each cell. The normal cells are measured to contain 36.5 ± 6.3 pg (mean ± standard deviation) of oxy-hemoglobin, while the infected cells contain 15.7 ± 10.9 pg, representing a decrease in hemoglobin of 20.7 pg, or 56.8% ($p < .0001$, t-test, JMP Pro). The quantity of hemoglobin measured in normal cells is higher than laboratory reference ranges for mean cell hemoglobin (29 ± 2 pg[103], measured across $>10^6$ cells), which may be due to a systematic error.

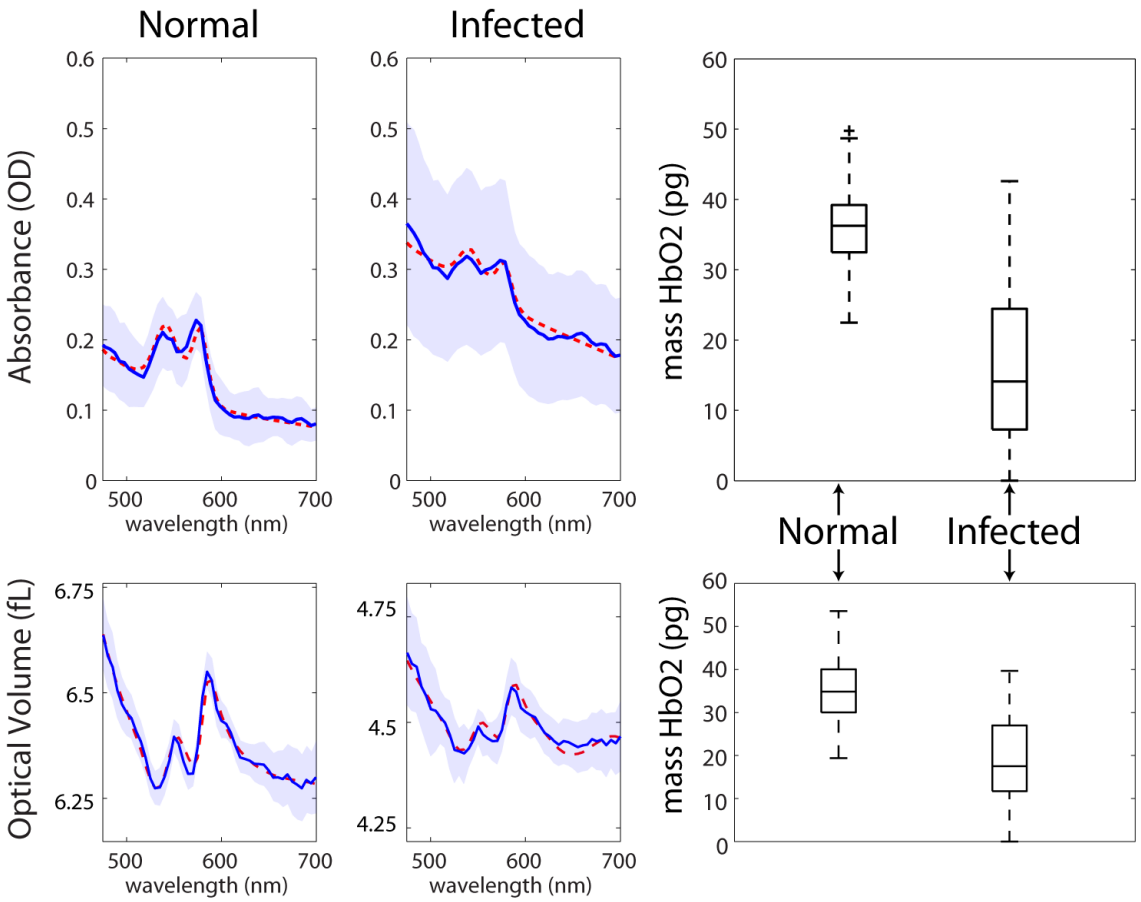

Figure 6.5: Absorbance spectra (top) and OV spectra (bottom) examining nonlinear spectral features corresponding to hemoglobin content. Boxplots of the mass of hemoglobin contained in each cell indicate maximum, minimum, median, and IQR range of hemoglobin mass, with outliers indicated with crosses. The light blue range corresponds to the standard deviation of the population.

The optical volume presented in Figure 6.5 shows decreases in the nonlinear features corresponding to oxy-hemoglobin. The light blue ranges around each OV spectrum indicate the standard deviation of the population's nonlinear OV spectra after subtracting the mean of each cell's spectral OV. As described above (section 6.2.4), the OV is fit to determine the mass of hemoglobin in each RBC using linear least squares

regression. The normal and infected populations are measured to contain 35.0 ± 8.0 pg and 18.3 ± 11.7 pg; this represents a decrease in average hemoglobin content of 16.7 pg, or 47.8% ($p < .0001$).

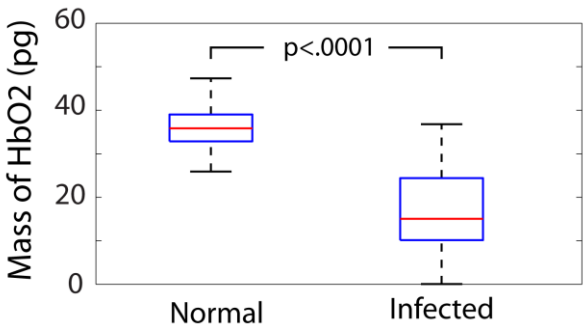

Figure 6.6: Population distributions of hemoglobin mass as determined by averaging the masses calculated from absorbance and OV for each individual cell.

In section 4.4.3, the precision of holographic concentration-determination was improved by a factor of ~2x by averaging the amplitude-based concentration measurement with the phase-based concentration measurement at each spatial location. Using a similar approach, each RBC's hemoglobin mass measurements presented in Figure 6.5 were averaged, producing the population distributions of hemoglobin content seen in Figure 6.6. The resulting mass of hemoglobin in normal cells is 35.7 ± 5.7 pg, while the mass of hemoglobin measured in infected cells is 17.0 ± 10.2 pg, with an absolute decrease of 18.7 pg (52% decrease). The measured hemoglobin masses are summarized in Table 6.1.

Table 6.1: Concentrations of HbO2 as measured by absorbance, OV, and combined

	Absorbance From Amplitude		*OV From Phase*		*Combined*	
Nominal	**Mean**	**Std**	**Mean**	**Std**	**Mean**	**Std**
Normal	36.5 pg	±6.3	35.0 pg	±8.0	35.7 pg	±5.7

Infected	15.7 pg	±10.9	18.3 pg	±11.7	17.0 pg	±10.2
Difference	20.7 pg		16.7 pg		18.7 pg	

As a final analysis, the relationship between non-spectroscopic optical volume, i.e. - averaged over the visible spectrum, and the fitted mass of hemoglobin of each cell is examined (Figure 6.7). It appears that while spectrally-averaged optical volume is correlated with the mass of hemoglobin present in the cell, hemoglobin content is only a modest predictor of cell optical volume both in normal cells as well as cells containing *P. falciparum* parasites (coefficients of determination of $r^2 = 0.39$ and 0.66 for the respective populations). Thus, both mass of hemoglobin as estimated from nonlinear spectral features and the spectrally-averaged OV provide metrics that can complement each other when characterizing cell types.

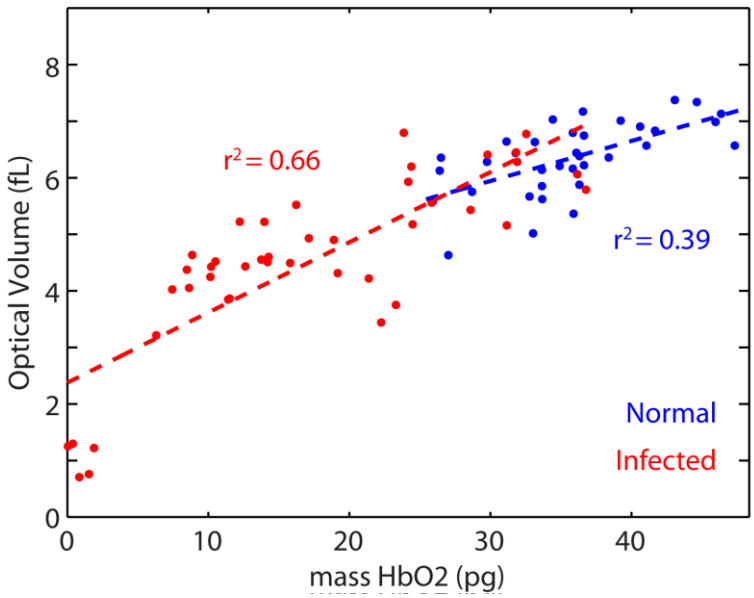

Figure 6.7: Relationship between nonspectroscopic OV and mass of hemoglobin within individual cells. Both normal and infected cells only show weak trends between the two metrics.

6.4 Discussion

Malaria is a leading cause of death worldwide, with *P. falciparum* infection being the primary causative agent. Detection of infection, determination of parasitemia (extent of infection), and estimation of the stages of parasites within their lifecycles are critical for effective diagnosis and subsequent treatment. The need for better understanding of *P. falciparum's* lifecycle and improved diagnostic techniques has motivated significant attention amongst quantitative phase imaging researchers. QPM has previously been applied to the investigation of RBCs infected by *P. falciparum* to estimate cell and parasite volumes, RIs, and mechanical properties.[49–51] However, spectroscopic changes in individual infected RBCs has not previously been investigated by QPM.

A detailed analysis has been presented which demonstrates that QPS can measure both decreases in RBC optical volume as well as decreases in hemoglobin mass associated with parasite infection. While the average mass of hemoglobin measured in normal RBCs (35.7 pg) is higher than reference ranges for mean cell hemoglobin (27-31 pg)[103], the measured decrease in hemoglobin mass of schizont-stage infected RBCs relative to healthy RBCs (52%) is in line with literature reports of hemoglobin consumption by *P. falciparum* (50-55%).[47] Our measurements further indicate that changes in non-spectroscopic OV and hemoglobin mass are only loosely correlated, suggesting that the use of RI measurements at a single wavelength to estimate hemoglobin concentration may be an unreliable method.[50]

While the measurements of hemoglobin mass and optical volume presented here both show statistically significant differences between healthy and infected RBCs, neither of these parameters or a combination of the two fully differentiates the populations. This is in part due to the variability of individual RBC volume, mass, and RI, and also in part due to the variability of metabolic activity and lifecycle stage among individual parasites. The observed differences in these populations do, however, motivate further work to develop models that incorporate both morphological and spectral features for characterizing and classifying the parasitic invasion of RBCs by *P. falciparum.*

6.5 Summary

In this chapter, a pilot study was conducted to quantify the spectral changes in RBCs infected by *P. falciparum* using QPS. Phase and amplitude spectra were processed using the methods presented in Chapters 3 & 4 to extract absorbance and optical volume spectra. These spectra were then fit to estimate hemoglobin mass differences between healthy and infected RBCs. Both hemoglobin mass and OV decreased significantly with infection, but were only loosely correlated with each other. This study indicates that spectral analysis can be useful for measuring the quantity of hemoglobin consumed through *P. falciparum* metabolism, and may be useful in distinguishing infection and parasite stage.

7 Red Blood Cell Flow Imaging

7.1 Introduction

Chapter 4 presented optical volume as a metric for quantifying microscopic objects whose exact refractive indices and physical dimensions are unknown, i.e., individual cells. A method of automated digital refocusing was also demonstrated; this technique preserves the precision of OV measurements when cells in a dynamic environment move in and out of a fixed plane of focus. This chapter presents a study that uses QPM to characterize the dynamic behavior of normal red blood cells flowing in a microchannel containing seeded endothelial cells, which make up the inner lining of blood vessels *in vivo*. Endothelialized microchannels are being developed as an *ex vivo* model of blood vessels for studying the interaction of RBCs with vessel walls. High speed QPM can complement this platform by providing a method for making quantitative measurements of individual cells with high spatial resolution and sub-millisecond temporal rates. Therefore, this chapter develops a framework for capturing and analyzing RBCs flowing through these novel microfluidic devices.

Section 7.2 describes the microfluidic platform design and construction and outlines the specific QPM imaging parameters. Next, section 7.3 presents the image processing methods used to analyze each individual RBC flowing across the field of view. A model of a single RBC is then analyzed in section 7.4.1 to provide context for

the interpretation of the experimental data acquired for 10 healthy RBCs flowing through the endothelialized microchannel (section 7.4.2).

7.2 Methods and Procedures

7.2.1 Microfluidic Device Construction

Microfluidic channels were designed to mimic the branching structure of *in vivo* capillaries.[104] First, a custom photomask with the channel features was designed and fabricated by Photosciences, Inc (Torrance, CA). Then, the positive features were photolithographically patterned onto a silicon wafer in SU-8 polymer. The thickness of the initial polymer layer determines the height of the microfluidic channels, and was varied across experiments, ranging from 6.8 μm to 30 μm. After photolithography, the patterned wafer was used to mold polydimethylsiloxane (PDMS, Sylgard 184, Dow Corning), which cured overnight at room temperature. High temperature speeds the curing process, but also causes the PDMS to develop internal stresses that deform and distort the surfaces. After the cured PDMS structure is removed from the wafer mold, inlet and outlet through-holes are cut through the PDMS with a 19-gauge needle, and the structure is covalently bonded to a glass coverslip (#2, ~0.2 mm thick) after exposure to oxygen plasma to activate the surfaces (40W, 19s, Emitech K-1050X). The PDMS bonds to the glass and makes a watertight seal capable of withstanding moderate flow pressures.

7.2.2 Endothelialized Device & RBC Preparation

The microfluidic channels used in the experiments below were seeded with human endothelial cells derived from umbilical cord blood (hCB-ECs, obtained from the Carolina Cord Blood Bank with all patient identifiers removed) using a variable-flow seeding process developed to produce an relatively uniform distribution of adherent cells along the length of the microfluidic device.[104] The endothelial cells were then cultured to create confluent layers resembling the endothelial lining of *in vivo* capillaries.

Whole human blood with normal hemoglobin (HbAA) was obtained from Duke University hospital. Blood was centrifuged to fractionate the blood serum and RBCs. The serum (n = 1.34845, Bellingham & Stanley RFM 340) was subsequently used to dilute packed RBCs to a concentration of 0.02% before flowing the cells through the endothelialized microfluidic device in order to image only ~1 cell flowing through the field of view for each dataset.

7.2.3 RBC Flow and Imaging Protocol

The microfluidic device was placed in the sample plane of the interferometer, and diluted RBCs in serum were injected into the microfluidic device using a 19-gauge syringe connected to the device by polyethylene tubing (PE60, Intramedic). The tubing formed a tight seal with the PDMS, and the device remained leak-free over flow rates ranging from 0-200 μL/min. Flow rates were set by an infusion pump (Harvard Apparatus, PHD 2000) and varied over this range to in order to adjust the transit times

of individual RBCs across the field of view (variable based on channel size). The QPS instrument was used in a static single-wavelength mode to image flowing RBCs. The center wavelength was set to λ_0 = 532nm, and images were acquired at 1000 fps with an integration time of 1 ms. For each dataset, a corresponding background phase image dataset of 100 interferograms were captured at a location containing PDMS with no microchannels or other structures; these were averaged to provide a low-noise reference phase image.

7.3 Data Analysis

Quantitative phase images are calculated from the interferograms as described in Chapter 3. The areas of each phase image not containing microchannels are manually masked and fit to a 3rd order polynomial surface, which is then subtracted from the entire phase image. Each dataset also subtracts an interferogram of the microchannel with no RBCs present to isolate the quantitative phase images of individual RBCs in each frame during flow. After isolating individual RBCs, the resulting phase images are analyzed as described below to evaluate dynamic changes taking place as the RBCs tumble and deform in response to the fluid flow.

7.3.1 Optical Volume and Intracellular Environment

As described in section 4.2, the OV of RBCs is calculated at each time point. After digital refocusing, the cell is segmented using a phase threshold of φ_{thresh} = 0.2 rad in the experiments presented here. OV changes of single RBCs during flow indicate

changes in the intracellular environment because the RI of the surrounding media within the microchannels remains constant.

7.3.2 OPL vs Surface Area

One method of characterizing dynamically moving RBCs is by plotting the average OPL vs. surface area (SA) at each time point. RBCs are not spherically symmetric, thus both of these parameters vary with orientation. However, because the product of these two parameters equals the OV, as described previously in section 4.2, an isovolumetric object remains on a characteristic curve on a plot of mean-OPL vs. SA. These plots can illustrate both orientation changes as well as OV changes over the course of an experiment.

7.4 Results

7.4.1 Simulations: Normal RBC in various orientations

Here, the OPL, SA, and OV of a simulated RBC are presented to introduce and give context to the analyses performed on measured data later in this chapter. RBC geometric thickness is first defined as a circularly-symmetric function:

$$D(r) = \sqrt{1 - \left(\frac{r}{R_0}\right)^2} \cdot \left(C_0 + C_2 \left(\frac{r}{R_0}\right)^2 + C_4 \left(\frac{r}{R_0}\right)^4 \right) \qquad (7.1)$$

where r is the radial coordinate, R_0 is the measured cell radius, and C_0, C_2, and C_4 are experimentally determined coefficients.[105] In the simulations below, the shape coefficients are taken from published data for a cell population immersed in 300 mOsm

media (approximately isotonic) with a 94 fL average volume and 7.81 μm average diameter.[105] RBCs vary widely both in size and hemoglobin content across a population. Reference ranges for mean corpuscular volume (MCV) and mean cell hemoglobin (MCH) also vary across sources, but are reported by Sarma, *et al.*, as 87 ± 7 fL (or μm^3) and 29 ± 2 pg, respectively.[103] Based on these ranges, the simulated cell described below has larger-than-average yet reasonable volume.

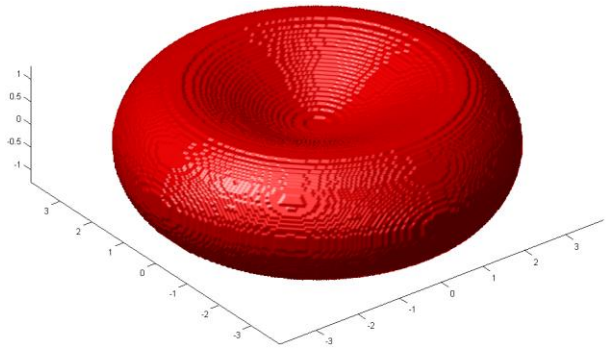

Figure 7.1: Red blood cell model. The surface is mathematically modeled by equation (7.1) to produce an object with a 91 fL volume and 7.81 μm diameter.[105] The model RBC has a homogeneous RI of 1.399.

The simulated RBC is shown laying flat in Figure 7.1. The cell model is rigidly rotated through a range of 0-90°, and thickness projections are simulated to illustrate the orientation-dependent morphology as would be measured by QPM (Figure 7.2). As the cell approaches a "standing up" geometry, two nodes appear and eventually merge to form a vertical projected profile at 90°.

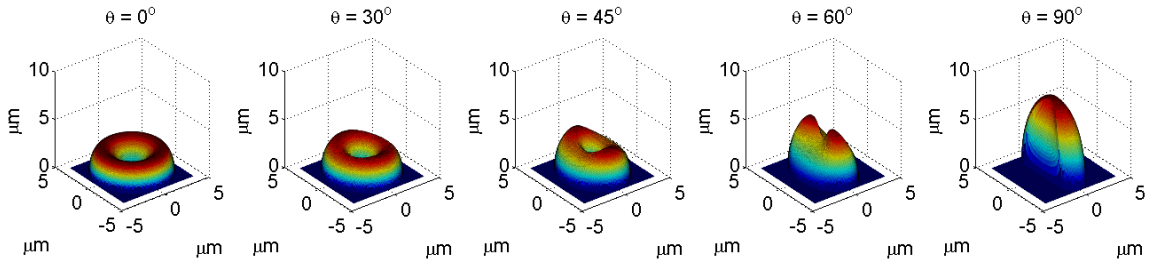

Figure 7.2: Simulated optical path length (OPL) images of the model RBC at five orientations ranging from flat (θ=0°) to standing on end (θ=90°).

Assuming an intracellular RI of 1.399[49] and a surrounding medium RI of 1.335, similar to that of 300 mOsm PBS (Δn = 0.064), the thickness profiles are converted to optical pathlength. The projected surface area of the RBC for each angle (steps of 1°) is calculated and plotted against the average OPL, producing a characteristic isovolumetric curve according to equation (4.5), $OV = \overline{\Delta OPL} * SA$ (Figure 7.3). Both increases in physical size or RI can produce a larger optical volume and shift the curve to the right, while decreases in size or RI shift the curve to the left.

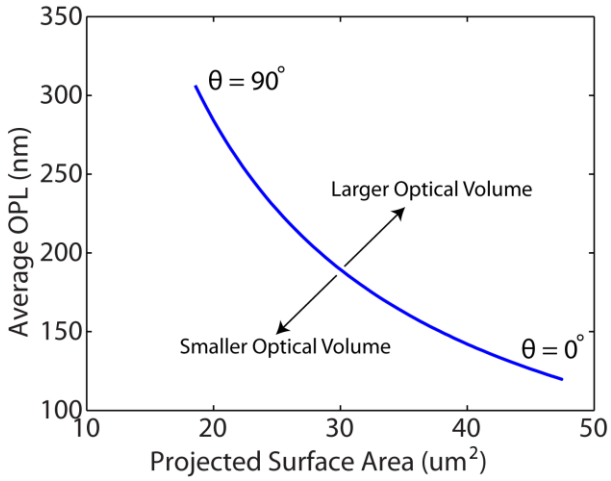

Figure 7.3 Theoretical plot of average OPL vs. projected surface area. As the cell is rotated through the orientations shown in Figure 7.2, both parameters change, however their product (OV) remains constant.

While the simulation presented above assumes a rigid RBC that maintains a classic biconcave disk shape, RBCs are dynamic objects with deformable membranes. Much of the modeling and experimental observations of RBC hydrodynamics during isotonic flow presented in literature allows membranes to deform, but assumes a consistent cell volume for analysis.[35,38–40,106,107] Under these conditions, RBCs may exceed the average OPL or projected SA range traced by the rigid RBC shown in Figure 7.3; however, a constant RI and volume will result in a constant OV measurement regardless of orientation or deformation.

7.4.2 Healthy RBCs Deforming in Microchannels

While flowing healthy RBCs through the microfluidic channels at varying rates (~1-2 mm/s), we imaged one segment of the device at which individual cells appeared to be impeded by the endothelial cells. The RBCs flow from left-to-right through the

channel pictured in Figure 7.4, first moving up the narrower 15μm-wide segment and then moving into a 15μm-wide segment. These channels were constructed with a 15μm height prior to seeding, which sets a maximum bound for the distance a flowing cell could move axially relative to the plane of focus during flow experiments. Note that although the sharp RI transitions at the edges of the channel create slight diffractive noise and a phase wrapping discontinuity between the background areas and the channel, such that the phase through the channel appears comparable to the background. In these images, the endothelial cells do not exhibit phase wrapping artifacts. According to the methods presented in section 7.2.3, the microchannel and endothelial cell structures, which do not change over time, are subtracted from each of the subsequent phase images to isolate the flowing RBCs (Figure 7.4 bottom row).

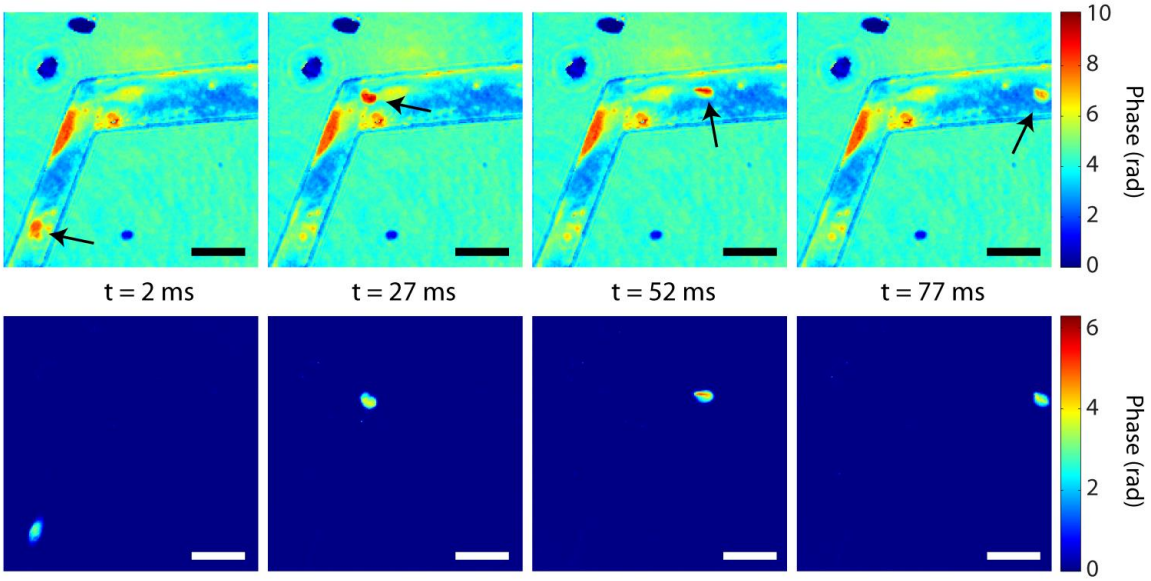

Figure 7.4: Phase images of the microchannel containing seeded endothelial cells during transit by one RBC (Top). Subtracting a phase image of the channel

before the RBC enters the field of view isolates the phase profile of the RBC at each time point. Scale bars are 20μm in length.

Ten RBCs were imaged flowing through this section of the microchannel one at a time over the course of ~21s and interferograms were captured at 1000 fps as described in Section 7.2.3. The camera software (PFV, Photron) was used to selectively save subsets of ~200 images for each cell to capture the full range of flow throughout the channel. After isolating the RBC in each frame and calculating digitally-refocused OPL images, the cells' center of mass location, projected surface area, average OPL, and OV were calculated from each frame. Figure 7.5 (A) illustrates the flow path of the same RBC pictured in Figure 7.4 superimposed on a representative phase image of the microchannel and endothelium color-coded by total distance traveled relative to the first time point. Each point corresponds to the cell's center of mass for one frame. Figure 7.5 (B) shows that over the course of 77ms, the cell travels ~120 μm (v_{avg} = 1.54 mm/s) and is delayed significantly at the elbow of the channel for approximately 15-20 ms. All 10 cells observed exhibited very similar flow paths and distances traveled, with average velocities ranging from 0.79 – 1.59 mm/s. Furthermore, all RBCs imaged were impeded at the elbow for times ranging from ~10-40 ms.

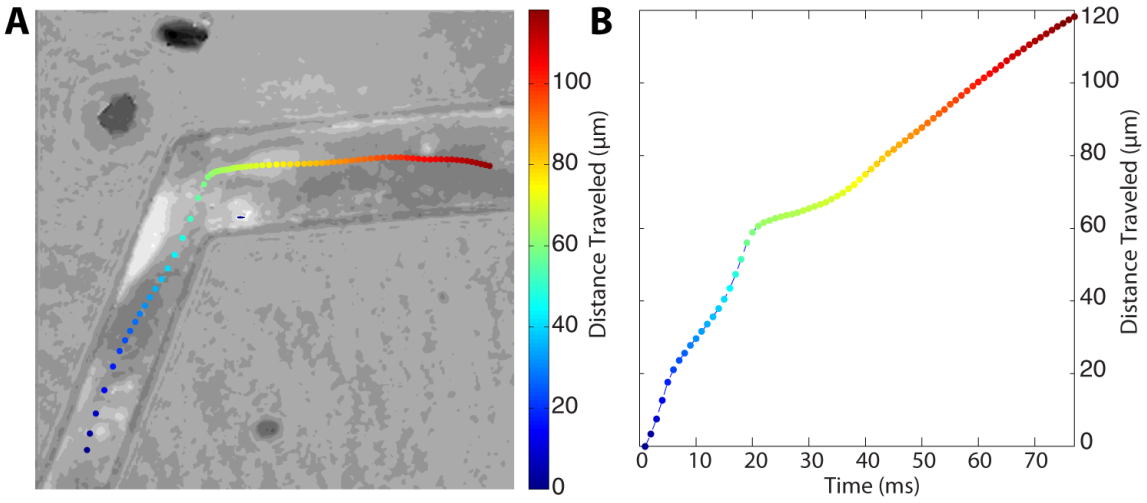

Figure 7.5: (A) Center of mass of a single RBC overlaid on top of the microchannel's phase image to illustrate the path of flow. Colorbar indicates total distance accumulated by the cell after it fully enters the field of view. (B) Total distance traveled. The slope of this line indicates velocity.

The high-speed video (Figure 7.6) of the RBC moving through the channel shows that the cell collides with an obstacle at the elbow and radically deforms before slipping around the obstacle and continuing. The cell retains a tail-like trail for a significant distance before recovering a more compact shape that is closer to the original morphology. Similar shape deformations and morphological dynamics are seen in all 10 of the RBCs imaged.

isolated_cell_s3_11.avi

Figure 7.6: Multimedia: movie of a single RBC flowing through the microchannel. (Top Left) Phase image of the microchannel and cell. (Top Right) RBC with microchannel and endothelial cells removed by phase subtraction. (Bottom Left) Surface plot of the isolate cell, centered about the center of mass. Scale bar indicates phase delay. (Bottom Right) Zoomed in phase image of the isolated RBC centered at the cell's center of mass.

Examining the OV of the single RBC shown above reveals minor fluctuations during the first 20 ms of flow followed by a progressive increase in OV of almost 25% while the cell is delayed at the elbow (Figure 7.7 (A)). Once free of this "snag" point, the OV decreases quickly to ~7 μm^3 and persists in this state until 60ms, at which point the RBC appears to undergo a rapid transition to the original OV of 6-6.5 μm^3. The corresponding average OPL vs. SA plot (Figure 7.7 (B)) also shows that the OV changes over time. This plot shows that during the first 20ms, the cell is either changing orientation via tumbling or deforming without changing volume because both the average OPL and SA vary but the OV remains approximately constant.

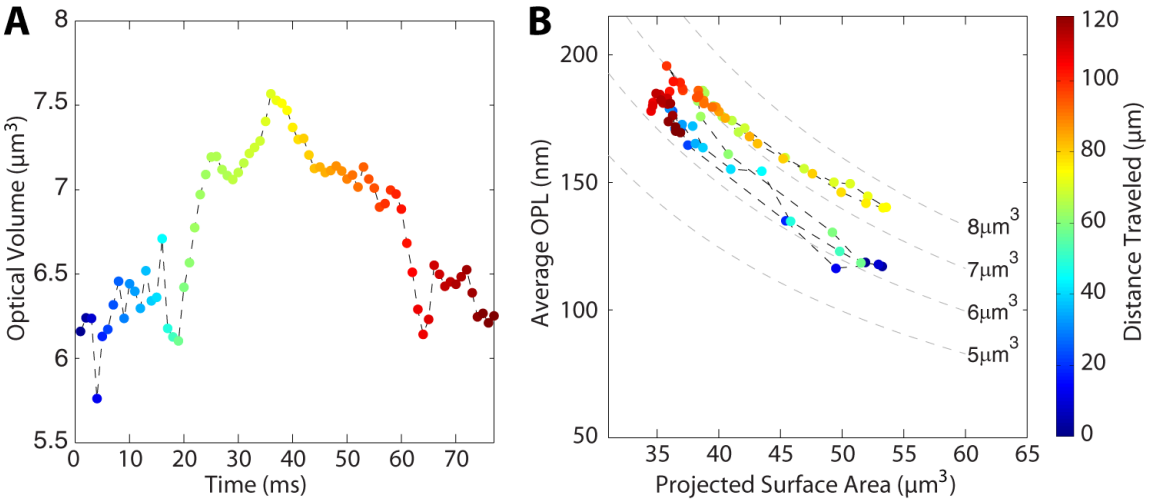

Figure 7.7: (A) Optical volume changes of one RBC flowing through the microchannel, interacting with the endothelial cells. (B) Average OPL vs. projected surface are of the RBC. Dashed lines reference lines correspond to isometric OVs. Both plots are color-coded by total distance traveled.

The dynamic increase in OV observed in this RBC is also observed in all 10 of the cells analyzed. Figure 7.8 shows the OV averaged at each distance traveled over the

population. Because each cell travels a similar distance but has significantly different transit times, averages are computed by first interpolating the volume curve across the 70-100 distance data points and then averaging. The cells are all impeded and deform at the same point in the elbow of the channel, corresponding to very similar distances traveled. Averaging at time points instead of referencing to the distance travelled along the channel would wash out the OV changes. Each RBC's distinct volume and Hb content produces a unique OV indicated by the standard deviation range shown in light blue; however, each of the cells exhibits the increase in OV at the same physical region of the channel, ~60-75μm into their flow paths. All of the cells also return to their original OVs as they return to an equilibrium morphology.

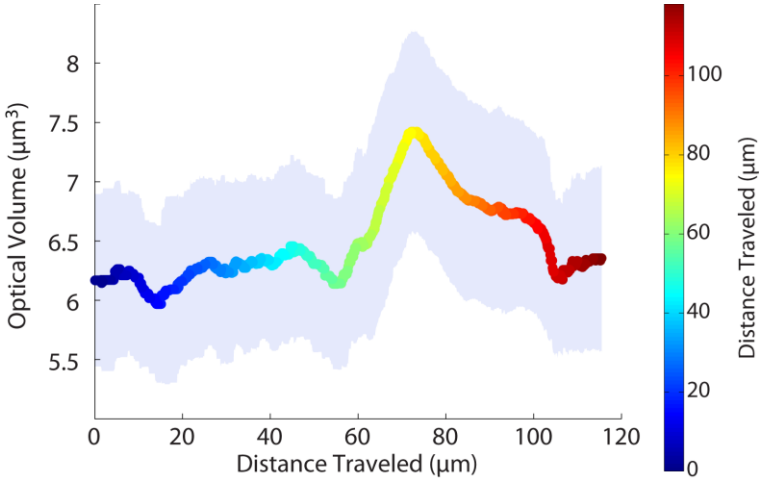

Figure 7.8: Optical volume of 10 cells averaged at each distance traveled through the channel and color-coded by total distance traveled. The blue region indicates the standard deviation of the population at each distance; the range is most due to variability in each cell's initial OV.

7.4.3 Modeling OV changes as Intracellular Water Volume Changes

RBCs are some of the most simple cells in the human body as they lack intracellular organelles and are composed primarily of a lipid bilayer membrane surrounding an aqueous solution dense with hemoglobin. The RI of an individual RBC can be modeled either as a summation of partial refractive indices[108]:

$$\overline{n_{RBC}} = n_{H2O}\frac{V_{H2O}}{V_{Total}} + n_{HbO_2}\frac{V_{HbO_2}}{V_{Total}} \tag{7.2}$$

or using the literature values of RI increments for the non-water (dry mass) components[10,12,84,109]:

$$\overline{n_{RBC}} = n_{H2O} + \alpha_{HbO_2}C_{HbO_2} + \sum_i \alpha_i C_i \tag{7.3}$$

Assuming that the RBCs are (1) dynamically changing water content in response to the surrounding environment and (2) conserving non-water mass, either equation (7.2) or (7.3) may equivalently be combined with equation (4.6) to calculate relative changes in water content from temporal changes in OV:

$$\Delta OV_{t_2-t_1} = (n_{H2O} - n_m)\cdot \Delta V_{t_2-t_1} \tag{7.4}$$

The refractive index of DI water and human serum were measured to be n_{H2O} = 1.33298 and n_m = 1.34845 using a refractometer (Bellingham & Stanley, 340 RFM), resulting in a difference of Δn = 0.01547 at λ = 589nm. Note that the RBC measurements by QPM were performed at λ_0 = 532nm, so a slight error in Δn may be present. Using equation (7.4), the relative OV changes for each of the 10 RBCs were calculated,

referenced to the initial volume, and averaged (Figure 7.9). The cells appear to lose up to 78.42 fL of water volume while deforming and squeezing past the obstacle seen above. If the average cell volume is taken to be 94 fL[105], then this indicates the cells lose enough water to account for an average 83% volume change in these experiments.

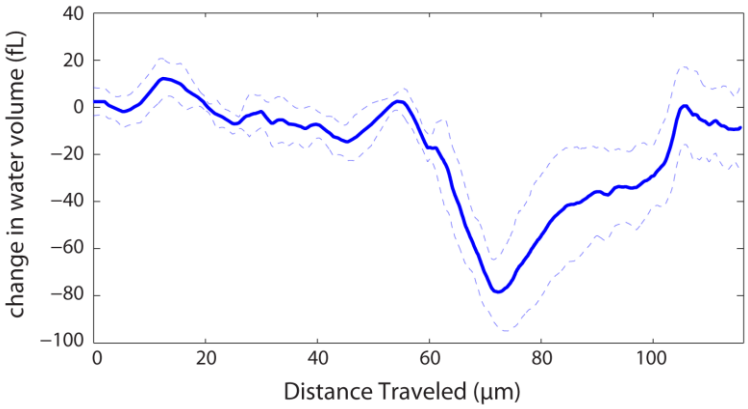

Figure 7.9: Calculated changes in RBC water volume, assuming that non-water cell components are conserved and maintain a constant RI contribution by equation (7.2) or (7.3). Solid blue line indicates the average change in water volume across the 10 cells, dotted lines indicate standard deviations of the population.

7.5 Discussion

The dynamic changes in OV observed in these experiments are modeled as changes in intracellular water volume in section 7.4.3. This model assumes that the dry mass of the RBC is conserved during transit through the channel, and that the RI increment of all dry mass components remain constant. I hypothesize that the cell loses water upon collision and absorbs water from its environment to reestablish equilibrium, which seems to be reasonably supported by the data in Figure 7.9. Because the RI of water is less than that of serum, a decrease of water would increase OV and an increase

of water would decrease OV, which qualitatively matches the experimental observations. Other sources for the observed trends would be to consider that the cell is damaged and loses mass: however, this phenomenon would result in a decrease in OV as the RI increment of proteins is higher than the surrounding serum media, and would result in an irreversible change in the cell's OV.

To consider other sources of the observed change, one must acknowledge that an RBC's volume is not comprised solely of water, but also contains a significant volume of hemoglobin. Using the measured apparent partial volume of hemoglobin from DeMoll, *et al.*,[110] as 0.7505 fL/pg and the average hemoglobin content of RBCs as 29 pg [103], an average healthy RBC should contain 21.76 fL of hemoglobin volume, leaving only 72.24 fL of water. Without taking into account the contributions of cytosolic ions and additional non-hemoglobin proteins (approximately 2.5% of the RBC mass[11]), the RBCs that were measured here would have to contain more water than the literature-described average RBCs and would have to lose practically all of it. Therefore, while water loss may account for some of the changes in OV observed here, there appear to be additional mechanisms that cause the peak OV changes. These mechanisms may include changes to the constitutive cell materials (hemoglobin, proteins, water), potentially caused by compression due to mechanical forces, or nonlinear concentration-dependences of the RIs of these materials that appear with high local concentrations.

The experiments here suggest that RBCs as seen here may exhibit substantial volumetric changes in response to flow and mechanical stresses, however much of the literature that models or experimentally characterizes RBC flow dynamics assumes a constant cell volume.[35,38–40,106,107] This discrepancy points to the need for future studies of individual RBCs by QPM to elucidate the relationship between mechanical stimuli and the resulting volumetric changes.

7.6 Summary

In this chapter, high-speed QPM was applied to imaging RBCs flowing in endothelialized microchannels. These microchannels mimic the network structures seen for *in vivo* vasculature and have branches with cross-sections as small as 15x15 μm^2. Furthermore, the channels are seeded with endothelial cells, which are then cultured into continuous linings to simulate capillaries. These microchannels provide an elegant *ex vivo* model for studying the interactions of flowing cells with the walls of blood vessels.

High-speed QPM allows quantitative label-free measurement both of the microchannel and endothelial environment as well as the dynamic cells traversing the field of view with millisecond resolution, making the system well-suited for imaging these devices at physiological flow rates.[104] In this chapter, a model of a single RBC was constructed to illustrate the relationship between average OPL, projected surface area, and OV and to provide context to the experimental data. A set of 10 healthy RBCs were

then imaged flowing through the smallest microchannels at velocities up to 1.59 mm/s while interacting with the endothelial cells. The image analysis enabled by QPM demonstrates dynamic changes in both the morphology and OV of these RBCs in response to these interactions. An attempt to model the OV changes as water volume regulation indicated that the physical mechanism underlying the measured dynamics is not solely due to water loss as originally hypothesized. Instead, these results underscore the need for future studies to characterize how the intracellular environment of RBCs changes in response to mechanical deformations, and how these responses vary with disease pathology.

8 Conclusions and Future Directions

The work presented in this dissertation chronicled the development of instrumentation and image processing methods for high-resolution off-axis quantitative phase microscopy and its extension as a hyperspectral holographic imaging technique, quantitative phase spectroscopy (QPS). Three novel applications studying the dynamics and spectral features of semitransparent objects were then presented, demonstrating that the QPS and time-resolved QPM instruments and data analysis techniques developed here can provide insight to the physics of biological samples.

The off-axis QPM system design and image processing methods were described in Chapter 3. The system captures interferograms, which are processed to yield quantitative phase images with high resolution. Accurate time-resolved 2-dimensional maps of sample optical path lengths (OPLs) were obtained through phase unwrapping algorithms and subtraction of a background phase imagery.

After describing the QPM system and phase image conditioning methods, the development of QPS is outlined. The addition of a filtered supercontinuum light source with finite illumination bandwidth requires path-matching of the interferometer arms and produces a coherence "envelope" on the off-axis interference fringe. Sweeping the center wavelength across the visible range also produces field of view and focal shifts, which must be digitally corrected. The chapter finally presents a detailed characterization of the temporal and spatial noise of the QPS system and analyzes the

noise reduction achieved by averaging frames. The final QPS system achieves sub-nanometer spatio-temporal sensitivity.

Chapter 4 presented several novel methods of analyzing the quantitative phase information produced by the QPM and QPS systems. Optical volume (OV) was presented as a novel metric for evaluating microscopic objects whose height profiles cannot be separated from their RIs, and the impact of defocus on accurate OV measurements was studied experimentally using microspheres with known sizes as well as individual RBCs, whose RI and thicknesses are not well-characterized. Because these instruments recover the complex amplitude and phase of the light transmitted through the sample, the images can be digitally-refocused after recording to significantly improve the accuracy of RI and OV measurements. After demonstrating noise-reduction in phase images by spectrally-averaging multiple measurements obtained by QPS, the methods of extracting spectral dispersion and molecular content characterization were discussed. A glass microchannel system was used to measure the concentrations of rhodamine 6G (R6G). These associated analyses demonstrated that holographic phase and amplitude can each be used to independently assess concentration with approximately equivalent sensitivity, and may be further combined to improve the precision of concentration measurements at each spatial point across the field of view.

Using the QPM instrument presented in Chapter 3, a study of dynamically-hydrating microbicidal films with varying thicknesses and compositions was presented in Chapter 5. The dissolution kinetics of the polymer material of these films has an impact on drug delivery kinetics, and the spatiotemporal behavior of the polymer vehicle has not been quantitatively studied outside of the experiments presented here. Film thickness was found to slow the rate of hydration, while thickness and composition were found to affect both the microscopic and macroscopic spatiotemporal dissolution kinetics. These results can be used in conjunction with mathematical models of film hydration and distintegration[32] to improve the understanding of polymer vehicle behavior and its impact on efficient topical drug delivery.

Chapter 6 presents a study that employed QPS to investigate the spectroscopic optical volume (OV) changes in RBCs infected with *P. falciparum* that are associated with intracellular biomolecular changes. The absorbance and phase spectra of a population of RBCs infected with schizont-stage *P. falciparum* parasites both indicated a decrease in hemoglobin quantity. A similar decrease in the spectrally-averaged OV was seen, but only loosely correlated with hemoglobin decrease on a cell-by-cell basis. This weak correlation suggests that while the conversion of hemoglobin to hemozoin has an impact on OV, there may be additional changes in protein composition or density that account for the remaining variation in OV. Two- and three-dimensional single-wavelength RI maps of RBCs infected by *P. falciparum* have previously been used to estimate parasite

volume and hemoglobin content; however, QPS adds the spectral dimension of information and opens the door for spectroscopic composition determination. These results motivate further investigations of spectral OV and more detailed models of intracellular RI to better characterize the biophysical changes that take place within RBCs during infection. It is also important to realize that these morphological and spectroscopic features change during parasite growth; therefore, a larger study has been planned to compare holographic morphology and spectroscopy of *P. falciparum* at multiple stages in its lifecycle. Results of this future study may provide insight into the underlying biophysical interaction of *P. falciparum* with RBCs, and also may yield metrics that can be used to develop automated identification and classification of disease stage.

Chapter 7 presented a study that used QPM to characterize the dynamic behavior of normal red blood cells flowing in a microchannel containing seeded endothelial cells, which make up the inner lining of blood vessels *in vivo*. A sample of 10 RBCs traversing the microchannel all exhibited high-speed deformations in response to mechanical forces that were captured with millisecond resolution by QPM. Unlike previous studies that have examined the deformability and morphology of RBCs under mechanical stresses using intensity-based microscopy[38,41], QPM enabled digitally-refocused OV measurements that indicate large changes in the cells' coupled RI and volume. Initial modeling of these observations as water volume changes indicated that

the physical mechanism underlying the measured dynamics is not as straightforward as originally hypothesized. Instead, these results underscore the need for future studies to characterize how the intracellular environment of RBCs changes in response to mechanical deformations, and how these responses vary with disease pathology.

References

1. Gabor, D. A New Microscopic Principle. *Nature* **161,** 777–778 (1948).

2. Zhang, T. & Yamaguchi, I. Three-dimensional microscopy with phase-shifting digital holography. *Opt. Lett.* **23,** 1221 (1998).

3. Goodman, J. W. *Introduction to Fourier optics*. (Roberts & Co., 2005).

4. Popescu, G. *et al.* Fourier phase microscopy for investigation of biological structures and dynamics. *Opt. Lett.* **29,** 2503 (2004).

5. Iwai, H. *et al.* Quantitative phase imaging using actively stabilized phase-shifting low-coherence interferometry. *Opt. Lett.* **29,** 2399 (2004).

6. Wang, Z. *et al.* Spatial light interference microscopy (SLIM). *Opt. Express* **19,** 1016 (2011).

7. Cuche, E., Marquet, P. & Depeursinge, C. Simultaneous amplitude-contrast and quantitative phase-contrast microscopy by numerical reconstruction of Fresnel off-axis holograms. *Appl. Opt.* **38,** 6994 (1999).

8. Ikeda, T., Popescu, G., Dasari, R. R. & Feld, M. S. Hilbert phase microscopy for investigating fast dynamics in transparent systems. *Opt. Lett.* **30,** 1165 (2005).

9. Popescu, G., Ikeda, T., Dasari, R. R. & Feld, M. S. Diffraction phase microscopy for quantifying cell structure and dynamics. *Opt. Lett.* **31,** 775 (2006).

10. Park, Y., Yamauchi, T., Choi, W., Dasari, R. & Feld, M. S. Spectroscopic phase microscopy for quantifying hemoglobin concentrations in intact red blood cells. *Opt. Lett.* **34,** 3668–3670 (2009).

11. Lichtman, M. A. & Williams, W. J. *Williams hematology*. (McGraw-Hill, Medical Pub. Division, 2006).

12. Jang, Y., Jang, J. & Park, Y. Dynamic spectroscopic phase microscopy for quantifying hemoglobin concentration and dynamic membrane fluctuation in red blood cells. *Opt. Express* **20,** 9673 (2012).

13. Fu, D. *et al.* Quantitative dispersion microscopy. *Biomed. Opt. Express* **1,** 347–353 (2010).

14. Robles, F. E., Satterwhite, L. L. & Wax, A. Nonlinear phase dispersion spectroscopy. *Opt. Lett.* **36,** 4665–4667 (2011).

15. Choma, M. A., Ellerbee, A. K., Yang, C., Creazzo, T. L. & Izatt, J. A. Spectral-domain phase microscopy. *Opt. Lett.* **30,** 1162 (2005).

16. Ahrenkiel, R. K. Modified Kramers-Kronig analysis of optical spectra. *J. Opt. Soc. Am.* **61,** 1651–1655 (1971).

17. Rinehart, M., Zhu, Y. & Wax, A. Quantitative phase spectroscopy. *Biomed. Opt. Express* **3,** 958 (2012).

18. Jung, J.-H., Jang, J. & Park, Y. Spectro-refractometry of Individual Microscopic Objects Using Swept-Source Quantitative Phase Imaging. *Anal. Chem.* **85,** 10519–10525 (2013).

19. Mann, C. J., Bingham, P. R., Lin, H. K., Paquit, V. C. & Gleason, S. S. Dual modality live cell imaging with multiple-wavelength digital holography and epi-fluorescence. *3D Res.* **2,** 1–6 (2010).

20. Miller-Chou, B. A. & Koenig, J. L. A review of polymer dissolution. *Prog. Polym. Sci.* **28,** 1223–1270 (2003).

21. Kolin, D. L., Ronis, D. & Wiseman, P. W. k-Space Image Correlation Spectroscopy: A Method for Accurate Transport Measurements Independent of Fluorophore Photophysics. *Biophys. J.* **91,** 3061–3075 (2006).

22. Lee, P. I. & Peppas, N. A. Prediction of polymer dissolution in swellable controlled-release systems. *J. Controlled Release* **6,** 207–215 (1987).

23. Stone, A. & Harrison, P. F. *Microbicides: Ways Forward*. (Alliance for Microbicide Development, Silver Spring, MD, 2010).

24. Abdool Karim, Q. *et al.* Effectiveness and Safety of Tenofovir Gel, an Antiretroviral Microbicide, for the Prevention of HIV Infection in Women. *Science* **329,** 1168–1174 (2010).

25. National Institute of Allergy and Infectious Diseases (NIAID) & Microbicide Trials Network. *Safety and Effectiveness of Tenofovir 1% Gel, Tenofovir Disproxil Fumarate, and Emtricitabine/Tenofovir Disoproxil Fumarate Tablets in Preventing HIV in Women*.

26. Garg, S. *et al.* Advances in development, scale-up and manufacturing of microbicide gels, films, and tablets. *Antiviral Res.* **88,** S19–S29 (2010).

27. Garg, S. *et al.* Development and characterization of bioadhesive vaginal films of sodium polystyrene sulfonate (PSS), a novel contraceptive antimicrobial agent. *Pharm. Res.* **22,** 584–595 (2005).

28. Geonnotti, A. R. & Katz, D. F. Dynamics of HIV Neutralization by a Microbicide Formulation Layer: Biophysical Fundamentals and Transport Theory. *Biophys. J.* **91,** 2121–2130 (2006).

29. Katz, D. F., Gao, Y. & Kang, M. Using modeling to help understand vaginal microbicide functionality and create better products. *Drug Deliv. Transl. Res.* **1,** 256–276 (2011).

30. Akil, A. *et al.* Development and characterization of a vaginal film containing dapivirine, a non-nucleoside reverse transcriptase inhibitor (NNRTI), for prevention of HIV-1 sexual transmission. *Drug Deliv. Transl. Res.* **1,** 209–222 (2011).

31. Ham, A. S. *et al.* Vaginal Film Drug Delivery of the Pyrimidinedione IQP-0528 for the Prevention of HIV Infection. *Pharm. Res.* **29,** 1897–1907 (2012).

32. Tasoglu, S., Rohan, L. C., Katz, D. F. & Szeri, A. J. Transient swelling, spreading, and drug delivery by a dissolved anti-HIV microbicide-bearing film. *Phys. Fluids* **25,** 031901 (2013).

33. Rinehart, M. T. *et al.* Time-resolved imaging refractometry of microbicidal films using quantitative phase microscopy. *J. Biomed. Opt.* **16,** 120510 (2011).

34. Mohandas, N. & Evans, E. Mechanical properties of the red cell membrane in relation to molecular structure and genetic defects. *Annu. Rev. Biophys. Biomol. Struct.* **23,** 787–818 (1994).

35. Hochmuth, R. M. & Marcus, W. D. Membrane Tethers Formed from Blood Cells with Available Area and Determination of Their Adhesion Energy. *Biophys. J.* **82,** 2964–2969 (2002).

36. Yedgar, S., Koshkaryev, A. & Barshtein, G. The red blood cell in vascular occlusion. *Pathophysiol. Haemost. Thromb.* **32,** 263–268 (2002).

37. Fischer, T. M. Shape Memory of Human Red Blood Cells. *Biophys. J.* **86,** 3304–3313 (2004).

38. Dupire, J., Socol, M. & Viallat, A. Full dynamics of a red blood cell in shear flow. *Proc. Natl. Acad. Sci.* **109,** 20808–20813 (2012).

39. Pivkin, I. & Karniadakis, G. Accurate Coarse-Grained Modeling of Red Blood Cells. *Phys. Rev. Lett.* **101,** (2008).

40. Peng, Z. *et al.* Lipid bilayer and cytoskeletal interactions in a red blood cell. *Proc. Natl. Acad. Sci.* **110,** 13356–13361 (2013).

41. Quinn, D. J. *et al.* Combined Simulation and Experimental Study of Large Deformation of Red Blood Cells in Microfluidic Systems. *Ann. Biomed. Eng.* **39,** 1041–1050 (2011).

42. Popescu, G., Park, Y., Dasari, R., Badizadegan, K. & Feld, M. Coherence properties of red blood cell membrane motions. *Phys. Rev. E* **76,** (2007).

43. Park, Y. *et al.* Measurement of red blood cell mechanics during morphological changes. *Proc. Natl. Acad. Sci.* **107,** 6731–6736 (2010).

44. Park, Y. *et al.* Measurement of the nonlinear elasticity of red blood cell membranes. *Phys. Rev. E* **83,** (2011).

45. Wang, R., Ding, H., Mir, M., Tangella, K. & Popescu, G. Effective 3D viscoelasticity of red blood cells measured by diffraction phase microscopy. *Biomed. Opt. Express* **2,** 485 (2011).

46. World Health Organization, Tuschman, M., World Health Organization & Global Malaria Programme. *World malaria report 2013*. (2013).

47. Orjih, A. U. & Fitch, C. D. Hemozoin production by Plasmodium falciparum: variation with strain and exposure to chloroquine. *Biochim. Biophys. Acta BBA - Gen. Subj.* **1157,** 270–274 (1993).

48. Hosseini, S. M. & Feng, J. J. How Malaria Parasites Reduce the Deformability of Infected Red Blood Cells. *Biophys. J.* **103,** 1–10 (2012).

49. Park, Y. *et al.* Refractive index maps and membrane dynamics of human red blood cells parasitized by Plasmodium falciparum. *Proc. Natl. Acad. Sci.* **105,** 13730–13735 (2008).

50. Kim, K. *et al.* High-resolution three-dimensional imaging of red blood cells parasitized by *Plasmodium falciparum* and *in situ* hemozoin crystals using optical diffraction tomography. *J. Biomed. Opt.* **19,** 011005 (2013).

51. Chandramohanadas, R. *et al.* Biophysics of Malarial Parasite Exit from Infected Erythrocytes. *PLoS ONE* **6,** e20869 (2011).

52. Ghiglia, D. & Pritt, M. *Two dimensional phase unwrapping: theory,algorithms & software*. (Wiley Interscience, 1998).

53. Schofield, M. A. & Zhu, Y. Fast phase unwrapping algorithm for interferometric applications. *Opt. Lett.* **28,** 1194 (2003).

54. Huntley, J. M. Noise-immune phase unwrapping algorithm. *Appl. Opt.* **28,** 3268 (1989).

55. Flynn, T. J. Two-dimensional phase unwrapping with minimum weighted discontinuity. *J. Opt. Soc. Am. A* **14,** 2692 (1997).

56. Huntley, J. M. & Saldner, H. Temporal phase-unwrapping algorithm for automated interferogram analysis. *Appl. Opt.* **32,** 3047 (1993).

57. Hendargo, H. C., Zhao, M., Shepherd, N. & Izatt, J. A. Synthetic wavelength based phase unwrapping in spectral domain optical coherence tomography. *Opt. Express* **17,** 5039 (2009).

58. Cheng, Y.-Y. & Wyant, J. C. Two-wavelength phase shifting interferometry. *Appl. Opt.* **23,** 4539 (1984).

59. Onodera, R. & Ishii, Y. Two-Wavelength Interferometry That Uses a Fourier-Transform Method. *Appl. Opt.* **37,** 7988 (1998).

60. Mann, C. J., Bingham, P. R., Paquit, V. C. & Tobin, K. W. Quantitative phase imaging by three-wavelength digital holography. *Opt. Express* **16,** 9753 (2008).

61. Gass, J., Dakoff, A. & Kim, M. K. Phase imaging without 2π ambiguity by multiwavelength digital holography. *Opt. Lett.* **28,** 1141 (2003).

62. Parshall, D. & Kim, M. K. Digital holographic microscopy with dual-wavelength phase unwrapping. *Appl. Opt.* **45,** 451 (2006).

63. Rinehart, M. T., Shaked, N. T., Jenness, N. J., Clark, R. L. & Wax, A. Simultaneous two-wavelength transmission quantitative phase microscopy with a color camera. *Opt. Lett.* **35,** 2612–2614 (2010).

64. Kühn, J. *et al.* Real-time dual-wavelength digital holographic microscopy with a single hologram acquisition. *Opt. Express* **15,** 7231 (2007).

65. Khmaladze, A., Kim, M. & Lo, C.-M. Phase imaging of cells by simultaneous dual-wavelength reflection digital holography. *Opt. Express* **16,** 10900 (2008).

66. Fu, Y., Pedrini, G., Hennelly, B. M., Groves, R. M. & Osten, W. Dual-wavelength image-plane digital holography for dynamic measurement. *Opt. Lasers Eng.* **47,** 552–557 (2009).

67. Reed Teague, M. Deterministic phase retrieval: a Green's function solution. *J. Opt. Soc. Am.* **73,** 1434 (1983).

68. Barty, A., Nugent, K. A., Paganin, D. & Roberts, A. Quantitative optical phase microscopy. *Opt. Lett.* **23,** 817 (1998).

69. Hitzenberger, C. K., Sticker, M., Leitgeb, R. & Fercher, A. F. Differential phase measurements in low-coherence interferometry without 2π ambiguity. *Opt. Lett.* **26,** 1864 (2001).

70. Zhang, J., Rao, B., Yu, L. & Chen, Z. High-dynamic-range quantitative phase imaging with spectral domain phase microscopy. *Opt. Lett.* **34,** 3442 (2009).

71. Jenness, N. J., Hill, R. T., Hucknall, A., Chilkoti, A. & Clark, R. L. A versatile diffractive maskless lithography for single-shot and serial microfabrication. *Opt. Express* **18,** 11754 (2010).

72. Picart, P., Mounier, D. & Desse, J. M. High-resolution digital two-color holographic metrology. *Opt. Lett.* **33,** 276 (2008).

73. Shaked, N. T., Zhu, Y., Rinehart, M. T. & Wax, A. Two-step-only phase-shifting interferometry with optimized detector bandwidth for microscopy of live cells. *Opt. Express* **17,** 15585–15591 (2009).

74. Choma, M. A., Ellerbee, A. K., Yazdanfar, S. & Izatt, J. A. Doppler flow imaging of cytoplasmic streaming using spectral domain phase microscopy. *J. Biomed. Opt.* **11,** 024014 (2006).

75. Monemhaghdoust, Z., Montfort, F., Emery, Y., Depeursinge, C. & Moser, C. Dual wavelength full field imaging in low coherence digital holographic microscopy. *Opt. Express* **19,** 24005–24022 (2011).

76. Yaqoob, Z. *et al.* Single-shot full-field reflection phase microscopy. *Opt. Express* **19,** 7587–7595 (2011).

77. Liebling, M. & Unser, M. Autofocus for digital Fresnel holograms by use of a Fresnelet-sparsity criterion. *J. Opt. Soc. Am. A* **21,** 2424 (2004).

78. Dubois, F., Schockaert, C., Callens, N. & Yourassowsky, C. Focus plane detection criteria in digital holography microscopy by amplitude analysis. *Opt. Express* **14,** 5895 (2006).

79. Langehanenberg, P., Kemper, B., Dirksen, D. & von Bally, G. Autofocusing in digital holographic phase contrast microscopy on pure phase objects for live cell imaging. *Appl. Opt.* **47,** D176 (2008).

80. Xu, L., Mater, M. & Ni, J. Focus detection criterion for refocusing in multi-wavelength digital holography. *Opt. Express* **19,** 14779–14793 (2011).

81. Barer, R. Interference Microscopy and Mass Determination. *Nature* **169,** 366–367 (1952).

82. Davies, H. G., Wilkins, M. H. F., Chayen, J. & La Cour, L. F. The Use of the Interference Microscope to Determine Dry Mass in Living Cells and as a Quantitative Cytochemical Method. *Q. J. Microsc. Sci.* **S3,** 271–304 (1954).

83. Davies, H. G. & Wilkins, M. H. F. Interference Microscopy and Mass Determination. *Nature* **169,** 541–541 (1952).

84. Barer, R. & Tkaczyk, S. Refractive Index of Concentrated Protein Solutions. *Nature* **173,** 821–822 (1954).

85. Heller, W. Remarks on Refractive Index Mixture Rules. *J. Phys. Chem.* **69,** 1123–1129 (1965).

86. Born, M. & Wolf, E. *Principles of optics: electromagnetic theory of propagation, interference and diffraction of light*. (Cambridge University Press, 1999).

87. X3550CH.3 Example Chip Drawing. (2008). at <http://www.micronit.com/wp-content/uploads/2014/08/X3550CH.3-R1.1.pdf>

88. Datasheet: D 263® M – Glass for Microscopy Cover Slips. (2013). at <http://www.us.schott.com/advanced_optics/english/syn/advanced_optics/products/optical-materials/thin-glass/cover-glass-d-263-m/index.html>

89. Daimon, M. & Masumura, A. Measurement of the refractive index of distilled water from the near-infrared region to the ultraviolet region. *Appl. Opt.* **46,** 3811 (2007).

90. Prahl, S. *Rhodamine 6G*. (2012). at <http://omlc.org/spectra/PhotochemCAD/html/083.html>

91. Rinehart, M., Grab, S., Rohan, L., Katz, D. & Wax, A. Analysis of Vaginal Microbicide Film Hydration Kinetics by Quantitative Imaging Refractometry. *PLoS ONE* **9,** e95005 (2014).

92. Tsay, T. T. & Jacobson, K. A. Spatial Fourier analysis of video photobleaching measurements. Principles and optimization. *Biophys. J.* **60,** 360–368 (1991).

93. Berk, D. A., Yuan, F., Leunig, M. & Jain, R. K. Fluorescence photobleaching with spatial Fourier analysis: measurement of diffusion in light-scattering media. *Biophys. J.* **65,** 2428–2436 (1993).

94. Popescu, G. *et al.* Optical imaging of cell mass and growth dynamics. *AJP Cell Physiol.* **295,** C538–C544 (2008).

95. Bray, R. S. & Garnham, P. C. The life-cycle of primate malaria parasites. *Br. Med. Bull.* **38,** 117–122 (1982).

96. Phillips, A., Gerald Shaper, A. & Whincup, P. ASSOCIATION BETWEEN SERUM ALBUMIN AND MORTALITY FROM CARDIOVASCULAR DISEASE, CANCER, AND OTHER CAUSES. *The Lancet* **334,** 1434–1436 (1989).

97. Sydoruk, O., Zhernovaya, O., Tuchin, V. & Douplik, A. Refractive index of solutions of human hemoglobin from the near-infrared to the ultraviolet range: Kramers-Kronig analysis. *J. Biomed. Opt.* **17,** 115002 (2012).

98. Faber, D. *et al.* Oxygen Saturation-Dependent Absorption and Scattering of Blood. *Phys. Rev. Lett.* **93,** (2004).

99. Lucarini, V., Peiponen, K.-E., Saarinen, J. J. & Vartiainen, E. M. *Kramers-Kronig Relations in Optical Materials Research*. (Springer-Verlag Berlin Heidelberg, 2005).

100. Bachrach, R. & Brown, F. Exciton-Optical Properties of TlBr and TlCl. *Phys. Rev. B* **1,** 818–831 (1970).

101. Prahl, S. *Optical Absorption of Hemoglobin*. (Oregon Medical Laser Center, 1999). at <http://omlc.org/spectra/hemoglobin/index.html>

102. Phong, V.-T. *Novel Optical Detection of Synthesized Hemozoin Crystals for Malaria Diagnosis*. (University of Delaware). at <http://web.mit.edu/vophong/www/Hemozoin%20Detection.htm>

103. Sarma, P. R. in *Clinical Methods: The History, Physical, and Laboratory Examinations* (eds. Walker, H. K., Hall, W. D. & Hurst, J. W.) (Butterworths, 1990). at <http://www.ncbi.nlm.nih.gov/books/NBK260/>

104. Zhao, K. Optimization of Conditions for Endothelial Seeding of Microfluidic Devices with Long Branching Networks and Small Channel Dimensions. (Duke University, 2013). at <http://hdl.handle.net/10161/8274>

105. Evans, E. & Fung, Y.-C. Improved measurements of the erythrocyte geometry. *Microvasc. Res.* **4,** 335–347 (1972).

106. Fedosov, D. A., Dao, M., Karniadakis, G. E. & Suresh, S. Computational Biorheology of Human Blood Flow in Health and Disease. *Ann. Biomed. Eng.* **42,** 368–387 (2014).

107. Hochmuth, R. M. Micropipette aspiration of living cells. *J. Biomech.* **33,** 15–22 (2000).

108. Casassa, E. F. & Eisenberg, H. PARTIAL SPECIFIC VOLUMES AND REFRACTIVE INDEX INCREMENTS IN MULTICOMPONENT SYSTEMS [1]. *J. Phys. Chem.* **65,** 427–433 (1961).

109. Friebel, M. & Meinke, M. Model function to calculate the refractive index of native hemoglobin in the wavelength range of 250-1100 nm dependent on concentration. *Appl. Opt.* **45,** 2838–2842 (2006).

110. DeMoll, E., Cox, D. J., Daniel, E. & Riggs, A. F. Apparent specific volume of human hemoglobin: Effect of ligand state and contribution of heme. *Anal. Biochem.* **363,** 196–203 (2007).

Biography

Matthew Thomas Daniel Rinehart was born in Maplewood, Minnesota on Septembers 2nd, 1986. He was raised in Durham, North Carolina, attending C.E. Jordan High School and graduating in 2004. Matthew attended Duke Univeristy in Durham, NC and graduated in 2008 with B.S.E. degrees in biomedical and electrical engineering. He immediately began his graduate studies in biomedical engineering in the lab of Dr. Adam Wax, and was supported by McChesney and Chambers fellowships. He expects to defend his dissertation in the fall of 2014. During his time in Dr. Wax's lab, Matthew attended and presented at numerous conferences, has been an active member of the university's cycling team, and has published 13 peer-reviewed papers (listed below).

Publications:

1. Will J Eldridge, Amihai Meiri, Adi Sheinfeld, **Matthew T Rinehart**, Adam Wax, "Fast wide-field photothermal and quantitative phase cell imaging with optical lock-in detection," Biomedical Optics Express 5, 2517-2525 (2014).

2. **Matthew T. Rinehart**, Sheila Grab, Lisa C. Rohan, David Katz, and Adam Wax, "Analysis of vaginal microbicide film hydration kinetics by quantitative imaging refractometry," PLoS ONE 9(4): e95005 (2014).

3. **Matthew T. Rinehart**, Volker Jaedicke, and Adam Wax, "Quantitative Phase Microscopy with Off-Axis Optical Coherence Tomography," Optics Letters 39, 1996-1999 (2014).

4. Adam Wax, Amihai Meiri, Siddarth Arumugam, **Matthew T Rinehart, "**Comparative review of interferometric detection of plasmonic nanoparticles," Biomedical Optics Express, 4, 2166-2178 (2013).

5. Sanghoon Kim, **Matthew T. Rinehart**, Hansang Park, Yizheng Zhu, and Adam Wax, "Phase-sensitive OCT imaging of multiple nanoparticle species using spectrally

multiplexed single pulse photothermal excitation," Biomedical Optics Express 3, 2579-2586 (2012).

6. Adam Wax, Michael Giacomelli, Thomas E. Matthews, **Matthew T. Rinehart**, Francisco E. Robles, Yizheng Zhu, "Optical Spectroscopy of Biological Cells," Advances in Optics and Photonics 4, 322-378 (2012).

7. **Matthew T. Rinehart**, Yizheng Zhu, and Adam Wax, "Quantitative phase spectroscopy," Biomedical Optics Express 3, 958 (2012).

8. **Matthew T. Rinehart**, Tyler K. Drake, Francisco E. Robles, Lisa C. Rohan, David Katz, and Adam Wax, "Time-resolved imaging refractometry of microbicidal films using quantitative phase microscopy," Journal of Biomedical Optics 16, 120510 (2011).

9. Neil G. Terry, Yizheng Zhu, **Matthew T. Rinehart**, William J. Brown, Steven C. Gebhart, Stephanie Bright, Elizabeth Carretta, Courtney G. Ziefle, Masoud Panjehpour, Joseph Galanko, Ryan D. Madanick, Evan S. Dellon, Dimitri Trembath, Ana Bennett, John R. Goldblum, Bergein F. Overholt, John T. Woosley, Nicholas J. Shaheen, Adam Wax, "Detection of Dysplasia in Barrett's Esophagus With In Vivo Depth-Resolved Nuclear Morphology Measurements," Gastroenterology – 20 (2010)

10. **Matthew T. Rinehart**, Natan T. Shaked, Nathan J. Jenness, Robert L. Clark, and Adam Wax, "Simultaneous two-wavelength transmission quantitative phase microscopy with a color camera," Opt. Lett. 35, 2612-2614 (2010)

11. James C. Booth, Nathan D. Orloff, Jordi Mateu, Michael D. Janezic, **Matthew T. Rinehart**, and James A. Beall, "Quantitative Permittivity Measurements of Nanoliter Liquid Volumes in Microfluidic Channels to 40 GHz," IEEE Transactions on Instrumentation and Measurement 99, 1-10 (2010)

12. Natan T. Shaked, Yizheng Zhu, **Matthew T. Rinehart**, and Adam Wax, "Two-step-only phase-shifting interferometry with optimized detector bandwidth for microscopy of live cells," Opt. Express 17, 15585-15591 (2009)

13. Natan T. Shaked, **Matthew T. Rinehart**, and Adam Wax, "Dual-interference-channel quantitative-phase microscopy of live cell dynamics," Opt. Lett. 34, 767-769 (2009)